

FEEDBACK IN CLUSTER CORES

A dissertation presented to

the faculty of

the College of Arts and Sciences of Ohio University

In partial fulfillment

of the requirements for the degree

Doctor of Philosophy

David Rafferty

August 2007

This dissertation titled
FEEDBACK IN CLUSTER CORES

by
DAVID RAFFERTY

has been approved for
the Department of Physics and Astronomy
and the College of Arts and Sciences by

Brian R. McNamara

Professor of Physics and Astronomy

Benjamin M. Ogles

Dean, College of Arts and Sciences

Abstract

RAFFERTY, DAVID, Ph.D., August 2007, Physics and Astronomy

FEEDBACK IN CLUSTER CORES (172pp.)

Director of Dissertation: Brian R. McNamara

We present an analysis of star formation, cooling, and feedback in 61 galaxies at the cores of galaxy clusters. A subsample of 33 of these systems possesses cavities in the intracluster medium (ICM) inflated by radio jets emanating from their active galactic nuclei (AGN). We present an extensive analysis of the X-ray cavities in these systems. We find that AGN, through their cavities alone, are energetically able to balance radiative losses (cooling) from the ICM in more than half of these systems. Using the cavity (jet) powers, we place strong lower limits on the rate of growth of supermassive black holes in central galaxies, and we find that they are growing at an average rate of $\sim 0.1 M_{\odot} \text{ yr}^{-1}$, with some systems growing as quickly as $\sim 1 M_{\odot} \text{ yr}^{-1}$. We find a trend between bulge growth (star formation) and black hole growth that is approximately in accordance with the slope of the local (Magorrian) relation between black hole and bulge mass. However, the large scatter in the trend suggests that bulges and black holes do not always grow in lock step. With the exception of the rapidly accreting supercavity systems (e.g, MS 0735.6+7421), the black holes are accreting well below their Eddington rates. Most systems could be powered by Bondi accretion from the hot ICM, provided the central gas density increases into the Bondi

radius as $\rho \propto r^{-1}$. However, if the gas density profile flattens into a core, as observed in M87, Bondi accretion is unlikely to be driving the most powerful outbursts.

Using a subsample of 17 systems with published star formation rates, we examine the relationship between cooling and star formation. We find that the star formation rates are approaching or are comparable to X-ray and far-UV limits on the rates of gas condensation onto the central galaxy. The remaining radiative losses could be offset by AGN feedback. The vast gulf between radiative losses and the sink of cooling material, which has been the primary objection to cooling flows, has narrowed and, in some cases, is no longer a serious issue. Lastly, for a subsample of 40 systems, we use broadband optical imaging to measure the $U - I$ and $U - R$ colors in the galaxies at the cores of the clusters. By comparing the optical properties to the X-ray-derived properties on similar spatial scales, we find that blue colors, indicative of recent star formation, occur only in clusters for which the central X-ray-emitting gas has cooling times less than $\sim 7 \times 10^8$ yr (or entropies of less than ~ 30 keV cm 2), whereas red central colors occur over a wide range of cooling times.

Taken together, these findings represent compelling evidence for AGN feedback in massive halos.

Approved: _____

Brian R. McNamara

Professor of Physics and Astronomy

Table of Contents

	Page
Abstract	3
List of Tables	8
List of Figures	9
1 Introduction	11
2 Observations and Data Reduction	17
2.1 The Sample	17
2.2 X-ray Data	24
2.2.1 The <i>Chandra</i> X-ray Observatory	24
2.2.2 Standard Reductions	25
2.2.3 Spectral Analysis	27
2.3 Optical Data	33
2.3.1 MDM, KPNO, and WIYN	33
2.3.2 Standard Reductions	35
2.3.3 Sky Subtraction	39
2.3.4 Image Stacking	40
2.3.5 Calibration and Corrections	41
2.4 Literature Data	42
3 AGN Feedback	44
3.1 Introduction: Cavities in the ICM	44

3.2 Quantifying AGN Heating	45
3.2.1 Measuring the Cavities	45
3.2.2 Energies	50
3.2.3 Ages	50
3.2.4 Cavity Powers	52
3.3 Measuring Cooling	56
3.3.1 X-ray Spectra	56
3.3.2 Consistency Check: XMM- <i>Newton</i> and FUSE	58
3.4 Comparing Heating and Cooling	60
3.4.1 Quenching Cooling Flows	60
3.4.2 Duty Cycle	65
3.4.3 Trends between X-ray and Mechanical Luminosities	66
3.5 Summary	69
4 Star Formation and the Cooling Flow	72
4.1 Introduction: Active Star Formation in Cooling Flows	72
4.2 Derivation of Star Formation Rates	73
4.3 Comparing Star Formation and Cooling Rates	80
4.4 Comparing CDG Colors and Central ICM Properties	83
4.4.1 Excess Blue Emission as a Signature of Star Formation	83
4.4.2 Analysis of Imaging Data	85
4.4.3 Analysis of X-ray Data	103

4.4.4	Comparing Colors and Cooling Times	107
4.4.5	Comparing Colors and Other ICM Properties	114
4.5	Summary	116
5	Bulge and Black Hole Growth	118
5.1	Introduction: the Magorrian Relation	118
5.2	Quantifying Black Hole Growth	119
5.2.1	Black Hole Growth Rates	119
5.2.2	Eddington and Bondi Accretion Rates	123
5.2.3	Black Hole Masses	124
5.3	Comparing Black Hole and Bulge Growth	129
5.4	Accretion Mechanism	133
5.5	Summary	138
6	Conclusions	140
	Bibliography	142
A	Images	159
B	Pipeline Software	167
C	Co-authored Publications	172

List of Tables

2.1	The Full Sample.	19
2.2	Cavity-Sample Properties.	22
2.3	X-ray and Optical Observations.	31
3.1	Cavity Properties.	47
3.2	Cavity and ICM Properties Derived from <i>Chandra</i> Data.	54
4.1	Star Formation and Cooling Rates.	75
4.2	CDG Color Gradients and Δ Colors.	97
4.3	Central ICM Properties.	105
4.4	Interpolated ICM Cooling Times.	106
5.1	Black Hole Masses and Growth Rates.	121
5.2	Central ICM Properties Used in the Bondi Calculations.	125

List of Figures

1.1 Examples of interactions between the radio source and the ICM.	15
2.1 Dark current in the Echelle CCD.	36
3.1 Histograms of cavity radii.	46
3.2 XMM- <i>Newton</i> , FUSE, and <i>Chandra</i> cooling rates compared.	59
3.3 Cavity power of the central AGN versus the X-ray luminosity of the intracluster medium.	62
3.4 The average cavity buoyancy age versus the central cooling time.	67
4.1 Net cooling rate versus the star formation rate.	82
4.2 $U - R$ color profiles.	91
4.3 $U - I$ color profiles.	92
4.4 $G(U - I)$ vs. $G(U - R)$	95
4.5 Comparison of our $U - I$ color profiles to those from the literature. .	100
4.6 Comparison of color profiles from different observing runs	102
4.7 <i>Left:</i> Color gradient versus the central cooling time. <i>Right:</i> Color gradient versus the cooling time at a radius of 12 kpc.	107
4.8 Histogram of the cooling times at 12 kpc.	109
4.9 $\Delta(U - R)$ and $\Delta(U - I)$ versus the cooling time at 12 kpc.	110

4.10 <i>Left:</i> Color gradient versus the separation between the CDG’s core and the cluster’s core. <i>Right:</i> Color gradient versus the cooling time at the radius of the CDG’s core.	111
4.11 Color gradient versus the ratio of cavity power to ICM luminosity. . .	113
4.12 <i>Left:</i> Color gradient versus the central temperature. <i>Right:</i> Color gradient versus the central pressure.	115
4.13 <i>Left:</i> Color gradient versus the central density. <i>Right:</i> Color gradient versus the central entropy.	115
5.1 Black hole growth rate versus star formation rate.	130
5.2 The black hole’s relative change in mass versus the mass of the black hole.	134
5.3 Bondi ratio (defined as $\dot{M}_{\text{acc}}/\dot{M}_{\text{Bondi}}$) versus the ratio of the semi-major axis of the central region to the Bondi radius.	135
A.1 Optical images of the CDGs in the sample.	160
A.2 Optical images of the CDGs in the sample — continued.	161
A.3 Optical images of the CDGs in the sample — continued.	162
A.4 Optical images of the CDGs in the sample — continued.	163
A.5 Optical images of the CDGs in the sample — continued.	164
A.6 Optical images of the CDGs in the sample — continued.	165
A.7 Optical images of the CDGs in the sample — continued.	166

CHAPTER 1

Introduction

A galaxy may be described as a gravitationally bound collection of stars, gas, dust, and dark matter. Until recently, our galaxy, the Milky Way, was thought to represent the entire universe; however, in 1923, Edwin Hubble confirmed the existence of objects at extragalactic distances, and our current view of a universe filled with luminous galaxies was formed. However, galaxies are not randomly distributed throughout the universe. Rather, they are often grouped or clustered together in gravitationally bound systems of galaxies that number from tens (“groups”) to thousands (“clusters”). Our own Milky Way belongs to the Local Group of approximately 30 galaxies. Both groups and clusters consist of luminous matter (stars and gas) and dark matter, with the ratio of dark to luminous matter being approximately 8 : 1. Furthermore, most of the luminous matter in clusters is not in stars, but instead in hot X-ray-emitting gas.

The temperature of this gas is mainly determined by the depth of the gravitational potential of the cluster as the infalling gas converts its potential energy to thermal energy, and is typically $\sim 10^7 - 10^8$ K. At these temperatures, the gas cools mainly through free-free and line emission in the X-ray region of the electromagnetic spectrum. Therefore, X-ray observations are the best way to image this gas. X-ray observations show us that the gas is fairly relaxed on large scales and approximately

in hydrostatic equilibrium, while on small scales, close to the cluster or group center, the ICM is often in a state of turmoil.

The centers of clusters and large groups often contain a single giant elliptical galaxy, referred to variously as the brightest cluster galaxy (BCG) or centrally-dominant galaxy (CDG). The CDG is often centered on the peak of the X-ray emission, implying a connection between the galaxy and the cooling ICM. The simplest theory for this connection is that the CDG was formed at least partly from the cooling ICM. A majority of clusters show highly peaked central emission from gas with short cooling times ([Peres et al., 1998](#)). As the ICM cools in approximately hydrostatic equilibrium, the dense central gas cools the most rapidly ($L \sim n^2 T^{1/2}$ for free-free emission). After a time of on the order of $10^8 - 10^9$ yr, this gas is expected, in the absence of heating, to drop out of hydrostatic equilibrium and form cold clouds of gas. The weight of the outer cluster atmosphere then causes a slow inflow of gas (a “cooling flow”), replacing the gas that has cooled.

This model, known as the cooling-flow model ([Fabian, 1994](#)), has been widely debated over the last 20 years. The debate has been fueled by a lack of evidence for the large amounts of cool gas and star formation that should be present in the CDG. Simple mass conservation requires that the amount of gas cooling out of the hot ICM should be equal to that seen in cold clouds and star formation. However, low spectral resolution ROSAT observations predicted deposition rates of $100 - 1000$'s $M_\odot \text{ yr}^{-1}$, exceeding both the inferred star formation rates ([McNamara, 1997](#)) and the implied

cold gas masses (Edge, 2001) by an order of magnitude. This discrepancy between the X-ray-derived cooling rates and optically derived star formation rates became known as the “cooling-flow problem.”

Recently, however, high-spectral resolution observations by the *Chandra* X-ray Observatory (McNamara et al., 2000; David et al., 2001; Blanton et al., 2003) and *XMM-Newton* (Peterson et al., 2003; Kaastra et al., 2004) have shown that the cooling rates predicted by ROSAT are too large by a factor of ten. These new telescopes show that cooling-flow spectra lack the emission signatures expected from gas cooling through $\sim 10^6$ K. For a cluster experiencing only cooling, the cooling rate of gas cooling through 10^7 K (which accounts for most of the cluster X-ray emission) should be equal to that cooling through $\sim 10^6$ K. Instead, the spectra show evidence of gas cooling through lower temperatures at rates of only 10% of the gas cooling through high temperatures. Due to these findings, a paradigm shift has occurred in cooling-flow theory. Whereas the classical cooling-flow problem was the discrepancy between the high cooling rates and low star formation rates, the “new” cooling-flow problem is the discrepancy between the radiation seen from gas at high temperatures (10^7 K) and that at lower temperatures (10^6 K). There are two main theories to account for this discrepancy: that the gas is cooling at its previously predicted rate, but without the spectroscopic signature expected in the classical cooling model, or that the gas is being heated and maintained at $\sim 10^7$ K.

Scenarios that account for the lack of emission lines from gas below $\sim 10^7$ K yet still maintain the large cooling rates include inhomogeneous metalicity distributions, differential absorption, or efficient mixing (e.g., [Fabian et al., 2001](#)); however, these possibilities all lack observational support. If, instead, the gas is being maintained at $\sim 10^7$ K, some form of heating is required. Heat may be supplied in a number of ways: by conduction from the cluster's hot outer atmosphere to its cool center, by supernovae explosions in the CDG, or by the AGN. Conduction, operating at the Spitzer rate or below, can have a significant effect on the outer parts of clusters ([Voigt & Fabian, 2004](#)); however, it can be unstable and cannot entirely balance cooling losses by itself ([Voigt et al., 2002](#); [Soker, 2003](#); [Wise et al., 2004](#)). Supernovae as well cannot supply enough heat to balance cooling ([McNamara et al., 2004](#)). AGN heating can not only supply enough energy to balance the radiative losses (e.g., Hydra A, [McNamara et al., 2000](#)) but naturally provides heat where it is most needed – in the core. AGN heating is therefore the most promising heating method to balance the cooling ICM.

AGN heating acts primarily on the inner part of the cluster where the AGN interacts with the ICM though its radio-emitting jets and lobes. The AGN is presumably powered by accretion of gas onto a supermassive black hole at the center of the CDG. As the gas accretes, part of its gravitational energy is converted to kinetic energy in a pair of oppositely directed jets of high energy particles and magnetic fields that radiate at radio wavelengths. These jets are seen in some clusters to be pushing

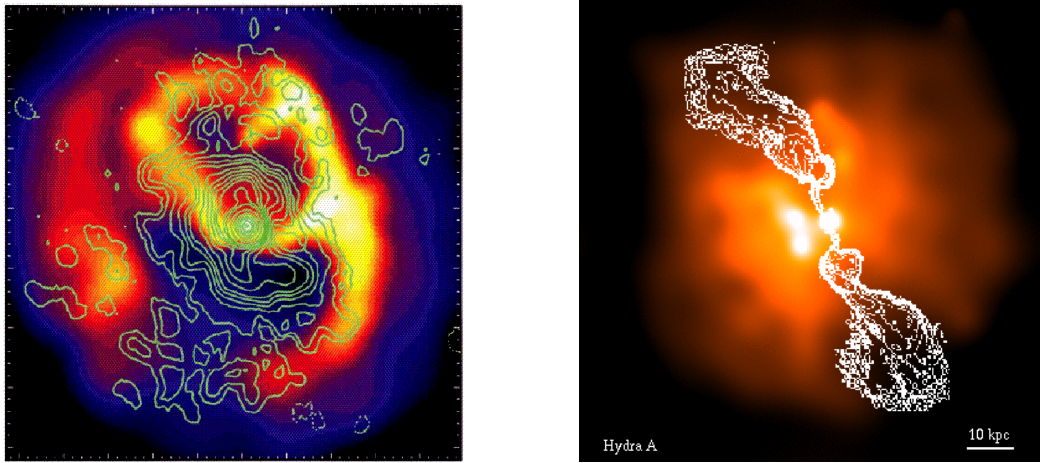


Figure 1.1: Examples of interactions between the radio source (shown as contours) and the ICM in *Chandra* X-ray images of Abell 2052 (*left*) and Hydra A (*right*).

out cavities of hot plasma, as shown in Figure 1.1, injecting energy at rates of up to $\sim 10^{45} - 10^{46}$ ergs s $^{-1}$. These cavities are capable in many objects of balancing cooling losses, but are unable to account alone for the radiation losses in all systems (Bîrzan et al., 2004; Rafferty et al., 2006). However, if AGN heating is periodic – a theory supported by the presence in some objects of multiple generations of cavities (e.g. Perseus, M87, and Hydra A) – some systems may be in a lower state of heating presently than other systems, thereby accounting for the AGN’s inability to supply enough heat to balance cooling in all systems at all times.

The nature of AGN heating suggests that a feedback mechanism exists between the cooling gas and the source of heat, such that the heating rate scales with the cooling rate. This feedback could take the form of a self-regulated loop in which cooling

gas accretes onto the central black hole, fueling episodic radio outbursts, the power of which scales with the rate of accreting gas. The outbursts temporarily quench or significantly reduce cooling. Eventually, in the absence of accreting material, the AGN weakens or turns off entirely, and cooling begins again. The intermittent or residual cooling would eventually lead to cold clouds and stars, but at rates much less than previously expected in the steady-state, classical cooling-flow picture (for a review, see [McNamara, 2004](#); [McNamara & Nulsen, 2007](#)).

In this dissertation, we describe an investigation into observational evidence for the new cooling-flow paradigm described above. We use optical and X-ray data to investigate connections between star formation, AGN heating, and the ICM properties for a sample of cooling flows and non-cooling flows. Chapter 3.2 of this dissertation was published in [Birzan et al. \(2004\)](#) and [Rafferty et al. \(2006\)](#); Sections 4.1, 4.2, and 4.3 and Chapter 5 were published in [Rafferty et al. \(2006\)](#). We assume $H_0 = 70 \text{ km s}^{-1} \text{ Mpc}^{-1}$, $\Omega_\Lambda = 0.7$, and $\Omega_M = 0.3$ throughout.

CHAPTER 2

Observations and Data Reduction

2.1 The Sample

The objects that comprise the sample were drawn from objects with observations publicly available in the *Chandra* Data Archive.¹ The entire sample of 61 objects can be divided into two subsamples: the first, used to investigate AGN heating, is composed primarily of clusters identified in the archive with cavities in their X-ray emission associated with the central AGN; the second, used to investigate the connection between star formation and the cooling flow, is composed of objects with acceptable total X-ray counts ($\gtrsim 10000$) that were observable from the optical observatories located at Kitt Peak, Arizona, on the scheduled nights. Some objects are shared between the two samples. Table 2.1 lists the general properties of the objects in both samples.

The cavity sample was constructed by doing a visual survey of all clusters in the *Chandra* Data Archive as of January, 2006, and identifying those with cavities. The sample comprises 31 CDGs, 1 group dominant galaxy (HCG 62), and 1 giant elliptical (M84). The sample ranges in redshift from $z = 0.0035$ to $z = 0.545$ and varies in its composition from groups to rich clusters. We note that this sample is biased in favor

¹See <http://cxc.harvard.edu/cda/>

of cavity systems; therefore, conclusions drawn from this sample may not apply to cooling flows as a whole. However, in Section 3.4.1, we attempt to correct for this bias using the flux-limited sample of Dunn & Fabian (2006). Table 2.2 lists the properties of the cavity sample and references for publications that discuss the cavities or X-ray data.

The optical cooling-flow sample comprises 40 CDGs, including 12 systems from the cavity sample, for which we have obtained broadband optical data. The optical data were designed to identify the presence of recent star formation in the CDG. To test whether the presence of any such star formation is related to the cooling flow, the objects in this sample were chosen to have a wide range of central cooling times, from $t_{\text{cool}} \lesssim 10^8$ yr to $t_{\text{cool}} \gtrsim 10^{10}$ yr, and range in redshift from $z = 0.0035$ to $z = 0.545$. See Table 2.3 for details of the observations.

Table 2.1. The Full Sample.

System	z	X-ray Core (J2000)		CDG Name	CDG Core (J2000)	
		α ($^{\circ}$)	δ ($^{\circ}$)		α ($^{\circ}$)	δ ($^{\circ}$)
A85	0.055	10.4593	-9.3022	PGC 002501	10.4603	-9.3031
3C 28	0.195	13.9599	26.4098	PGC 138263	13.9609	26.4105
A133	0.057	15.6744	-21.8804	ESO 541-013	15.6739	-21.8820
A223	0.207	24.4828	-12.8198	2MASX J01375602-1249106	24.4833	-12.8195
A262	0.016	28.1922	36.1528	NGC 708	28.1936	36.1520
A383	0.187	42.0139	-3.5291	PGC 145057	42.0141	-3.5291
AWM 7	0.017	43.6145	41.5797	NGC 1129	43.6139	41.5796
Perseus	0.018	49.9507	41.5118	NGC 1275	49.9510	41.5116
2A 0335+096	0.035	54.6700	9.9660	PGC 013424	54.6691	9.9701
A478	0.088	63.3551	10.4653	PGC 014685	63.3553	10.4652
A496	0.033	68.4076	-13.2619	PGC 015524	68.4077	-13.2619
A520	0.199	73.5422	2.9248	PGC 1240180	73.5160	2.8923
MS 0735.6+7421	0.216	115.4351	74.2440	PGC 2760958	115.4361	74.2438
PKS 0745-191	0.103	116.8806	-19.2947	PGC 021813
4C 55.16	0.242	128.7287	55.5725	PGC 2506893
Hydra A	0.055	139.5238	-12.0953	PGC 026269
RBS 797	0.350	146.8043	76.3873
Zw 2701	0.214	148.2050	51.8849	PGC 2401970
Zw 3146	0.290	155.9152	4.1863	2MASX J10233960+0411116
A1068	0.138	160.1853	39.9532	PGC 093944
A1361	0.117	175.9150	46.3562	PGC 093947	175.9150	46.3556
A1413	0.143	178.8249	23.4052	PGC 037477	178.8250	23.4049
M84	0.004	186.2651	12.8869	M84
M87	0.004	187.7057	12.3913	M87	187.7059	12.3912
Centaurus	0.011	192.2038	-41.3111	NGC 4696
HCG 62	0.014	193.2740	-9.2036	NGC 4778	193.2738	-9.2040
A1650	0.084	194.6727	-1.7617	PGC 1110773	194.6730	-1.7614
Coma	0.023	194.8984	27.9591	NGC 4874	194.8988	27.9593

Table 2.1 (continued)

System	z	X-ray Core (J2000)		CDG Name	CDG Core (J2000)	
		α ($^{\circ}$)	δ ($^{\circ}$)		α ($^{\circ}$)	δ ($^{\circ}$)
A1795	0.063	207.2196	26.5913	PGC 049005	207.2188	26.5929
A1835	0.253	210.2581	2.8789	2MASX J14010204+0252423
PKS 1404-267	0.022	211.8738	-27.0179	IC 4374
MACS J1423.8+2404	0.545	215.9492	24.0786
A1991	0.059	223.6314	18.6445	NGC 5778	223.6313	18.6424
MS 1455.0+2232	0.258	224.3128	22.3424	PGC 1668167	224.3130	22.3429
RXC J1504.1-0248	0.215	226.0310	-2.8043	PGC 126345	226.0313	-2.8045
A2029	0.077	227.7337	5.7449	PGC 054167
A2052	0.035	229.1851	7.0215	UGC 09799
MKW 3S	0.045	230.4653	7.7073	NGC 5920
A2065	0.073	230.6224	27.7052	PGC 054888	230.6215	27.7077
RX J1532.8+3021	0.345	233.2242	30.3497	PGC 1900245	233.2241	30.3499
A2199	0.030	247.1591	39.5512	NGC 6166
A2218	0.176	248.9613	66.2110	PGC 140648	248.9553	66.2124
Hercules A	0.154	252.7841	4.9924	PGC 059117	252.7840	4.9927
A2244	0.097	255.6775	34.0606	PGC 140689	255.6772	34.0604
NGC 6338	0.027	258.8453	57.4113	NGC 6338	258.8456	57.4114
RX J1720.2+2637	0.164	260.0413	26.6250	PGC 1782937	260.0419	26.6256
MACS J1720.2+3536	0.391	260.0699	35.6075	...	260.0699	35.6074
A2261	0.224	260.6132	32.1327	PGC 1981854	260.6133	32.1326
3C 388	0.092	281.0098	45.5582	PGC 062332
A2319	0.056	290.3044	43.9366	PGC 063099	290.2918	43.9456
3C 401	0.201	295.1042	60.6933	PGC 2605547
Cygnus A	0.056	299.8682	40.7341	PGC 063932
A2390	0.228	328.4034	17.6955	PGC 140982	328.4035	17.6957
A2409	0.148	330.2194	20.9743	PGC 093957	330.2191	20.9693
Sersic 159/03	0.058	348.4935	-42.7257	ESO 291-009
A2597	0.085	351.3322	-12.1239	PGC 071390	351.3322	-12.1242

Table 2.1 (continued)

System	z	X-ray Core (J2000)		CDG Name	CDG Core (J2000)	
		α ($^{\circ}$)	δ ($^{\circ}$)		α ($^{\circ}$)	δ ($^{\circ}$)
A2626	0.055	354.1271	21.1471	IC 5338	354.1270	21.1464
A2657	0.040	356.2393	9.1919	PGC 072297	356.2393	9.1932
A2670	0.076	358.5571	-10.4189	PGC 072804	358.5570	-10.4190
A4059	0.048	359.2517	-34.7620	ESO 349-010

Note. — The X-ray and CDG core locations are from this work.

Table 2.2. Cavity-Sample Properties.

System	σ_c^a (km s $^{-1}$)	M_K^b	M_R^b	M_{bulge}^c (10 $^{11} M_\odot$)	References
A85	340 \pm 9	-26.72 \pm 0.04	-24.80 \pm 0.08	31 \pm 1	9, 25
A133	...	-26.36 \pm 0.06	-24.18 \pm 0.05	17.9 \pm 0.4	17, 18
A262	255 \pm 8	-25.65 \pm 0.03	-22.77 \pm 0.02	4.9 \pm 0.1	4
Perseus	247 \pm 10	-26.23 \pm 0.04	-24.25 \pm 0.01	19.2 \pm 0.1	11, 12, 14, 42
2A 0335+096	...	-26.15 \pm 0.05	-24.18 \pm 0.13	18 \pm 1	30
A478	...	-26.64 \pm 0.07	-24.66 \pm 0.10	28 \pm 1	43, 47
MS 0735.6+7421	...	-26.37 \pm 0.17	-24.51 \pm 0.10	24 \pm 1	35
PKS 0745-191	...	-26.82 \pm 0.09	-24.63 \pm 0.10	27 \pm 1	20
4C 55.16	...	-26.10 \pm 0.13	-24.75 \pm 0.50	30 \pm 8	21
Hydra A	322 \pm 20	-25.91 \pm 0.06	-24.67 \pm 0.05	28.2 \pm 0.7	8, 32, 37, 39
RBS 797	44
Zw 2701	...	-26.26 \pm 0.17	-24.75 \pm 0.10	30 \pm 1	1
Zw 3146	...	-27.67 \pm 0.14	1, 22
A1068 ^d	...	-26.71 \pm 0.08	-25.07 \pm 0.21	41 \pm 4	34, 49
M84	298 \pm 2	-24.69 \pm 0.02	-22.62	4.3	15
M87	341 \pm 3	-25.55 \pm 0.02	-23.61	11	16, 50
Centaurus	257 \pm 6	-26.02 \pm 0.02	-23.70 \pm 0.01	11.6 \pm 0.1	41, 44
HCG 62	...	-25.26 \pm 0.03	48
A1795	294 \pm 10	-26.50 \pm 0.08	-23.86 \pm 0.10	13.4 \pm 0.6	10
A1835	...	-27.36 \pm 0.14	36, 45
PKS 1404-267	258 \pm 7	-25.30 \pm 0.03	-22.93 \pm 0.20	5.7 \pm 0.5	24
MACS J1423.8+2404	52
A2029	366 \pm 9	-27.44 \pm 0.05	-24.39 \pm 0.02	21.9 \pm 0.2	6
A2052	259 \pm 11	-26.27 \pm 0.06	-23.62	11	2, 3
MKW 3S	...	-25.55 \pm 0.06	-23.67 \pm 0.05	11.2 \pm 0.3	29, 31
A2199	302 \pm 4	-26.37 \pm 0.03	-24.03 \pm 0.03	15.7 \pm 0.2	23
Hercules A	...	-26.45 \pm 0.11	-23.95 \pm 0.50	1.5 \pm 4	38
3C 388	365 \pm 23	-26.24 \pm 0.06	-24.46 \pm 0.50	23 \pm 6	27, 28

Table 2.2 (continued)

System	σ_c^a (km s $^{-1}$)	M_K^b	M_R^b	M_{bulge}^c ($10^{11} M_\odot$)	References
3C 401	-23.43 ± 0.50	9 ± 2	40
Cygnus A	...	-26.70 ± 0.06	-23.47 ± 0.35	9 ± 2	26, 46
Sersic 159/03	...	-26.26 ± 0.10	-23.68 ± 0.39	11 ± 2	51
A2597	222 ± 18	-25.55 ± 0.11	-23.49 ± 0.21	9 ± 1	7, 33
A4059	296 ± 49	-26.74 ± 0.05	-25.00 ± 0.02	38.2 ± 0.4	5, 19

References. — (1) Bauer et al. (2005); (2) Blanton et al. (2001); (3) Blanton et al. (2003); (4) Blanton et al. (2004); (5) Choi et al. (2004); (6) Clarke et al. (2004); (7) Clarke et al. (2005); (8) David et al. (2001); (9) Durret et al. (2005); (10) Ettori et al. (2002); (11) Fabian et al. (2000); (12) Fabian et al. (2003a); (13) Fabian et al. (2005); (14) Fabian et al. (2006); (15) Finoguenov & Jones (2001); (16) Forman et al. (2005); (17) Fujita et al. (2002); (18) Fujita et al. (2004); (19) Heinz et al. (2002); (20) Hicks et al. (2002); (21) Iwasawa et al. (2001); (22) Jeltema et al. (2005); (23) Johnstone et al. (2002); (24) Johnstone et al. (2005); (25) Kempner et al. (2002); (26) Kino & Kawakatu (2005); (27) Kraft et al. (2006); (28) Leahy & Gizani (2001); (29) Mazzotta et al. (2002); (30) Mazzotta et al. (2003); (31) Mazzotta et al. (2004); (32) McNamara et al. (2000); (33) McNamara et al. (2001); (34) McNamara (2004); (35) McNamara et al. (2005); (36) McNamara et al. (2006); (37) Nulsen et al. (2002); (38) Nulsen et al. (2005a); (39) Nulsen et al. (2005b); (40) Reynolds et al. (2005); (41) Sanders & Fabian (2002); (42) Sanders et al. (2005); (43) Sanderson et al. (2005); (44) Schindler et al. (2001); (45) Schmidt et al. (2001); (46) Smith et al. (2002); (47) Sun et al. (2003); (48) Vrtilek et al. (2002); (49) Wise et al. (2004); (50) Young et al. (2002); (51) Zakkamska & Narayan (2003); (52) Allen et al. (2004).

^aCentral stellar velocity dispersions were taken from the HyperLeda database; when more than one measurement was available, a weighted average was used. For the purposes of the buoyancy-age calculation, when no velocity dispersion was available, the average value for our sample ($\langle \sigma \rangle = 295$ km s $^{-1}$) was adopted.

^bTotal magnitudes from the 2MASS catalog (K -band) or HyperLeda catalog (R -band), corrected for Galactic extinction, K -correction, and evolution (see text for details).

^dThe *Chandra* image of A1068 does not show evidence of cavities. A1068 is included because of the large starburst in the central galaxy.

2.2 X-ray Data

2.2.1 The *Chandra* X-ray Observatory

The *Chandra* X-ray Observatory, launched in 1999, has revolutionized the X-ray study of clusters of galaxies. X-ray observatories previous to *Chandra*, such as *Einstein* (launched in 1978) and ROSAT (launched in 1990), were useful for studying the large-scale properties of the cluster, but were unable to image the X-ray-emitting gas on small scales (~ 1 arcsec), similar to the scales at which optical and radio data are generally available. *Chandra*'s arcsecond resolution has revealed that the ICM in cores of clusters, once thought to be fairly smooth and dynamically relaxed, is often very disturbed, with a complex structure that includes the X-ray cavities that form the basis of this dissertation. Additionally, the *Chandra* imager records both spatial and spectral information. Effectively, the position and energy of each X-ray photon is recorded. This record makes it possible to extract spectra from any region of the image tailored to each object, a feature we take advantage of when deriving radial profiles of the ICM's temperature, density, and pressure (described in Section 2.2.3).

Table 2.3 lists the observational details for each object in the sample. The X-ray data were all obtained from the *Chandra* Data Archive.²

²See <http://cxc.harvard.edu/cda/>

2.2.2 Standard Reductions

Due to the complexity of *Chandra* data reduction and to facilitate the reduction of the large number of observations, pipeline software was written to automate a significant portion of the process. The software was written in IDL, the Interactive Data Language,³ with calls to CIAO, the *Chandra* Interactive Analysis of Observations software.⁴ The pipeline software in total comprises more than 4000 lines of code, with 1200 lines devoted to the standard reductions discussed here and the remainder to imaging and spectral analysis (discussed in Sections 3.2, 3.3, and 4.4.3). See Appendix B for details of the pipeline software.

All data were observed with the ACIS detector and reduced using CIAO 3.3 using the calibration database CALDB 3.2.0. In brief, the steps performed in the general reduction of each observation are as follows.

- 1. Reprocessing:** The processed data downloaded from the *Chandra* Data Archive was reprocessed to apply the latest calibrations and corrections uniformly. Most important among these are corrections for the time-dependent charge transfer inefficiency (CTI), which corrects for losses in charge during the CCD readout; corrections to the gain map, which determines how charge is mapped to photon energy; and removal of cosmic ray events.

³See <http://www.ittvis.com/idl/>

⁴See <http://cxc.harvard.edu/ciao/>

2. Background Determination: Since many of our systems have extended emission that fills the entire field of view of the CCD, we used blank-sky background files to account for the X-ray background in our observations. The X-ray background sometimes undergoes flaring, in which the background event rate increases by up to a factor of 100. These periods were excluded by filtering the lightcurve for periods during which the count rate exceeds 20% the quiescent background count rate (after exclusion of all point sources, which may also vary). The remaining quiescent X-ray background consists primarily of two components: a soft ($E \lesssim 2$ keV) component due to the cosmic X-ray background, and a hard component ($E \gtrsim 2$ keV) due to cosmic rays, many of which are excluded in the previous step. This background was found to be stable in time, and can therefore be used, with proper normalization to account for differing foreground extinction, for most observations.⁵

The background normalization was calculated by comparing the count rates in the blank-sky background file with those in the source observation (after removing point sources) in the 10-12 keV energy range. This range ensures that there is no contaminating emission present (e.g., from the cluster). Additionally, since the background varies with position on the CCD, background spectra were extracted from the normalized blank-sky files and source files from the identical

⁵See <http://cxc.harvard.edu/contrib/maxim/bg/>

regions (after reprojection of the background data to match the aspect solution of the source data).

3. Images and exposure maps: Images were made of each field in a number of bands (0.3-0.54 keV, 0.54-1.0 keV, 1.0-1.6 keV, 1.6-2.0 keV, 2.0-3.5 keV, 3.5-5.0 keV, and 5.0-7.0 keV) to check for the presence of a hard-spectrum point source at the cluster's center, which is indicative of a central AGN. Any such point sources were removed before spectral fitting was performed. We detected and removed hard central point sources in approximately 20% of our sample. Lastly, an exposure map was made to correct images for pixel-to-pixel variations in effective area, using weights appropriate for a single-temperature plasma. Systematic errors can result from this approximation, since the cluster emission is due to gas at a variety of temperatures; however, because the spectrum of a single-temperature plasma is fairly smooth as a function of energy and the temperature does not vary strongly with position, such errors should generally be small (< 10%).⁶ The exposure-corrected images were used to measure the cavities (Section 3.2.1) and to derive surface-brightness profiles (Section 4.4.3).

2.2.3 Spectral Analysis

Here we describe the basic spectral analysis common to all objects. This analysis involves the extraction and fitting of spectra in concentric annuli to derive basic prop-

⁶See http://cxc.harvard.edu/ciao/threads/spectral_weights/

erties of the cluster's atmosphere, such as its temperature and density as functions of radius.

Since the X-ray emission from most clusters is reasonably smooth and relaxed, the ICM properties at a given radius (or along a given ellipse) are fairly constant as a function of azimuthal angle. We use this property to derive the radial profiles of various ICM properties by extracting spectra in concentric annuli centered on the cluster core. The spectra were extracted from the reprocessed and cleaned data using the *dmextract* CIAO tool. Weighted responses (used to convert readout counts to photon energy) were made using *mkwarf* and *mkacisrmf* for observations made at a focal-plane temperature of -120 C and *mkrmf* for all others. The spectra were then fit with models of a single-temperature plasma (plus foreground absorption to account for Galactic HI).

The resulting best-fit models give the emission-weighted temperature, abundance, and emissivity of plasma within the extracted region. However, the spectrum from an annulus at a given radius will include emission from a variety of radii, due to the projection of background and foreground emission. Assuming the ICM is fairly smooth, we can account for this projection using an onion-peel model for the cluster emission. With this technique, known as deprojection, emission from outer shells is estimated and subtracted from the inner spectra during fitting. We then recover the temperature, abundance, and emissivity in each shell, allowing us to calculate the density within the shell.

We used the PROJCT model in XSpec version 11.3.1 to perform the deprojection. The PROJCT model fits all spectra simultaneously while accounting for geometric projection effects to arrive at the best-fit parameters. Because the PROJCT model effectively moves flux between spectra, a large total number of counts is required to obtain reliable fits. Typically, spectra were extracted to contain at least 3000 counts each and then binned on energy to a minimum of 30 counts per energy bin. A thorough testing of the PROJCT model was done by [Johnstone et al. \(2005\)](#), who found that the model reproduced the intrinsic density and temperature profiles accurately in all but the outermost annulus. The quantities of the outermost annulus were overestimated due to projected emission from cluster gas at larger radii. However, this problem does not affect our results as we are interested in the properties in the cores of our systems, well inside the outer annulus used in deprojection.

Typically, deprojection recovers a lower temperature in the inner few annuli, since projected emission from the hotter outer gas has been accounted for, but there should be no large differences between deprojected and projected quantities. We note that the PROJCT model allows deprojection using elliptical shells, which has proved useful since many of the systems in our sample are elliptical in projection. However, we have generally found only small differences between the density profiles derived using elliptical shells and spherical shells ($\lesssim 10\%$). The PROJCT model also allows for incomplete shells, which was used when the cluster was positioned such that some of the annuli extended partly off the chip (e.g., near a corner of the chip). Lastly,

it should be noted that the results of any deprojection method will be somewhat in error in the complex inner regions of the cluster where the emission is not smooth or azimuthally symmetric.

Each spectrum was fit with a single-temperature (MEKAL) model ([Liedahl et al., 1995](#)) with a component to account for Galactic absorption (WABS). The column density of the WABS component was fixed to the Galactic value of [Dickey & Lockman \(1990\)](#). The temperature and abundance (relative to the solar values of [Anders & Grevesse, 1989](#)) of the MEKAL model were allowed to vary, and the redshift was fixed to the value given in Table [2.1](#). We fit to the well-calibrated energy range of 0.5-7.0 keV. The density was then calculated from the normalization of the MEKAL component, assuming $n_e = 1.2n_H$ (for a fully ionized gas with hydrogen and helium mass fractions of $X = 0.7$ and $Y = 0.28$), as:

$$n_e = \sqrt{\frac{1.2 \times 10^{14} (4\pi D_L^2) \times \text{norm}}{(1+z)^2 V}}, \quad (2.1)$$

where n_e has units of cm^{-3} , the luminosity distance (D_L) has units of cm, and the volume of the shell (V) has units of cm^3 . The pressure in each annulus was calculated as $P = nkT$, where we have assumed an ideal gas and $n \approx 2n_e$.

Table 2.3. X-ray and Optical Observations.

System	X-ray Observations			Optical Observations				Photometric?
	OBSID	Exp. Time ^a (ks)	Telescope	Total Exp. Time (s)	<i>U</i>	<i>R</i>	<i>I</i>	
A85	904	37.5	2.4 m	1200	300	450	...	Y
3C28	3233	48.2	2.4 m	1800	300	450	...	Y
A133	2203	30.9	4 m	2000	200	800	...	N
A223	4967	42.2	4 m	2200	1600	300	...	Y
A262	2215	26.7	4 m	1200	...	1000	...	N
A383	2321	16.8	2.4 m	1800	450	225	...	Y
AWM 7	908	47.9	2.4 m	600	...	450	...	Y
Perseus	4947	29.6	4 m	3600	...	500	...	Y
2A 0335+096	919	16.1	2.4 m	1200	300	450	...	Y
A478	1669	41.0	4 m	1800	700	Y
A496	4976	58.0	2.4 m	1200	300	450	...	Y
A520	4215	54.2	4 m	3200	300	1200	...	N
MS 0735.6+7421	4197	39.9	3.5 m	2100	3600	2400	...	Y
PKS 0745-191	2427	17.4
4C 55.16	4940	66.5
Hydra A	4970	98.8
RBS 797	2202	8.7
Zw 2701	3195	22.2
Zw 3146	909	41.5
A1068	1652	25.6
A1361	3369	3.0	2.4 m	1800	450	225	...	Y
A1413	5003	65.8	2.4 m	2700	900	450	...	Y
M84	803	25.8
M87	3717	15.1	2.4 m	600	200	345	...	Y
Centaurus	5310	48.9
HCG 62	921	47.5	2.4 m	300	150	150	...	Y
A1650	4178	26.6	2.4 m	300	150	150	...	Y
Coma	1086	9.3	2.4 m	900	300	Y
RX J1347.5-1145	3592	51.8	2.4 m	150	150	150	...	Y
A1795	3666	14.2	2.4 m	1800	450	225	...	Y
A1835	496	10.3
PKS 1404-267	1650	6.6
MACS J1423.8+2404	4195	110.2
A1991	3193	35.8	2.4 m	1800	450	225	...	Y
MS 1455.0+2232	4192	83.2	2.4 m	1800	450	225	...	Y
RXC J1504.1-0248	5793	33.2	2.4 m	1800	600	900	...	Y
A2029	4977	77.3
A2052	890	36.1
MKW 3S	900	55.2
A2065	3182	26.0	2.4 m	1800	450	225	...	Y

Table 2.3 (continued)

System	X-ray Observations			Optical Observations				Photometric?
	OBSID	Exp. Time ^a (ks)	Telescope	Total	Exp. Time (s)	<i>U</i>	<i>R</i>	<i>I</i>
RX J1532.8+3021	1649	8.8	2.4 m	3600	1200	900	...	Y
A2199	498	15.9
A2218	1666	34.2	2.4 m	1800	400	600	...	Y
Hercules A	1625	12.5	4 m	2400	1200	Y
A2244	4179	55.7	2.4 m	1500	450	600	...	Y
NGC 6338	4194	44.0	2.4 m	1800	450	225	...	Y
RX J1720.2+2637	4361	22.0	2.4 m	1200	300	300	...	Y
			4 m	2400	...	600	...	N
MACS J1720.2+3536	6107	29.7	2.4 m	1800	450	225	...	Y
A2261	5007	21.7	2.4 m	3600	1050	1800	...	Y
3C 388	5295	25.8
A2319	3231	14.1	2.4 m	1200	...	600	...	Y
3C 401	4370	21.8
Cygnus A	360	34.2
A2390	4193	83.3	2.4 m	1200	300	450	...	Y
			4 m	2400	1100	1000	...	Y
A2409	3247	9.7	2.4 m	1800	450	675	...	Y
Sersic 159/03	1668	9.7
A2597	922	11.3	2.4 m	600	150	450	...	Y
A2626	3192	23.5	2.4 m	1200	300	450	...	Y
A2657	4941	15.6	4 m	1200	600	400	...	N
A2670	4959	33.5	4 m	1200	...	600	...	Y
A4059	5785	92.1

^aExposure time after cleaning for background flares.

2.3 Optical Data

2.3.1 MDM, KPNO, and WIYN

Since we wish to search for connections between star formation and the cooling flow, we need data that are sensitive to the presence of active star formation. Such star formation is best detected at short wavelengths. To take advantage of the rising spectral energy distribution (SED) of hot stars in the ultraviolet and the falling SED of the background galaxy population (see Section 4.4.1), we chose to observe in U -band (with a central wavelength of 3582 Å). This choice minimizes contamination from [OII] emission lines expected to be present in many of the systems. At long wavelengths, contamination from H α and H β lines can be a problem. However, the galaxies are bright at these wavelengths and therefore integration times will be short. Therefore, we chose to observe in both I and R filters (with central wavelengths of 6513 and 8204 Å, respectively). Observing in both filters allows us to choose the least contaminated image (depending on the redshift of the object). Additionally, colors obtained from both filters give us a means of verifying that any anomalous blue emission is due to star formation. If the $U - R$ and $U - I$ colors are both anomalously blue, it is likely to be due to star formation, and not due to contamination from emission lines (at least in the red filters).

Optical data were obtained during five separate runs. Three runs, totaling 11 nights, were done using the 2.4-m telescope at the MDM observatory on Kitt Peak,

Arizona between the dates of March 9-12, 2005, September 26-29, 2005, and May 22-24, 2006. An additional run of four nights was performed at the KPNO 4-m telescope between October 5-8, 2005. Lastly, a 2-night run was performed at the WIYN 3.5-m telescope between January 22-23, 2006. See Table 2.3 for details of the optical observations. Broadband imaging was done at MDM using the Echelle CCD with a 9.4×9.4 arcmin field of view and a scale of 0.28 arcsec pixel $^{-1}$. At the KPNO 4-m telescope, imaging was done using the Mosaic CCD array of eight CCDs with a 36×36 arcmin field of view and a scale of 0.26 arcsec pixel $^{-1}$. At the WIYN 3.5-m telescope, imaging was done using the Mini-Mosaic CCD array of two CCDs, with a 9.6×9.6 arcmin field of view and a scale of 0.14 arcsec pixel $^{-1}$. Harris U , R , and I filters were used during all runs. All objects were imaged in the U -band and in either R - or I -band (most objects were imaged in both R - and I -bands). Exposure times were typically 2×600 s in U , 2×150 s in I , and 2×225 s in R ; however, in some cases (e.g., for distant systems), longer total exposure times were required. Multiple frames were taken to allow for easy removal of cosmic-ray events. The frames were dithered by $\sim 30 - 60$ arcsec between exposures to allow for the removal of artifacts such as bad columns and CCD gaps and to improve flat fielding.

Conditions varied during the runs, with photometric conditions for approximately two-thirds of the total time. During photometric conditions, standard star observations were made at regular intervals over a wide range of airmass and color.

Optical reduction and analysis was performed using IRAF (the Image Reduction and Analysis Facility⁷), version 12.2.1, and custom procedures written in IDL.

2.3.2 Standard Reductions

The bias level and its row-to-row variation were modeled and subtracted in all frames by fitting a high-order function to the overscan region of each chip. The remaining bias structure was removed with a bias frame constructed by averaging 30-40 individual frames taken each night in the evening and morning. Twilight flats were then used to remove differences in pixel sensitivities across the chip. Flats were made for each night by averaging together at least 3 dithered frames taken during the evening and morning twilight with exposure levels of $\sim 1/2$ the saturation level of the CCDs.

The MDM Echelle CCD was found to have significant dark current ($\sim 0.1 - 0.2$ counts s^{-1}) during the March and September 2005 runs (the dark current during the May 2006 run was much lower), which resulted in large sky gradients in the long-exposure *U*-band frames. Additionally, a small but significant light contamination (probably due to light from the red light-emitting diodes on the instrument mounting) was present in the *R*- and *I*-band dark frames. We corrected for the dark current and light leak by creating a master dark frame in each band by averaging 4-5 individual frames together and subtracting a scaled version of this master frame from each object

⁷See <http://iraf.noao.edu/>

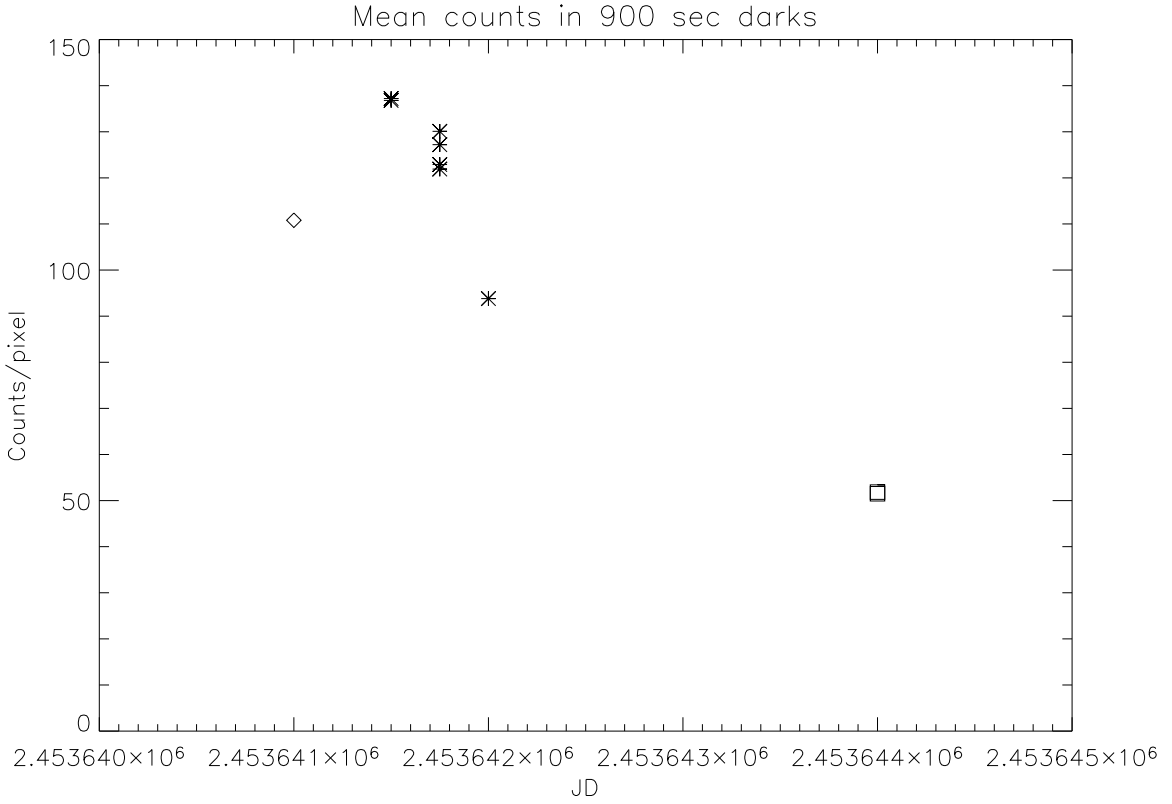


Figure 2.1: Counts per pixel versus time (Julian date) for 900 s darks taken during the three MDM runs: March 2005 (*diamond*), September 2005 (*stars*), and May 2006 (*square*). Note the strong change in dark current over the course of the September run.

frame. Each individual dark frame had a dark time typical of the longest exposure time used during observation (e.g., 900 s for U). Unfortunately, the dark current was found to vary both in magnitude (by a factor of two) and in spatial structure over the course of a single night (see Figure 2.1). This variation made it impossible to use a simple scaling by exposure time. Instead, the best scaling was determined using a χ^2 minimization routine. The best dark scaling for each object frame was determined by minimizing the residuals between the modes of the pixel values in multiple regions of the CCD after dark subtraction. This method effectively scales

the dark frame to produce the flattest sky across the CCD. However, for this method to be effective, sky variations due to pixel-to-pixel differences in sensitivity must first be removed by flat fielding. Therefore, the dark images were also flat fielded before fitting and subtraction. The fitting was done in IDL using the MPFIT package written by Craig Markwardt.⁸ Typically 9 object-free sub-regions of the chip in which the dark structure was most pronounced were used for fitting. If the fitted scaling in any given region differed by more than 3 sigma from the adopted mean it was rejected. The mean scaling across all the remaining regions was then used for dark subtraction. Remaining sky gradients were typically on the order of 2-3% of sky across the CCD, but they are generally much smaller ($\sim 0.5\%$) in the region of the BCG.

Fringing due to night sky lines was found to be significant in the I -band images; therefore a fringe frame for each night was constructed and subtracted from the I -band object frames. The fringe frame was made by averaging together all the I -band object frames of a given night, after masking of all objects (using the *objmasks* task in IRAF). The sky level and any large-scale gradient were removed from the fringe frame using a median filter over large blocks of pixels to filter out small-scale variations. The final fringe frame was then scaled and subtracted from all the I -band object frames using the *rmfringe* tool in IRAF.

In the KPNO data, an additional additive feature was present in I - and U -band images due to scattered light off of the prime-focus corrector (this feature is not

⁸See <http://cow.physics.wisc.edu/~craigm/idl/fitting.html>.

present in the *R*-band images due to the anti-reflective coating applied to the corrector). A template image of this “pupil ghost” was made using the *mscpupil* task in IRAF. This task isolates the pupil contribution to an image by fitting a spline function to the background of a master image and subtracting it off. The master image was made by averaging all flat-corrected images in a given filter over the entire run, after the masking of all objects using the *objmask* task in IRAF, and scaling by the mode of pixel values in object-free regions of the image. The resulting pupil template image was then scaled and subtracted off of each image interactively.

Once the additive features were subtracted from each frame, a dark-sky flat was made by again averaging all frames in a given filter over each night. Generally, 10-20 frames were required to produce good dark-sky flats. When an insufficient number of frames existed for a given night (due, e.g., to poor weather), a dark-sky flat from a neighboring night was used. Once again, all objects were masked before averaging. The sky flats were then median smoothed with a 129×129 -pixel box filter to reduce the noise but preserve large-scale structure.

Finally, a world coordinate system (WCS) solution was derived for each frame using the WCS mapping tools in IRAF. The WCS was accurately aligned and scaled to each frame using fits to USNO A2 catalog positions of typically 100-200 stars. After this adjustment, the WCS was found to be accurate to ± 0.3 arcsec or better.

2.3.3 Sky Subtraction

Accurate determination of the sky surface brightness is essential for tracing galaxy profiles to large radius, where the galaxy's surface brightness is often just a few percent of the sky. Our study is concerned mainly with the profiles in the centers of the galaxies, where their emission generally dominates over the sky. However, we have nonetheless attempted to determine the sky level as accurately as possible. To this end, we have adopted the method of sky determination used in McNamara & O'Connell (1992), in which counts in source-free regions of the sky are assumed to be dominated by Poisson noise. The distribution of counts in each region should then be well represented by a Gaussian, the width of which is an estimate of the statistical error in the sky level. Therefore, to determine the sky level, we extracted the counts in a number of source-free regions, constructed a histogram of sky values, and fit a Gaussian to the histogram. This method of fitting the distribution of sky values, in contrast to using a simple mode or mean, allows one to use the distribution's deviation from a normal distribution to identify the presence of contaminating sources.

We used the mean of the best-fit Gaussian as the modal sky value for a given region. We used 7-9 sky regions with areas of at least 1000 pixels each, distributed over the chip far from the CDG, and eliminated regions with sky modes more than 2σ from the adopted mean. We also filtered regions for which the sky distributions had values of normality (defined as in Martinez & Iglewicz, 1981) more than 2σ different from unity (the normality of a perfectly normal distribution). A deviant normality may

indicate the presence of low-level contamination in the sky region, such as emission from the galaxy’s extended halo. Comparison with sky values determined by fitting a plane to the entire CCD (median filtered over large blocks) showed typical differences between the two methods of $\lesssim 1 - 2\%$. However, our method of using smaller, source-free regions should not be as sensitive as the plane-fitting method to residual large-scale gradients that may remain due to the dark current problems discussed in Section 2.3.2.

We also used the difference between sky modes in the multiple regions to place a limit on the systematic error in our sky estimate. As in McNamara & O’Connell (1992), we used the maximum difference between adopted sky modes ($\Delta S_{\max} = S_{\max} - S_{\min}$) to define the systematic error in sky levels as $\Delta S_{\text{sys}} = \Delta S_{\max}/2$. When computing total errors in colors, systematic errors were added in quadrature with the statistical errors.

2.3.4 Image Stacking

After sky subtraction and before stacking, the pixel values were changed to units of counts per second by multiplying by the gain and dividing by the exposure time. The gain, which gives the conversion from ADU to electrons ($N_e = \text{gain} \times \text{ADU}$) was determined each night using the *findgain* task in IRAF. Next, the individual frames in each band were scaled to remove differences in intensity due to changes in airmass between exposures. The IRAF task *mscimatch* was used to perform this

scaling. This task uses the measured intensities of unsaturated stars to determine the scaling; typically, 50-200 stars per frame were used. Since the frames for a given object were always taken within a short time of one another, scalings were typically within a few percent of unity. We note that *mscimatch* was not used to determine zero-point offsets, as this step was done during sky subtraction.

In order to stack the frames into a final master image, the frames must be tangent-plane projected onto the same pixel grid using the WCS solution derived earlier. To minimize artifacts due to projection, cosmic rays were identified and removed using the *craverage* and *fixpix* tasks in IRAF. The *mscimage* task was used to perform the projection using a sinc interpolant. Next, in the rare cases where there were large point spread function (PSF) variations between frames, PSF matching was done to remove these variations. Finally, the frames were stacked using a median filter (or an average when only 2 frames were used) with a σ -clipping routine using the *mscstack* task in IRAF.

2.3.5 Calibration and Corrections

During photometric nights, we observed typically ~ 20 standard stars from the Landolt catalog ([Landolt, 1992](#)) with a wide range in color and over a wide range in airmass. These standard-star observations allow the observed fluxes to be calibrated relative to the standard *UVBRI* system. However, for the purposes of this disserta-

tion, where we compare colors measured between different radii of the same source, photometric calibration is not necessary and was not done.

Normally, because our sources are scattered across the sky, corrections must be made to remove extinction due to dust in our own galaxy, which varies as a function of position on the sky. However, we are measuring radial gradients and hence comparing colors between two radii in the same source. Since the Galactic extinction does not vary significantly over the typical angular scale of our galaxies ($r \lesssim 2$ arcmin), no correction for Galactic extinction is necessary.

2.4 Literature Data

To supplement our data, we use a variety data taken from the literature. We describe these data and their sources in the following sections:

Total Stellar Luminosities: The total luminosity of the CDG is used to infer the central black hole mass; see Section 5.2.3.

Stellar Velocity Dispersions: The velocity dispersion of stars in the CDG is also used to infer black hole mass, as well as the depth of the CDG potential (Section 3.2.3).

Star Formation and Cooling Rates: These rates are compared to accretion rates when we discuss BH and bulge growth (Section 5.3) and to one another when we compare star formation and cooling (Section 4.3).

CDG Color Gradients: We use color gradients from the literature for a number of objects that we did not observe; see Section 4.4.

Additionally, we use optical color profiles from the literature as a consistency check on our values (see Section 4.4.2).

CHAPTER 3

AGN Feedback

3.1 Introduction: Cavities in the ICM

Chandra images of galaxy clusters have revealed many large-scale interactions between the ICM and the central AGN, the best-known examples of which are the Perseus cluster (Boehringer et al., 1993; Fabian et al., 2000; Schmidt et al., 2002; Fabian et al., 2002a, 2003a,b, 2006), Abell 2052 (Blanton et al., 2001, 2003), and Hydra A (McNamara et al., 2000; David et al., 2001; Nulsen et al., 2002, 2005b). In these systems, the radio jets of the AGN have pushed out cavities in the cluster's atmosphere, creating surface-brightness depressions in X-ray images that are correlated with the lobes' radio emission, such that the radio emission fills the depression in X-rays. The lower emissivities of the depressions imply that they are low-density cavities in the ICM, and therefore should rise buoyantly in the cluster's atmosphere (Churazov et al., 2001). By measuring the surrounding pressure and volume of the cavities using the X-ray data, one can derive the work done by the radio source on the ICM in inflating the cavities, giving a direct measurement of the non-radiative energy released during the outburst. Measurements of this energy, combined with measurements of the star formation and cooling rates, can be used to investigate

possible feedback scenarios that may govern the growth of the CDG and its central supermassive black hole.

3.2 Quantifying AGN Heating

3.2.1 Measuring the Cavities

In total, 62 surface brightness depressions or cavities were identified in the 33 cavity systems. Table 3.1 lists the cavity properties. We measured the size and position of each cavity by overlaying ellipses onto the exposure-corrected, unsmoothed images. The ellipses were positioned such that they encompass the cavity, but not the bright rim (if present). We note that this measurement is qualitative and its accuracy depends on the contrast of the cavity with its surroundings, which in turn depends on the exposure time of the available images. Cavities with bright surrounding rims (e.g., A2052) were easily identified and measured, while those without rim emission (e.g., MS0735.6+7421) were difficult to measure accurately. To account for this difference, we assigned a figure of merit (FOM) of 1, 2, or 3 to each cavity, with 1 indicating a cavity with a bright rim and 3 indicating a poorly defined cavity without a rim.

The cavities in our sample range in radius from ~ 2 kpc (e.g, M87) to ~ 100 kpc (MS 0735.6+7421) and in their distance to the core from ~ 2 kpc (e.g, M87) to ~ 200 kpc (MS 0735.6+7421). Histograms of the cavity sizes and positions are shown in Figure 3.1. On average, our cavities lie at a distance from the core of

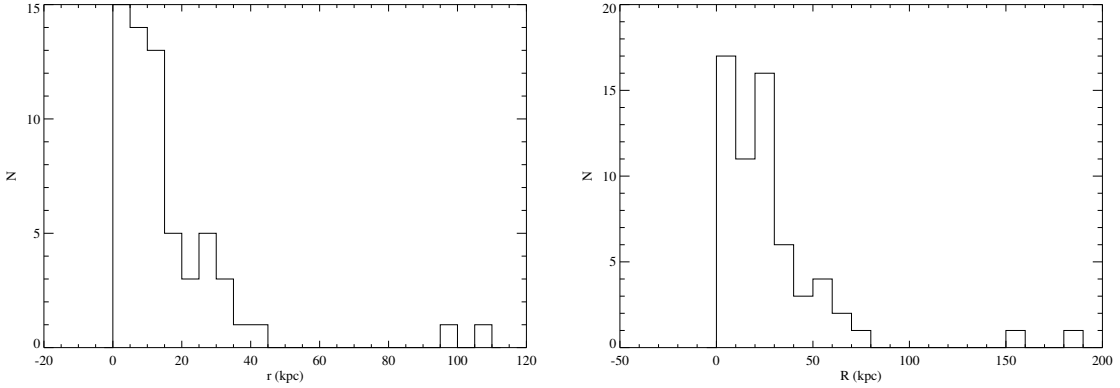


Figure 3.1: *Left:* Histogram of cavity equivalent radii, defined as $r = \sqrt{ab}$, where a and b are the semiaxes. *Right:* Histogram of cavity distances, R , from the X-ray core. The two cavities at radii of ~ 100 kpc belong to the MS 0735.6+7421 system.

approximately twice their radii. We note that since the detectability of a cavity depends on its location and size (Enßlin & Heinz, 2002), with larger and more central cavities having greater contrast with their surroundings, our sample is biased towards these cavities. Additionally, we have probably missed cavities completely in some systems. In particular, we have likely missed small cavities at large radii (due to lack of contrast) and small cavities at higher redshifts (due to lack of resolution). However, it is unlikely that we have missed many large, central cavities, which are most important to the estimation of the cavity power (see Section 3.2.4).

Table 3.1. Cavity Properties.

System	Cavity FOM ^a	a^b (kpc)	b^c (kpc)	R^d (kpc)	pV (10^{58} erg)	t_{c_s} (10 ⁷ yr)	t_{refill} (10 ⁷ yr)	t_{buoy} (10 ⁷ yr)
A85	2	8.9	6.3	21	$1.2^{+1.2}_{-0.4}$	2.3	5.1	4.2
A133	3	41	21	32	24^{+11}_{-1}	3.8	14	5.1
A262	2	5.4	3.4	8.7	$0.060^{+0.050}_{-0.017}$	1.5	2.9	1.7
Perseus	2	5.7	3.4	8.1	$0.065^{+0.018}_{-0.016}$	1.4	2.8	1.6
	1	9.1	7.3	9.4	$3.7^{+4.7}_{-1.7}$	1.0	4.9	1.6
	1	8.2	4.7	6.5	$1.6^{+1.0}_{-0.1}$	0.7	3.6	1.1
	2	17	7.3	28	$3.9^{+3.5}_{-0.1}$	3.1	10	8.3
	2	17	13	39	$9.7^{+10.4}_{-3.4}$	4.0	13	10
	2	9.3	6.5	23	$1.0^{+1.0}_{-0.3}$	3.2	6.3	5.4
2A 0335+096	2	4.8	2.6	28	$0.072^{+0.037}_{-0.002}$	3.7	4.6	11
A478	2	5.5	3.4	9.0	$0.74^{+0.57}_{-0.07}$	1.0	2.9	1.8
	2	5.6	3.4	9.0	$0.76^{+0.55}_{-0.17}$	1.0	3.0	1.8
MS 0735.6+7421	2	110	87	160	770^{+960}_{-360}	13	58	26
	2	130	89	180	830^{+770}_{-220}	15	66	33
PKS 0745-191	3	26	17	31	69^{+56}_{-10}	3.0	12	5.2
4C 55.16	2	10	7.5	16	$4.7^{+4.9}_{-1.7}$	1.7	5.6	3.0
	2	13	9.4	22	$7.1^{+7.4}_{-2.7}$	2.3	7.3	4.1
Hydra A ^e	2	18	12	29	$8.1^{+7}_{-1.6}$	3.0	8.7	5.1
	2	20	12	31	$8.6^{+6}_{-0.3}$	3.2	9.3	5.6
	3	42	21	78	20^{+8}_{-1}	7.8	21	17
	3	34	24	66	27^{+27}_{-8}	6.6	19	12
RBS 797	2	13	8.5	24	18^{+14}_{-2}	2.2	7.5	5.0
Zw 2701	2	9.7	9.7	20	20^{+36}_{-13}	1.8	6.5	3.4
	2	46	41	54	220^{+340}_{-130}	5.2	23	7.8
Zw 3146	2	51	21	40	170^{+180}_{-10}	3.7	17	6.8
	2	36	30	59	210^{+280}_{-100}	5.0	21	10
M84	2	1.6	2.3	$0.002^{+0.004}_{-0.0015}$		0.5	0.4	

Table 3.1 (continued)

System	Cavity FOM ^a	a^b (kpc)	b^c (kpc)	R^d (kpc)	pV (10^{58} erg)	t_{cs} (10^7 yr)	t_{refill} (10^7 yr)	t_{buoy} (10^7 yr)
M87	2	2.1	1.2	2.5	$0.001^{+0.0001}_{-0.0005}$	0.6	1.0	0.5
	2	2.3	1.4	2.8	$0.016^{+0.012}_{-0.003}$	0.4	0.9	0.4
Centaurus	2	1.6	0.8	2.2	$0.004^{+0.002}_{-0.001}$	0.4	0.7	0.4
	1	3.3	2.4	6.0	$0.038^{+0.039}_{-0.012}$	1.0	2.2	1.3
HCG 62	2	5.0	4.3	3.5	$0.022^{+0.012}_{-0.003}$	0.6	1.5	0.7
	2	4.0	4.0	8.4	$0.027^{+0.039}_{-0.015}$	1.8	2.9	1.5
A1795	3	19	7.2	19	$4.7^{+6.6}_{-1.6}$	1.9	6.8	3.7
	3	16	12	23	27^{+30}_{-10}	2.1	8.3	4.1
A1835	3	14	9.7	17	20^{+20}_{-6}	1.5	6.5	2.7
	2	3.5	2.6	4.6	$0.054^{+0.060}_{-0.020}$	0.8	2.0	0.9
PKS 1404-267	2	3.2	2.7	3.8	$0.062^{+0.085}_{-0.031}$	0.6	1.8	0.6
	2	9.4	9.4	16	15^{+27}_{-19}	1.5	5.7	2.5
MACS J1423.8+2404	2	9.4	9.4	17	14^{+25}_{-19}	1.6	5.9	2.8
	2	9.4	7.2	32	$4.8^{+2.7}_{-0.1}$	2.5	6.8	6.9
A2029	3	13	7.2	11	$1.2^{+1.4}_{-0.4}$	1.8	5.5	1.9
	1	11	7.9	11	$0.53^{+0.88}_{-0.32}$	1.2	3.6	1.0
A2052	1	6.5	6.2	6.7	38^{+39}_{-4}	6.0	21	12
	2	9.4	9.4	17	$14^{+2.7}_{-9}$	2.1	7.1	3.2
MKW 3S	3	54	23	59	$3.7^{+3.7}_{-1.1}$	2.3	7.7	3.8
	2	15	10	19	$3.8^{+2.9}_{-0.4}$	2.3	7.7	3.8
A2199	2	16	10	21	$1.3^{+1.8}_{-1.7}$	6.1	18	13
	3	47	19	58	18^{+22}_{-22}	6.0	19	13
Hercules A	3	26	21	60	$2.9^{+5.3}_{-1.9}$	2.9	7.6	3.6
	3	47	15	27	$2.3^{+2.2}_{-0.2}$	2.4	6.9	3.1
3C 388	2	15	10	21	$5.4^{+9.8}_{-3.5}$	1.6	6.4	2.1
	2	12	12	15	$5.4^{+9.8}_{-3.5}$	1.6	6.4	2.1
3C 401	2	12	12	15	28^{+18}_{-1}	3.4	15	8.5
	1	29	17	43	56^{+52}_{-13}	3.4	15	3.6
Cygnus A	1	34	1	23				7.8

Table 3.1 (continued)

System	Cavity FOM ^a	a^b (kpc)	b^c (kpc)	R^d (kpc)	pV (10^{58} erg)	t_{c_s} (10^7 yr)	t_{refill} (10^7 yr)	t_{buoy} (10^7 yr)
Sersic 159/03	3	20	14	23	10^{+9}_{-2}	2.9	9.3	3.8
	3	22	17	26	15^{+17}_{-6}	3.3	11	4.2
A2597	2	7.1	7.1	23	$1.5^{+2.6}_{-0.9}$	2.5	7.9	6.8
	2	10	7.1	23	$2.1^{+2.0}_{-0.6}$	2.4	8.6	6.6
A4059	2	20	10	23	$2.2^{+1.0}_{-0.3}$	2.7	8.4	4.2
	2	9.2	9.2	19	$0.84^{+1.33}_{-0.55}$	2.3	6.2	3.5

^aFigure of merit. The FOM gives a relative measure of the cavity's contrast to its surroundings: (1) high contrast: bright rim surrounds cavity; (2) medium contrast: bright rim partially surrounds cavity; and (3) low contrast: no rim, or faint rim surrounds cavity.

^bProjected semi-major axis of the cavity.

^cProjected semi-minor axis of the cavity.

^dProjected radial distance from the core to the cavity's center.

^eThe deeper image of Wise et al. (2007) of Hydra A shows two large outer cavities beyond those measured here, but for consistency we report only those cavities apparent in archival data.

3.2.2 Energies

The radio-emitting jets are understood to be displacing the ICM at the location of the cavities, doing work against the surrounding plasma, as well as supplying thermal energy to the radio plasma that fills the lobes (McNamara et al., 2000; Blanton et al., 2003). The total energy required to create a cavity is equal to its enthalpy, given by

$$E_{\text{cav}} = \frac{\gamma}{(\gamma - 1)} pV, \quad (3.1)$$

where p is the pressure of the gas surrounding the cavity, V is the cavity's volume, and γ is the ratio of specific heats of the gas inside the cavity. For a relativistic gas, $\gamma = 4/3$, and the enthalpy is $4pV$. We assume this value of γ for all subsequent calculations involving E_{cav} . The pressure (p) was derived as in Section 2.2.3. The volume (V) was calculated from the projected elliptical shape as a prolate ellipsoid, with semimajor axis a and semiminor axis b . However, since we see the cavity in projection, its true three-dimensional shape is unknown. We account for this uncertainty by allowing each bubble to have an intrinsic a/b as large as that of the most eccentric cavity observed in the sample, $(a/b)_{\max}$. The upper and lower limits are then calculated assuming either oblate or prolate symmetry.

3.2.3 Ages

The cavities are generally believed to be rising buoyantly in the cluster's atmosphere, based on observational evidence including the presence of cool rims around a

number of cavities (e.g., Blanton et al., 2001) and the lack of strong shocks around the bubbles (for a review, see McNamara & Nulsen, 2007) that preclude rapidly expanding and rising cavities. Additionally, a number of simulations find that buoyant cavities reproduce typical cavity locations and sizes well (e.g., Churazov et al., 2001). However, to include a range of possible ages, we estimate the age of the cavity in three cases:

1. The cavity rises at the speed of sound ($v_{\text{cs}} = (\gamma kT/\mu m_{\text{H}})^{1/2}$) for a distance R (the projected distance from the core to the cavity's present location), giving:

$$t_{\text{cs}} = R/v_{\text{cs}} = R\sqrt{\mu m_{\text{H}}/\gamma kT}, \quad (3.2)$$

where we have taken $\gamma = 5/3$ and $\mu = 0.62$. Since strong shocks are not generally seen in these systems, this estimate is a lower limit to the age.

2. The cavity rises buoyantly with a velocity of:

$$v_{\text{t}} \sim (2gV/SC)^{1/2}, \quad (3.3)$$

where V is the volume of the bubble, S is the cross section of the bubble, and $C = 0.75$ is the drag coefficient (Churazov et al., 2001). The gravitational acceleration was calculated using the stellar velocity dispersion of the central galaxy, under the approximation that the galaxy is an isothermal sphere, as $g \approx 2\sigma^2/R$ (Binney & Tremaine, 1987). Published values of the velocity dispersion were used when available (see Table 2.2); otherwise, the average value ($\langle \sigma \rangle =$

280 km s^{-1}) was adopted. The cavity age is then given by

$$t_{\text{buoy}} = R/v_t \sim R\sqrt{SC/2gV}. \quad (3.4)$$

3. The cavity rises as quickly as it can be refilled (McNamara et al., 2000; Nulsen et al., 2002):

$$t_r \sim 2R\sqrt{r/GM(R)} = 2\sqrt{r/g}, \quad (3.5)$$

where $r = (ab)^{1/2}$ is the radius of the cavity.

The ages are listed in Table 3.1. In general, the sound-speed ages are the shortest and the refill ages are the longest, with a factor of $\sim 2 - 3$ difference. For simplicity, we use the buoyancy ages for all calculations, unless otherwise noted.

3.2.4 Cavity Powers

The mean jet power required to create a cavity or cavity pair is then

$$P_{\text{cav}} = \frac{E_{\text{cav}}}{t}, \quad (3.6)$$

where t is the average time between outbursts. This time is known only for a few objects, such as Perseus, for which the interval between outbursts may be estimated from the presence of multiple generations of cavities and ripples (Fabian et al., 2006).

In objects with only a single set of cavities, which make up most of our sample, the cavity's buoyancy age is used for t .

Table 3.2 lists the total cavity energies and the associated powers for the systems in our sample (see Table 3.1 in the Appendix for the properties of each cavity). For

A1068, in which no cavities are apparent in the X-ray image, the outburst power was estimated using the $\nu = 1400$ MHz radio flux from the NVSS survey ($S_{1400} = 23.1 \pm 1.1$ mJy), as $P_{\text{cav,tot}} \sim 1500 \times \nu_{\text{MHz}} P_\nu$, the average relation found from the sample of [Bîrzan et al. \(2004\)](#) for radio-filled cavities.

Table 3.2. Cavity and ICM Properties Derived from *Chandra* Data.

System	pV_{tot} (10^{58} erg)	$P_{\text{cav,tot}}^{\text{a}}$ (10^{42} erg s $^{-1}$)	L_X^{b} (10^{42} erg s $^{-1}$)	$\dot{M}_{\text{cool}}^{\text{c}}$ (M_{\odot} yr $^{-1}$)	$L_{\text{cool}}^{\text{b}}$ (10^{42} erg s $^{-1}$)	$r_{\text{cool}}^{\text{d}}$ (kpc)
A85	$1.2^{+1.2}_{-0.4}$	37^{+37}_{-11}	365 ± 20	18^{+13}_{-9}	30^{+20}_{-10}	142
A133	24^{+11}_{-10}	620^{+260}_{-20}	106 ± 2	5 ± 3	3 ± 2	93
A262	$0.13^{+0.10}_{-0.03}$	$9.7^{+7.5}_{-2.6}$	$11.1^{+0.4}_{-0.3}$	< 0.7	< 0.3	57
Perseus	19^{+20}_{-5}	150^{+160}_{-30}	554 ± 2	20^{+9}_{-8}	21^{+8}_{-7}	90*
2A 0335+096	$1.1^{+1.0}_{-0.3}$	24^{+23}_{-6}	338 ± 2	29^{+7}_{-5}	13 ± 4	135
A478	$1.5^{+1.1}_{-0.4}$	100^{+80}_{-20}	1440 ± 10	40^{+40}_{-20}	40^{+50}_{-20}	150
MS 0735.6+7421	1600^{+1700}_{-600}	6900^{+7600}_{-2600}	450 ± 10	$20^{+20}_{-10}*$	12^{+13}_{-8}	141
PKS 0745-191	69^{+56}_{-56}	1700^{+1400}_{-1400}	2300 ± 30	170 ± 90	230 ± 120	176
4C 55.16	12^{+12}_{-4}	420^{+440}_{-160}	640 ± 20	70 ± 30	70 ± 20	162
Hydra A	64^{+48}_{-11}	430^{+200}_{-50}	282 ± 2	16 ± 5	13 ± 4	109
RBS 797	38^{+50}_{-15}	1200^{+1700}_{-500}	3100^{+100}_{-130}	$200^{+490}_{-180}*$	250^{+400}_{-220}	185
Zw 2701	350^{+530}_{-200}	6000^{+8900}_{-3500}	430^{+20}_{-30}	$< 8^{*}$	< 6	135
Zw 3146	380^{+460}_{-110}	5800^{+6800}_{-1500}	3010^{+70}_{-90}	590^{+190}_{-170}	680^{+170}_{-150}	186
A1068	...	20^{e}	...	< 48	...	152
M84	$0.003^{+0.005}_{-0.002}$	$1.0^{+1.5}_{-0.6}$	0.07 ± 0.01	$0.038 \pm 0.002^{*}$	$0.012^{+0.003}_{-0.001}$	10
M87	$0.020^{+0.014}_{-0.003}$	$6.0^{+4.2}_{-0.9}$	$8.30^{+0.03}_{-0.04}$	$1.2^{+0.1}_{-0.3}$	$1.1^{+0.1}_{-0.2}$	26*
Centaurus	$0.060^{+0.051}_{-0.015}$	$7.4^{+5.8}_{-1.8}$	28.1 ± 0.3	$2.7^{+0.2}_{-0.1}$	4.3 ± 0.2	54*
HCG 62	$0.046^{+0.073}_{-0.028}$	$3.9^{+6.1}_{-2.3}$	1.8 ± 0.2	< 0.3	< 0.1	33
A1795	$4.7^{+6.6}_{-1.6}$	160^{+230}_{-50}	625^{+6}_{-11}	8^{+13}_{-7}	10^{+14}_{-9}	135
A1835	47^{+16}_{-16}	1800^{+1900}_{-600}	3160^{+60}_{-90}	156
PKS 1404-267	$0.12^{+0.15}_{-0.05}$	20^{+26}_{-9}	27 ± 1	5 ± 2	3 ± 1	83
MACS J1423.8+2404	29^{+52}_{-19}	1400^{+2300}_{-900}	2290 ± 30	140^{+110}_{-90}	90^{+70}_{-60}	187
A2029	$4.8^{+2.7}_{-0.7}$	87^{+49}_{-4}	1160 ± 10	< 1.9	< 3	140
A2052	$1.7^{+2.3}_{-0.7}$	150^{+200}_{-70}	97 ± 1	$7.0^{+0.9}_{-0.4}$	$3.4^{+0.5}_{-0.2}$	87
MKW 3S	38^{+39}_{-39}	410^{+420}_{-420}	104 ± 2	5^{+3}_{-2}	5^{+3}_{-2}	120
A2199	$7.5^{+6.6}_{-1.5}$	270^{+250}_{-60}	142 ± 1	< 3	< 3	91
Hercules A	31^{+40}_{-9}	310^{+400}_{-90}	210^{+10}_{-20}	$< 58^{*}$	< 46	104
3C 388	$5.2^{+7.5}_{-2.1}$	200^{+280}_{-80}	27^{+2}_{-3}	$< 3^{*}$	< 2	55

Table 3.2 (continued)

System	pV_{tot} (10^{58} erg)	$P_{\text{cav,tot}}^{\text{a}}$ (10^{42} erg s $^{-1}$)	L_X^{b} (10^{42} erg s $^{-1}$)	$\dot{M}_{\text{cool}}^{\text{c}}$ (M_{\odot} yr $^{-1}$)	$L_{\text{cool}}^{\text{b}}$ (10^{42} erg s $^{-1}$)	$r_{\text{cool}}^{\text{d}}$ (kpc)
3C 401	11^{+20}_{-7}	650^{+1200}_{-420}	37^{+2}_{-7}	12^{+5*}_{-6}	7 ± 3	62
Cygnus A	84^{+70}_{-14}	1300^{+1100}_{-200}	420 ± 4	31^{+7}_{-6}	50 ± 10	91
Sersic 159/03	25^{+26}_{-8}	780^{+820}_{-260}	220 ± 6	15 ± 9	9 ± 5	136
A2597	$3.6^{+4.6}_{-1.5}$	67^{+87}_{-29}	470^{+8}_{-17}	30^{+30}_{-20}	30^{+30}_{-20}	128
A4059	$3.0^{+2.5}_{-0.9}$	96^{+89}_{-35}	93 ± 1	3^{+2}_{-2}	2 ± 1	85

^aCavity power calculated assuming $4pV$ of energy per cavity and the buoyancy timescale.^bBolometric luminosity between 0.001 and 100 keV inside r_{cool} .^cNet cooling rate to low temperatures. Values marked with an asterisk where derived from observations with a low number of counts inside the cooling radius ($\lesssim 15000$) and are therefore less reliable.^dRadius of the cooling region, inside which the cooling time is less than 7.7×10^9 yr (except for values marked with an asterisk, which correspond to the radius at the chip's edge).^eFor A1068, the cavity power was calculated from the $\nu = 1400$ MHz radio power as $P_{\text{cav,tot}} \sim 1500 \times \nu_{\text{MHz}} P_{\nu}$.

3.3 Measuring Cooling

3.3.1 X-ray Spectra

The luminosity of the cooling gas inside the cooling radius is needed to investigate whether or not AGN heating can balance cooling. Within the cooling radius, radiative energy losses must be replaced to prevent the deposition of large quantities of cool gas. We define the cooling radius as the radius within which the gas has a cooling time less than 7.7×10^9 yr, the look-back time to $z = 1$ for our adopted cosmology. This redshift is roughly the distance to which clusters have been found with properties similar to present day clusters. The corresponding lookback time should then approximate the time a cooling flow has had to establish itself. The cooling time was calculated using the cooling curves of [Boehringer & Hensler \(1989\)](#). Table 3.2 gives the values of r_{cool} for each cluster. Within this radius, we performed deprojections by fitting both a cooling model and a single temperature model to the spectra.

Cooling Flow Model

In order to obtain a spectroscopic estimate of the cooling luminosity, we performed the deprojection (see Section 2.3.2) using a cooling flow model (PROJECT×WABS×[MEKAL+MKCFLOW]), fit between 0.5 and 7.0 keV. To force all cooling to be within the cooling radius, the MKCFLOW model was used only inside the cooling radius and was set to zero outside. The MKCFLOW low temperature was fixed to

0.1 keV, resulting in an estimate of the luminosity of gas cooling to low temperatures. Within each annulus, the MEKAL and MKCFLOW abundances were tied together, and the MKCFLOW high temperature was tied to the temperature of the MEKAL component. Lastly, the column density (N_{H}) was tied between annuli and allowed to vary. The spectroscopic estimate of the bolometric cooling luminosity inside the cooling radius, L_{cool} , was then calculated from the unabsorbed fluxes obtained from the MKCFLOW model, integrated between energies of $\sim 0.1 - 100$ kev. In the case of A1835, the spectra were of insufficient quality to obtain a reliable cooling rate (see [McNamara et al., 2006](#)).

ICM Luminosity

To find the total luminosity inside the cooling radius, we performed the deprojection using a single-temperature model (PROJCT \times WABS \times MEKAL) fit between 0.5 and 7.0 keV to the same spectra used with the cooling flow model, again with N_{H} tied between regions and fixed to the Galactic value of [Dickey & Lockman \(1990\)](#). The unabsorbed fluxes from the MEKAL components for the annuli within the cooling radius, extrapolated between $\sim 0.1 - 100$ kev, were used to find the bolometric luminosity of the X-ray emitting gas, L_{X} . Table 3.2 gives L_{X} and L_{cool} (with 1σ errors estimated by XSPEC) for each object in our sample. Typically, L_{cool} is approximately 10% of L_{X} for our sample. Our values for L_{cool} and L_{X} are in reasonable agreement with published values for most of our sample.

3.3.2 Consistency Check: XMM-*Newton* and FUSE

Gas cooling out of the ICM at $T \sim 10^7$ K loses its energy primarily through thermal emission in the soft X-ray band. Therefore, its rate of cooling is best measured from X-ray spectra. Grating observations made with XMM-*Newton* provide high spectral resolution and hence the best constraints on the cooling rates. [Peterson et al. \(2003\)](#) have derived cooling rates from XMM-*Newton* grating observations for nine of the objects in our sample, and we list the most constraining rate (i.e. the smallest rate in any of the temperature bands) from this study in Table 4.1. With the exception of Hydra A and 2A 0335+096, these rates are upper limits.

At lower temperatures ($T \sim 10^5$ K), cooling gas should emit strongly in the far ultraviolet, mainly through the OVI doublet (see [Edgar & Chevalier, 1986](#)), where high-quality spectroscopic observations can be made. Such emission has been detected by FUSE for an additional six objects in our sample. The inferred FUSE cooling rates, calculated assuming the OVI emission is due to cooling gas (see e.g., [Oegerle et al., 2001](#); [Bregman et al., 2005, 2006](#)), are also listed in Table 4.1.

We have also derived cooling rates from lower-spectral-resolution *Chandra* data (see Section 3.3.1). For comparison, we plot the cooling rates from XMM-*Newton* and FUSE against those from our *Chandra* analysis in Figure 3.2. Despite significant differences in aperture and in the details of the modeling, the agreement between the X-ray-derived rates is reasonably good, as is their agreement with the UV-derived FUSE rates. We note, however, that the *Chandra* rates appear to be systematically

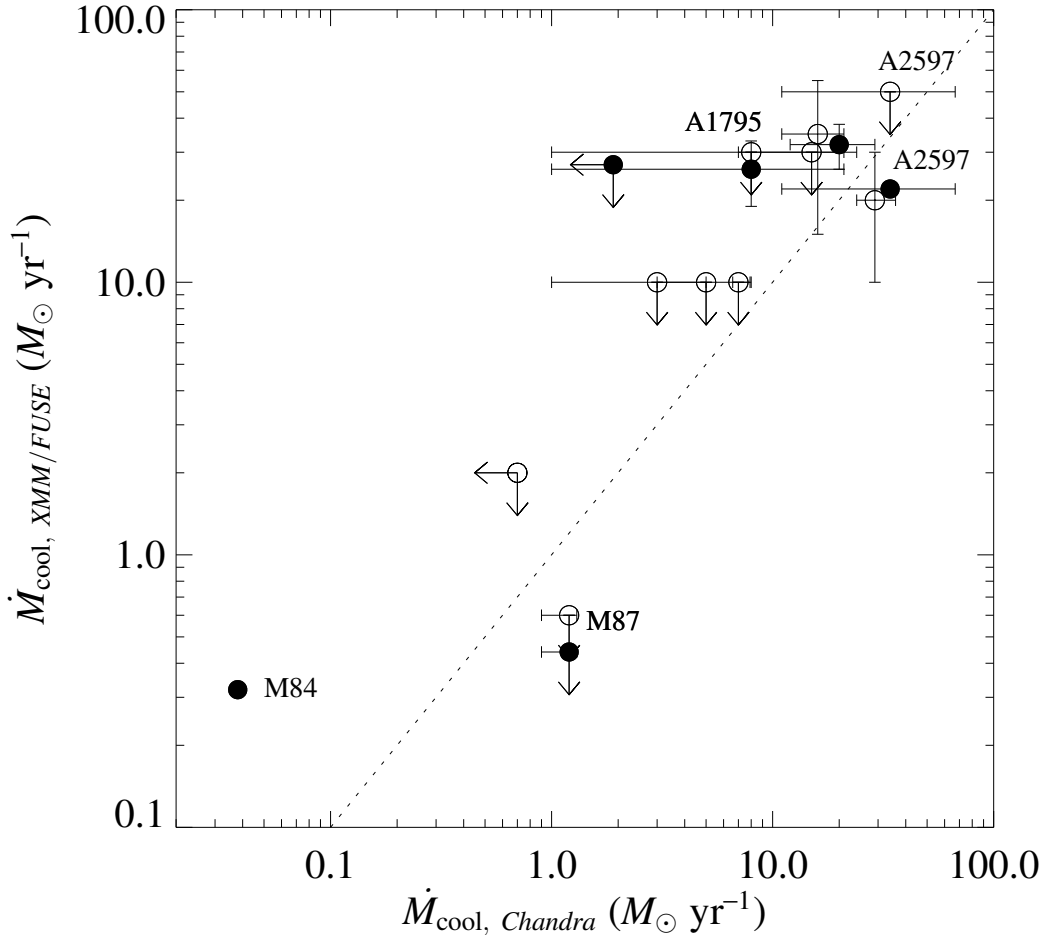


Figure 3.2: Cooling rates derived from *XMM-Newton* (empty symbols) and FUSE (filled symbols) spectra versus those derived from *Chandra* spectra. M87, A1795, and A2597 have both *XMM-Newton* and FUSE rates and hence appear twice. M84 is listed in [Bregman et al. \(2005\)](#) as a probable FUSE detection. The dotted line denotes equality between the two rates.

lower than the other two rates, possibly due to spatial and spectral resolution effects or calibration and modeling differences.

It should be emphasized that neither the *Chandra* nor *XMM-Newton* rates are based on fits to emission lines from gas cooling to low temperatures. Additionally, models fit to X-ray spectra do not generally require a cooling component to obtain an

adequate fit, except in the inner-most regions. Therefore, X-ray-derived cooling rates should be interpreted as the *maximum rates of cooling consistent with the spectra and not as unequivocal detections of cooling*. Until line emission that is uniquely due to cooling below 1 keV is identified, cooling through this temperature at any level cannot be confirmed (see however Morris & Fabian, 2005, who find possible weak detections of several cooling lines in XMM-Newton data of A2597). However, the reasonably close correspondence between FUSE and X-ray-derived rates indicates that cooling is occurring at or just below the detection limits.

3.4 Comparing Heating and Cooling

3.4.1 Quenching Cooling Flows

We now turn to the question of whether radio sources deposit enough energy into the ICM to quench cooling. We use L_X , the total luminosity of the X-ray-emitting gas from within the cooling radius, as an estimate of the classical, or morphological, cooling luminosity in the absence of heating and L_{cool} , the spectral estimate of the cooling luminosity within the cooling radius, as the luminosity of the gas cooling to low temperatures. The ICM luminosity, $L_{\text{ICM}} = L_X - L_{\text{cool}}$, must be offset by heating in order to prevent the gas from cooling to low temperatures. We note that this quantity ignores non-X-ray cooling, such as ultraviolet and optical emission, predicted to result from cooling by thermal conduction inside magnetic flux loops

(Soker et al., 2004), or along reconnected magnetic field lines between cold clouds and the ICM (Soker, 2003). Any such emission would lower the cooling luminosity which must be balanced by heating. Figure 3.3 shows the mechanical luminosity plotted against L_{ICM} for our sample. The diagonal lines represent equality between cooling and heating, assuming energy inputs of pV , $4pV$, and $16pV$ per cavity.

Figure 3.3 shows several objects, such as Hydra A, Cygnus A, and MS 0735.6+7421, the cavities of which can contain enough energy to balance radiative losses, at least temporarily, with only $1pV$ of heat input per cavity. The remaining objects, which require between a few and $\sim 20pV$ per cavity to balance cooling, would do so with varying degrees of difficulty. As discussed above, up to $4pV$ is available if the cavities are relativistic and nonadiabatic, and there may be further energy input if they are overpressured or produce a shock when they are formed. Therefore, the objects that require $\sim 4pV$ or less may reasonably be supplied with enough energy in the cavities to balance cooling, depending on the detailed dynamics (the heat also needs to be distributed inside the cooling radius to match the distribution of radiative losses). Provided that the true radio cycling timescale ranges between t_{c_s} and t_r , the cavities in at least one-half of the objects in our sample contain enough energy to offset radiation losses. Bear in mind that our conclusions depend on the adopted cooling radius (see Section 3.3), measurement uncertainties in the cavity sizes, and the cavity production timescale. Nevertheless, we can safely conclude that cooling can plausibly be balanced by the current bubble heating in some, but not all, systems.

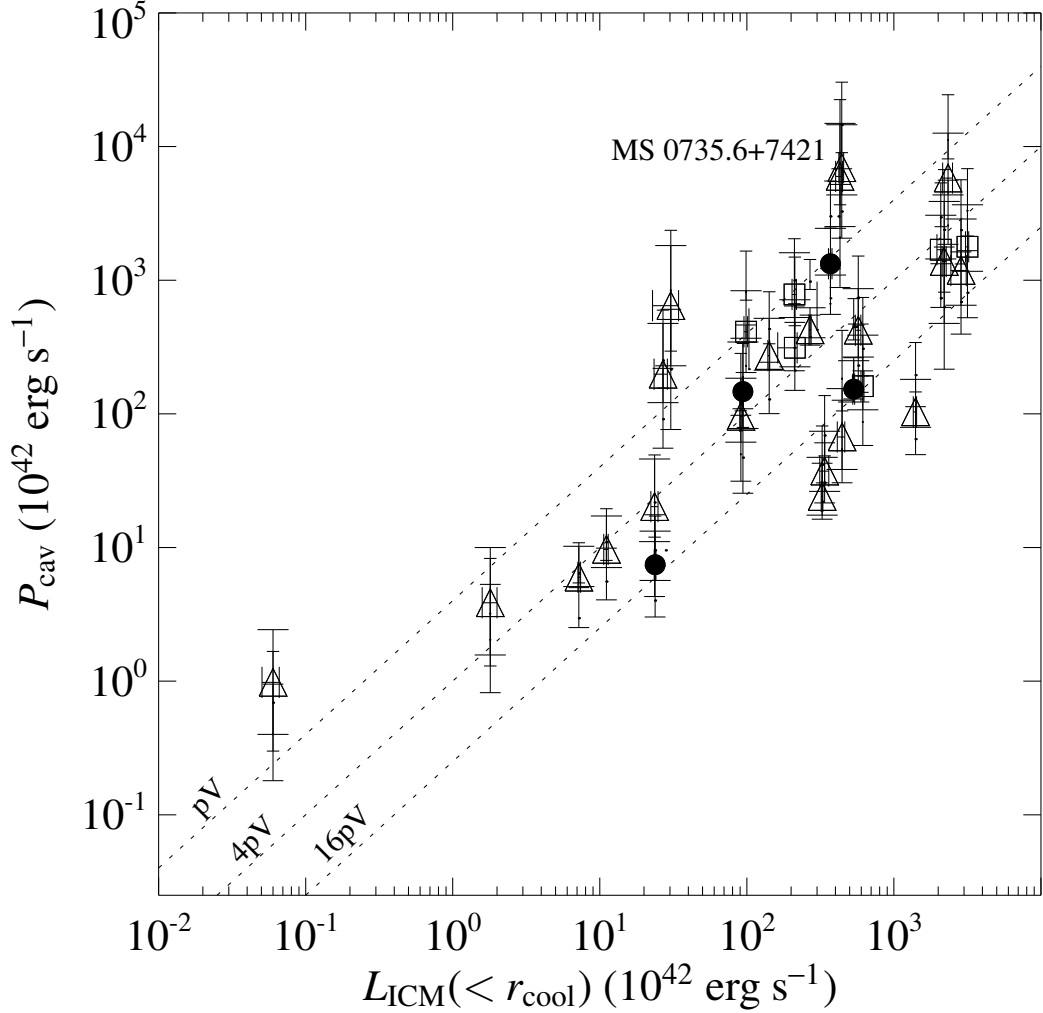


Figure 3.3: Cavity power of the central AGN versus the X-ray luminosity of the intracluster medium inside the cooling radius that must be offset to be consistent with the spectra ($L_{\text{ICM}} = L_{\text{X}} - L_{\text{cool}}$). The symbols and wide error bars denote the values of cavity power calculated using the buoyancy timescale. The short and medium-width error bars denote the upper and lower limits of the cavity power calculated using the sound speed and refill timescales, respectively. Different symbols denote different figures of merit: *circle* – well-defined cavity with bright rims, *triangle* – well-defined cavity without bright rims, *square* – poorly defined cavity. The diagonal lines denote $P_{\text{cav}} = L_{\text{ICM}}$ assuming pV , $4pV$, or $16pV$ as the total enthalpy of the cavities.

Another possibly important source of heating is thermal conduction, which, as demonstrated by Voigt & Fabian (2004), could supply a significant amount of heat. Using a sample similar to our own, Voigt & Fabian found that thermal conduction can reduce the cooling luminosity by factors of $\sim 2 - 3$ in some objects. Although they are difficult to find in X-ray images, shocks associated with the expanding cavities can deposit additional energy into the ICM. Deep *Chandra* images of a growing number of objects, including Cygnus A (Wilson et al., 2003, 2006), NGC 4636 (Jones et al., 2002), M87 (Forman et al., 2006), and Perseus (Fabian et al., 2003a), show surface brightness discontinuities that may be associated with weak shocks. In Cygnus A and M87, the shocks imply that the radio source may provide several times the upper limit of the luminosity seen in the bubbles, under the assumption of $4pV$ of energy per bubble (Wilson et al., 2003; Forman et al., 2006). Therefore, our cavity powers should be thought of as lower limits on the total mechanical power output of the AGN.

As discussed above, a number of systems lie well above the $4pV$ line and even above the pV line, implying that their cavities likely represent more energy than required to balance cooling. These systems, many of which possess supercavities and shocks extending beyond the cooling radius, have enough energy to quench cooling and to contribute to cluster preheating. An example is MS 0735.6+7421, the most powerful such outburst known to date. The AGN in this cluster has dumped $\sim 1/3$ keV per particle into the ICM (including the energy of the shock; McNamara et al.,

2005; Gitti et al., 2007). The cavities alone have enough energy to quench cooling 15 times over. This amount of energy, even if distributed only partly inside the cooling radius, should have a profound effect on any cooling gas. Such objects may thus be in a heating phase.

It is important to note that our sample is biased toward systems with visible evidence for X-ray cavities and does not represent clusters as a whole. Many clusters, including some with large cooling flows, do not contain cavities (e.g. Abell 1068, Wise et al., 2004; McNamara et al., 2004). These objects may have very different reheating histories than the objects discussed here. In this sense, the objects presented here represent the best-case examples for reheating the ICM by energetic bubbles. Our analysis does not prove that all cooling flows can be quenched in this fashion. However, the absence of cavities currently does not rule out significant feedback in the past. Donahue et al. (2006) find elevated entropy levels throughout the cooling region of both cooling-flow clusters that show evidence of AGN feedback and those that do not, consistent with a history of AGN feedback in all cooling flows. Secondly, in cooling flows that lack evidence of AGN heating, other sources of heat, such as thermal conduction, may be important. Lastly, the most powerful explosions, such as seen in MS 0735.6+7421, may turn off accretion and hence AGN activity for extended periods (note, however, that the central cooling time in MS 0735.6+7421 is just $\sim 5 \times 10^8$ yr, implying that cooling will occur again within that time frame if there is no further heating).

3.4.2 Duty Cycle

We can estimate the duty cycle with which the AGN creates the cavities by noting that we find cavities in 33 systems out of the approximately 150 clusters that we examined in the *Chandra* archive, implying a duty cycle of $\sim 20\%$. However, in this survey, we did not distinguish between cooling-flow and noncooling-flow clusters (i.e. those with and without short central cooling times), and we may have missed many existing cavities due to insufficient signal-to-noise in the archival images. The duty cycle may be much greater in cooling flow clusters than in clusters as a whole, since it is there that heating is required to balance cooling. Indeed, Dunn & Fabian (2006) find that $\sim 70\%$ of cooling-flow clusters in the Brightest 55 flux-limited sample of clusters (see Edge et al., 1990) have visible cavities, implying a duty cycle of at least 70% in cooling flows.

Using this duty cycle, we can estimate the ratio of the average heating rate to the average cooling rate across all cooling-flow clusters. For our sample of 33 systems, we find a ratio of average heating power to average cooling power of

$$\frac{\langle P_{\text{cav}} \rangle}{\langle L_{\text{ICM}} \rangle} = 1.6 \quad (3.7)$$

Adjusting this average for a duty cycle of 70% (by assuming that those systems without cavities have zero cavity power), we find a ratio of 1.1 across all cooling-flow clusters. If the energy is deposited efficiently in the cooling region, this result implies

that time-averaged AGN heating can balance cooling in cooling-flow clusters as a whole.

Furthermore, the AGN must create cavities frequently enough to prevent large amounts of cooling and to maintain the gas at the observed temperatures. This condition can only be met when the average time between outbursts is less than the average central cooling time (assuming the time to heat the gas is comparatively short). We plot in Figure 3.4 the current central cooling time derived in Section 4.4.3 versus the average cavity buoyancy age for each system with two or fewer cavities. For systems with multiple generations of cavities (Perseus and Hydra A), we plot the average of the difference in ages between the inner and outer sets of cavities. With the possible exception of A2029, the average cavity age in each system is less than the cooling time, a result that is consistent with feedback. However, there is no obvious trend between the two times, possibly because we do not know the true average time between outbursts for the majority of systems in our sample (the cavity age is only a lower limit on the time between outbursts).

3.4.3 Trends between X-ray and Mechanical Luminosities

Figure 3.3 shows a trend between the X-ray luminosity and bubble mechanical luminosity, with the sense that systems with larger X-ray luminosities also have larger mechanical luminosities. This trend extends over a dynamic range of ~ 1000 in both X-ray and mechanical luminosity. Just such a trend would be expected were the

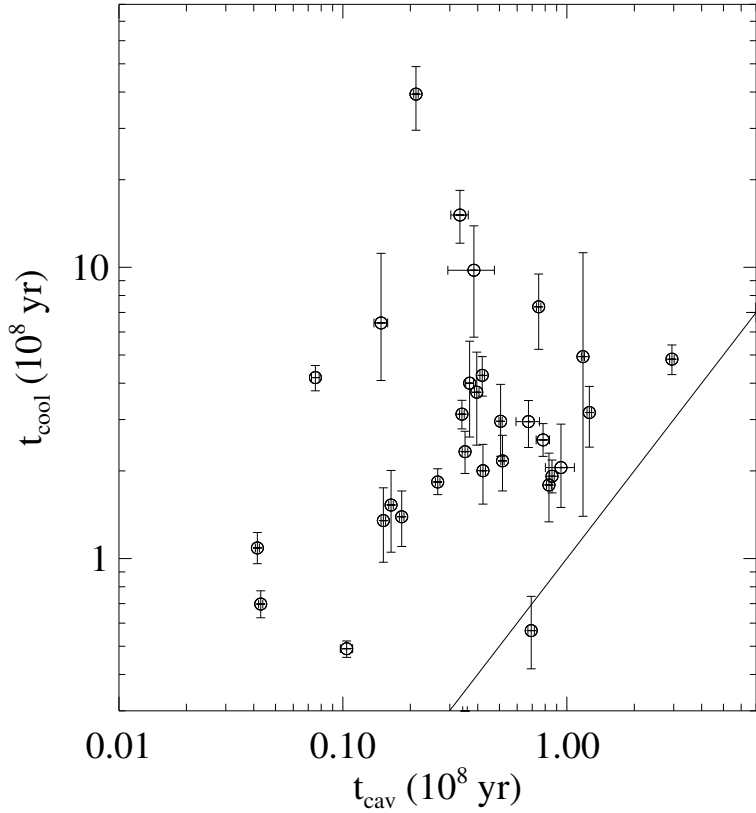


Figure 3.4: The average cavity buoyancy age versus the central cooling time. The line denotes equality between the two times.

cooling and heating of the ICM coupled in some fashion. Several studies (e.g. Rosner & Tucker, 1989; Binney & Tabor, 1995; David et al., 2001; Quilis et al., 2001; Churazov et al., 2002) have proposed that cooling is balanced by heating in a self-regulated feedback loop. The feedback loop is driven by episodic radio activity fueled by cooling and accretion onto a central black hole. The accretion energy is then returned to the ICM through an AGN outburst, including the action of the radio cavities, which temporarily arrests cooling. At later times, the center of the system settles down and the cooling flow is reestablished. During the cooling cycle, molecular gas (Edge,

2001) accumulates and star formation ensues (Johnstone et al., 1987; McNamara & O’Connell, 1989), albeit at substantially lower levels than expected in steady-cooling models (Fabian, 1994). Even if the radio bubbles are not the main source of heat, Figure 3.3 suggests that AGN feedback is intimately involved in the process that prevents a large cooling flow from forming.

The apparent correlation in Figure 3.3 should be treated with caution. As noted earlier, our sample was selected from clusters in the *Chandra* archive with fairly obvious cavities in their cores, and neglects those without obvious cavities. Other clusters are known to have substantial cooling luminosities commensurate with the observed levels of cold gas and star formation, yet contain no cavities and have low radio power. A prime example is A1068 (Wise et al., 2004; McNamara et al., 2004). Similar objects would appear in the lower right of this diagram, tending to weaken the correlation. On the other hand, it is unlikely that we would have missed objects with powerful cavities, which would lie in the upper part of this diagram. Therefore, the distribution of points may represent an upper envelope in mechanical luminosity as a function of X-ray luminosity. Such a distribution would be consistent with the feedback hypothesis, if objects like A1068 are in an extended cooling phase in which the central galaxies have experienced substantial levels of accretion in the past 100 Myr or so, when the radio source has not had a chance to create cavities capable of reducing or quenching cooling.

We have investigated the degree to which other systematic effects may lead to an unphysical luminosity-luminosity correlation. For example, [Elvis et al. \(1978\)](#) pointed out that a sample of objects with a small range of fluxes and a large range of distances will show a correlation in a luminosity-versus-luminosity plot, even if there is no intrinsic correlation in the sample. The cavities in our sample, however, have a large range of projected angular size (from $\sim 3''$ to $\sim 35''$). We believe, then, that these potential effects are unlikely to account entirely for the trends seen in Figure 3.3.

Selection bias may also contribute to the correlations. Small cavities are easily overlooked in distant objects, since cavities of a given linear size become more difficult to detect as their angular sizes decrease with increasing distance. Conversely, in very nearby objects, such as M87, we may miss larger bubbles that lie outside the detector. Furthermore, other considerations, such as the bubble position, affect the detectability ([Enßlin & Heinz, 2002](#)). The consequences of these and other effects on our selection function will be addressed in the future using a larger and better-defined sample of clusters, including a more sophisticated approach to placing limits on cavities that may exist in clusters but were missed by the observations.

3.5 Summary

We have presented an analysis of 33 systems taken from the *Chandra* archive having clear evidence for cavities in their X-ray emission. Remarkably, we find that

AGN heating, as traced by the power in X-ray cavities alone, is capable of balancing the radiative losses of the ICM in more than half of the systems in our sample. When our average heating and cooling luminosities are corrected for the fraction of all cooling flows with cavities ($\sim 70\%$, Dunn & Fabian, 2006), we find that AGN heating can on average balance cooling in all cooling flows. However, the means by which the AGN's jet energy is converted to heat in the ICM and the efficiency of this conversion are not yet clear (e.g., Reynolds et al., 2002). Lastly, our estimate of AGN heating neglects other significant sources of heat that are likely to be present in many of the systems in our sample, such as weak shocks (e.g., McNamara et al., 2005; Nulsen et al., 2005a,b; Forman et al., 2005), sound waves (e.g., Fabian et al., 2006), and thermal conduction (e.g., Voigt & Fabian, 2004). All of these heat sources may play a role in maintaining the rough balance of heating to cooling observed to exist throughout the cooling region. AGN, however, have emerged as the most important heating mechanism in cooling flows.

In addition, we have discovered a trend between the cooling X-ray luminosity and the mechanical energy of the cavities, with the sense that more luminous systems produce larger and more energetic cavities. The trend, or envelope, may have been established by a self-regulated cooling and feedback mechanism acting in many systems. The existence of such a mechanism in relatively nearby clusters, where the detailed physics can be examined, may provide significant insight on the process of galaxy formation that prevails at large redshifts (e.g., Voit et al., 2003). A similar

mechanism may regulate the growth of galaxy halos during the dissipative stages of their development ([Dubinski, 1994](#)) and may be an agent responsible for the detailed correlation between black hole mass and velocity dispersion of spheroids ([Fabian et al., 2002b](#)).

CHAPTER 4

Star Formation and the Cooling Flow

4.1 Introduction: Active Star Formation in Cooling Flows

The emerging picture of cooling flows is one in which most (but not all) of the cooling is roughly balanced by heating from AGN feedback, resulting in a moderate cooling flow (e.g., Pedlar et al., 1990; Soker et al., 2001; Binney, 2005; Soker, 2006). In this regulated-cooling scenario, net cooling from the ICM would result in condensation of gas onto the central galaxy, leading eventually to the molecular gas, star formation, and optical line emission observed in many systems (e.g., Hu et al., 1985; Johnstone et al., 1987; McNamara & O'Connell, 1989; Cardiel et al., 1998; Edge, 2001). If this scenario is correct, the star formation rates should on average be comparable to the rate of gas observed to be condensing out of the ICM. Studies of a small number of systems with reliable star formation and cooling rates have shown that the rates are converging, and in some cases are in rough agreement (e.g., McNamara, 2004; McNamara et al., 2004, 2006). The quality and quantity of data from *Chandra* and

XMM-Newton now makes it possible to construct a significantly larger sample of such systems to better understand the possible connection between star formation and net cooling in cooling flow clusters. In the first part of this chapter, we use star formation and cooling rates for a sample of 17 systems to test whether the rate of net cooling from the ICM is consistent with the rate of star formation in the central galaxy.

Additionally, it has been known for some time that indicators of star formation in the CDG, such as spatially extended, excess blue emission and optical line emission, correlate, albeit roughly, with the properties of the cooling flow (e.g., Heckman, 1981; Hu et al., 1985; McNamara & O'Connell, 1989). However, only with the advent of *Chandra* has it become possible to derive these properties on the same scale as the optical properties to determine more precisely the relationship between cooling and star formation. In the second part of this chapter, we use optical and X-ray data of similar spatial resolution for 43 systems to search for connections between the ICM properties, such as the central cooling time, and the presence of excess blue emission in the central galaxy.

4.2 Derivation of Star Formation Rates

The determination of reliable star formation rates requires sensitive photometry over a broad wavelength range to identify and isolate the star-forming population. Secure star formation rates are available in the literature for a significant number of CDGs. We have collected these rates from the literature, adjusted to our assumed

cosmology, and their sources in Table 4.1. Our sample includes rates derived from both spectroscopic and imaging studies.

Table 4.1. Star Formation and Cooling Rates.

System	Star Formation Rates			Cooling Rates		
	Continuous (ref) ^a ($M_{\odot} \text{ yr}^{-1}$)	Burst (ref) ^b ($M_{\odot} \text{ yr}^{-1}$)	Aperture (kpc)	XMM RGS (ref) ^c ($M_{\odot} \text{ yr}^{-1}$)	FUSE (ref) ^d ($M_{\odot} \text{ yr}^{-1}$)	Aperture (kpc)
A262	< 0.015 (8)	...	$r = 0.9$	< 2 (15)	...	$r = 5$
Perseus	2.3±0.2 (8)	...	$r = 1.0$...	32 ± 6 (3)	11×11
	15.5±5.2 (16)	...	$r = 18.8$
	~37 (18)	...	$r = 59$
2A 0335+096	4.2 (17)	...	$r = 16.0$	20 ± 10 (15)	...	$r = 22$
A478	10.0 (4)	...	3.1×44.6
PKS 0745-191	16.9±5.6 (16)	...	$r = 18.8$
Hydra A	≤ 0.5 (7)	~ 16 (7)	$r = 4.3$	35 ± 20 (15)	...	$r = 22$
Zw 3146	10.7 (5)	...	$5.7 \times (< 25.8)$
	< 110 (FIR)
A1068	18.1 (5)	...	3.2×15.6
	28±12 (10)	46±21 (10)	$r = 10.0$
M84	< 0.047 (FIR)
M87	< 0.02 (8)	...	$r = 0.2$	≤ 0.6 (14)	...	$r = 3.0$
	< 0.081 (FIR)	≤ 0.44 (2)	2.6×2.6
A1795	0.95±0.10 (8)	...	$r = 3.2$...	26 ± 7 (3)	36×36
	1.1 (5)	...	1.6×7.6	...	< 15 (14)	36×36
	2.1±0.9 (13)	...	19.4×19.4	< 30 (15)	...	$r = 33$
	6.3 (9)	23.2 (9)	13.3×26.7
A1835	48.9 (5)	...	5.1×8.3	< 200 (15)	...	$r = 99$
	79.0 (5)	...	5.1×8.3
	79.5 (5)	...	$5.1 \times (< 23.7)$
	140±40 (11)	...	$r = 30$
A2029	< 0.15 (8)	...	$r = 3.9$...	< 27 (3)	44×44
A2052	0.08±0.02 (8)	...	$r = 1.8$	< 10 (15)	...	$r = 17$
	0.51 (5)	...	0.9 × 6.8

Table 4.1 (continued)

System	Star Formation Rates				Cooling Rates		
	Continuous (ref) ^a ($M_{\odot} \text{ yr}^{-1}$)	Burst (ref) ^b ($M_{\odot} \text{ yr}^{-1}$)	Aperture (kpc)	XMM RGS (ref) ^c ($M_{\odot} \text{ yr}^{-1}$)	FUSE (ref) ^d ($M_{\odot} \text{ yr}^{-1}$)	Aperture (kpc)	
MKW 3S	0.31±0.10 (1)	...	$r = 2.1$
A2199	< 0.03 (8)	...	$r = 2.3$	< 10 (15)	$r = 11$
	0.10±0.03 (8)	...	$r = 1.6$
	0.10 (5)	...	0.8×7.3
A2597	2.3±1.3 (13)	...	16.0×16.0	$\lesssim 50$ (12)	$r = 190$
	6.4 (9)	22.3 (9)	24.2×24.2	...	22 (14)	48×48	
A4059	< 10 (15)	$r = 147$

^aContinuous star formation rate. References are in parentheses.^bStar formation rate for a burst of star formation calculated as the mass of the burst divided by its age. References are in parentheses.^cCooling rates derived from XMM-Newton RGS spectra. References are in parentheses.^dCooling rates derived from FUSE spectra. References are in parentheses.

References. — (1) Blanton et al. (2003); (2) Bregman et al. (2005); (3) Bregman et al. (2006); (4) Cardiel et al. (1998); (5) Crawford et al. (1999); (6) Lecavelier des Etangs et al. (2004); (7) McNamara (1995); (8) McNamara & O'Connell (1989); (9) McNamara & O'Connell (1993); (10) McNamara et al. (2004); (11) McNamara et al. (2006); (12) Morris & Fabian (2005); (13) O'Dea et al. (2004); (14) Oegerle et al. (2001); (15) Peterson et al. (2003); (16) Romanishin (1987); (17) Romanishin & Hintzen (1988); (18) Smith et al. (1992).

Typically, in deriving star formation rates, one first finds the luminosity of the star-forming population. From broadband images, this luminosity may be found by modeling and subtracting a smooth background galaxy (see e.g., McNamara et al., 2004). Any extended excess emission is then assumed to be due to active star formation, and the resulting colors may then be compared to stellar population models to constrain its age and mass-to-light ratio (however, the age and mass-to-light ratio cannot be constrained unambiguously using colors alone). For spectra, a similar process is used whereby a spectrum of the background galaxy is subtracted (or included as a component in the models), and the remaining spectral features are then fit with stellar population models (see e.g., Crawford et al., 1999). The models constrain the mass-to-light ratio and age of the star forming population, which may be used, together with its luminosity, to calculate the mean star formation rate. In both cases, the derived quantities are valid only in the aperture used. Consequently, there are three main sources of inhomogeneity in the star formation rates in our sample: differences and discrepancies in the model parameters (e.g., assumed ages), differences in the apertures within which the star formation is measured, and uncertainties due to dust extinction and reddening.

There are two principal parameters that go into the stellar population synthesis models: the slope of the initial mass function (IMF) and the star formation history. Changes in either of these parameters can result in typical deviations of factors of \sim 5-10 in the derived star formation rates. For the systems in our sample that have

star formation rates available, we list in Table 4.1 rates derived assuming continuous star formation for $\sim 10^9$ yr and, when available, for shorter duration bursts. There is little variation across our sample in IMF slope, since most studies assume a Salpeter IMF. This assumption appears to be valid in cooling flows (e.g., McNamara et al., 2006).

A significant difference between the studies we considered is the choice of aperture size. Observations made in spectroscopic slits have the weakness that the star forming region may not fall entirely within the slit, resulting in an underestimate of the total star formation rate. Table 4.1 gives the aperture used in each study. In our sample, aperture effects could lead to an underestimate of the total star formation rate by as much as a factor of ~ 10 if the star formation is uniformly distributed across the galaxy. However, imaging studies of CDGs (e.g., McNamara & O'Connell, 1992; Cardiel et al., 1998) show that star formation is centrally concentrated in most systems, reducing somewhat the likely magnitude of this effect. A comparison of objects in our sample with star formation rates derived in both ways shows that spectroscopic rates are typically lower than imaging-derived rates by factors of several. Therefore, although spectroscopic estimates should be treated as lower limits to the total star formation rates, they are unlikely to be more than an order of magnitude lower than the total rates.

In addition to observational and modeling inhomogeneities across our sample, a number of uncertainties exist in any derivation of the star formation rate. Principal

among these are the effects of extinction and reddening due to dust. These effects are difficult to quantify without high resolution imaging which is not generally available. But comparisons between the U -band rates, which are subject to strong extinction, and far IR rates, which are not, agree to within a factor of two (e.g., McNamara et al., 2004, 2006). Of the objects in our sample, A2052 (Blanton et al., 2003), A1068 (McNamara et al., 2004), 2A 0335+096 (Romanishin & Hintzen, 1988), A1795 and A2597 (O'Dea et al., 2004), and those systems studied by Crawford et al. (1999) have published rates that have been corrected for the presence of dust. The intrinsic color excess for systems similar to those in our sample is typically $E(B - V) \sim 0.3$ (Crawford et al., 1999).

Lastly, errors in mass-to-light ratio and age, while leading to errors in accreted mass, generally result in robust star formation rates due to the compensating effect that older populations have higher mass-to-light ratios. Therefore, errors resulting from an overestimated age will be partly compensated by an overestimated population mass, reducing the error in the resulting star formation rate.

A number of objects in our sample have no published optical star formation rates, or their rates were measured only in small apertures. For these objects, when possible, we have inferred the star formation rate from the far infrared (FIR) *IRAS* 60 μm flux derived with the Infrared Processing and Analysis Center's SCANPI tool.¹ We used the following relation of Kennicutt (1998) to convert the total FIR luminosity to a

¹See <http://irsa.ipac.caltech.edu/Missions/iras.html>

star formation rate:

$$\frac{SFR}{M_{\odot} \text{ yr}^{-1}} \lesssim 4.5 \times \left(\frac{L_{\text{FIR}}}{10^{44} \text{ erg s}^{-1}} \right), \quad (4.1)$$

where $L_{\text{FIR}} \sim 1.7 L_{60 \mu\text{m}}$ (Rowan-Robinson et al., 1997), and we have assumed that all the UV photons emitted by young stars are absorbed and re-radiated by dust in the FIR. Three objects in our sample have reliable 60 μm fluxes: Zw 3146, M87, and M84; for these objects we derived upper limits to the star formation rates (see Table 4.1).

4.3 Comparing Star Formation and Cooling Rates

We wish to test the hypothesis that star formation is fueled by gas condensing out of the ICM. If true, and cooling and star formation vary slowly with time, their rates should be comparable to each other. To make this comparison, we plot the net cooling (condensation) rate (derived as described in Section 3.3) against the star formation rate in Figure 4.1. Symbols denote the various types of data used to derive the star formation rate (see Section 4.2). The cooling rates include estimates inferred from XMM-Newton X-ray spectra and from FUSE ultraviolet spectra (see Section 3.3.2), and from our *Chandra* data (see Section 3.3.1). In almost all cases, the X-ray-derived cooling rates should be considered upper limits, since indisputable evidence of cooling below ~ 1 keV has yet to be found in the X-ray emission from cooling flow clusters.

The apparent trend should be interpreted cautiously in this context (see caveats in Section 3.3.2).

Figure 4.1 shows the condensation and star formation rates for all systems in our sample are consistent with the hypothesis that star formation is fueled by gas condensing out of the ICM. The average ratio of condensation to star formation rate for those rates derived in similar apertures is $\dot{M}_{\text{cool}}/\text{SFR} \sim 4$, using XMM-*Newton* and FUSE rates (the ratio does not change significantly if *Chandra* rates are considered). This value is similar to that found by Hicks & Mushotzky (2005) in a study of star formation and cooling using XMM-*Newton* UV monitor data.

Figure 4.1 shows that the rates of star formation and cooling have converged greatly and are in rough agreement in several systems. The classical cooling flow problem, in which the X-ray-derived cooling rates were factors of $10 - 100$ in excess of the star formation rates in most systems, has largely disappeared. While the average discrepancy of four to one is still large, it is of the order of the uncertainty in the rates. Factors that may contribute to scatter in the rates are time-dependent effects such as radio-triggered star formation (McNamara & O’Connell, 1993) and the time lag required for gas at $\sim 10^7$ K to cool and form stars.

Lastly, it is clear that if star formation is being fueled by the ICM, firm detections of cooling out of the X-ray band should be within reach of present and future X-ray observatories for those objects with large star formation rates (McNamara et al., 2006). Even with present-day instruments, the upper limits on cooling derived to date

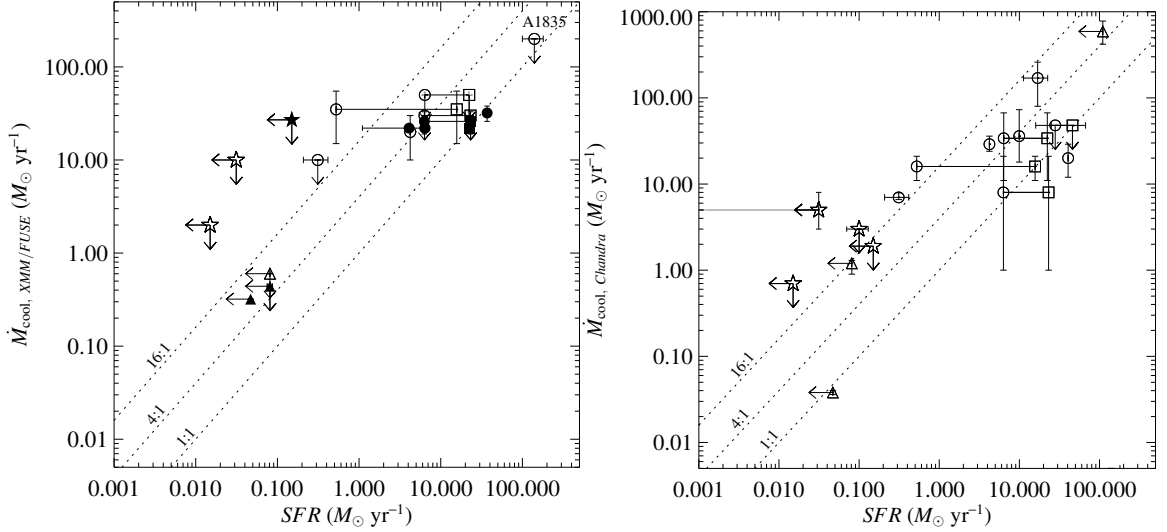


Figure 4.1: *Left:* Net cooling rate from *XMM-Newton* (*empty symbols*) and *FUSE* data (*filled symbols*) versus the star formation rate. *Right:* Net cooling rate from our *Chandra* X-ray analysis versus the star formation rate. Circles denote continuous SFRs measured from broadband images, stars denote continuous SFRs measured from spectra taken in slits, and triangles denote continuous FIR SFRs. When more than one rate is available, we plot the largest rate. If an object has both broadband and spectral rates, we plot only the broadband rate. Squares denote rates for a burst of star formation and are joined to symbols denoting continuous rates for the same object by horizontal lines. The diagonal lines denote different ratios of the cooling to star formation rate.

are very close to the inferred total star formation rates for a number of objects (e.g., A1835). If this star formation scenario is to survive, future deep X-ray observations of these objects (with Constellation-X, for example) should detect this cooling gas.

4.4 Comparing CDG Colors and Central ICM Properties

We now turn to a more general test of the moderate cooling-flow paradigm: whether the colors of the CDG are related to the properties of the cooling flow on similar spatial scales. In the following sections, we describe the analysis of the optical data described in Section 2.3. These data are used to search for spatially extended blue color excess, a signature of star formation, in the central galaxy. As a reminder, we note that these data were obtained to attempt to investigate the connection between star formation, cooling, and feedback in cooling-flow clusters. To this end, we observed a sample of systems with a broad range of central cooling time and entropy, both with and without evidence for feedback.

4.4.1 Excess Blue Emission as a Signature of Star Formation

The primary signatures of star formation are due to the presence of hot, massive stars in the star-forming population. This population is mixed with the generally old stellar population of the underlying CDG, as well as with cold gas and dust. These massive stars emit most of their energy in the ultraviolet and blue parts of the spectrum, unlike the less massive but much longer-lived stars that account for most of the CDG’s emission at longer wavelengths. The ultraviolet emission in turn can ionize nearby cool gas, resulting in optical line emission such as H α emission. Additionally,

the energetic photons from the massive stars heat surrounding dust, which re-emits the light in the far infrared through black-body radiation. In this study, we use the excess blue emission (above that expected from the old background population) as an indicator of recent star formation.

We use broadband imaging at short and long wavelengths to search for the excess blue emission in the cores of the CDGs. By comparing the short-wavelength surface-brightness profile, which is sensitive to young hot stars, with the long-wavelength profile, which traces the old background population, we can detect the presence of star formation. Elliptical galaxies generally show no signs of recent star formation, and have color profiles that become bluer with increasing radius (e.g., [Vader et al., 1988](#); [Franx et al., 1989](#); [Peletier et al., 1990](#); [Goudfrooij et al., 1994](#)). This effect is thought to be generally due to a decreasing stellar metalicity with increasing radius (e.g., [Carollo et al., 1993](#); [Kobayashi & Arimoto, 1999](#); [Tamura & Ohta, 2000](#); [Ferreras et al., 2005](#)). Therefore, a color profile that becomes increasingly blue towards the center is unusual (i.e. the CDG has excess blue emission), and is indicative of recent star formation in that region. We use this property to identify star formation in our sample.

The excess blue emission, while generally indicative of star formation, can be the result of other sources, such as the scattered light from an AGN or a low-metalicity stellar population. However, because AGNs are point sources, their emission should not be spatially extended on scales of tens of kpc, as the excess blue emission is often

observed to be in CDGs. Scattered light can make the AGN emission appear more extended, but studies of the nearby cooling flows A1795 and A2597 have ruled out significant polarization in the excess blue light (e.g., McNamara et al., 1996a, 1999). As to metalicity effects, most modeling of spectra and broadband colors of CDGs has found that systems with large color excesses are better modeled by emission from massive O and B stars, rather than old, low-metalicity stellar populations (e.g., Allen, 1995; Cardiel et al., 1995; Smith et al., 1997; Cardiel et al., 1998; Crawford et al., 1999). Additionally, Hubble Space Telescope studies of two CDGs with prominent blue excesses, A1795 and A2597, have resolved the blue emission into knots and demonstrated that it is most likely due to recent star formation (Koekemoer et al., 1999, 2002; O'Dea et al., 2004).

4.4.2 Analysis of Imaging Data

When more than one observation was made of a given object (e.g., at both MDM and KPNO), the data with the higher signal-to-noise were analyzed. We identified the CDG as the most extended galaxy within the field, which generally lies near the X-ray core. However, when the cluster contains more than one very large galaxy or if it is unclear which is the dominant galaxy, we chose as the CDG the galaxy with the largest integrated K -band magnitude from the 2MASS catalog. Below we note any unusual characteristics of the CDG or image.

A85: The CDG has extended optical line emission ([Hu et al., 1985; Fisher et al., 1995](#)).

3C 28: An excess of UV flux has been detected in the CDG by [Wills et al. \(2002\)](#) and was ascribed by them to active star formation.

A262: The CDG has a large, central dust lane and a bright star nearby which were masked.

Perseus: The Perseus CDG (NGC 1275) is well known for its blue, emission-line filaments, dust lanes, and the foreground high-velocity system, all of which were masked before analysis. Significant star formation was detected by [McNamara & O'Connell \(1989\); Romanishin \(1987\); Smith et al. \(1992\)](#).

2A 0335+096: There is a nearby bright star in the image that results in large areas of the galaxy being masked. Significant star formation was detected by [Romanishin & Hintzen \(1988\)](#).

A478: [Cardiel et al. \(1998\)](#) found spectral evidence for significant star formation in the CDG.

A520: The cluster appears to have no well-defined optical core ([Dahle et al., 2002](#)), but instead has several concentrations of galaxies, none of which coincides with the X-ray core. [Crawford et al. \(1999\)](#) note that there are three dominant galaxies and chose the SW one as the CDG, as did we.

M87: The optical jet and central region, associated with the AGN, were masked before analysis.

HCG 62: This compact group has a large, nearby companion galaxy, which was masked before analysis.

A1795: The CDG is well known to harbor a tail of blue emission that is thought to be due to star formation triggered by compression of the gas by the radio source ([McNamara et al., 1996a,b](#); [Pinkney et al., 1996](#); [O'Dea et al., 2004](#)). The R - and I -band images were affected by scattered light, which was masked as thoroughly as possible.

A1991: As with A1795, the long-wavelength images were affected by scattered light, requiring masking, and the seeing was poor. [McNamara & O'Connell \(1989\)](#) report spectral evidence for a small SFR, and [McNamara & O'Connell \(1992\)](#) report a positive $U - I$ color gradient in the core.

RXC J1504.1-0248: The U -band image shows an elongated blue region in the core, extending 6 arcsec in length.

A2065: This cluster has two dominant galaxies. We have analyzed the southern galaxy, which appears to be associated with the X-ray core ([Chatzikos et al., 2006](#)).

RX J1532.5+3021: The CDG is known to be very blue (Dahle et al., 2002). The $U - I$ colormap shows a very blue region offset slightly to the south of the core. extending 4-8 arcsec in radius.

Hercules A: The CDG has extended optical line emission (Tadhunter et al., 1993). The CDG core is the southeastern of the two surface-brightness peaks.

A2244: A nearby bright star required large areas of masking.

RX J1720.2+2637: The CDG has a blue central region some 13 arcsec in radius.

MACS J1720.2+3536: The $U - I$ colormap shows blue emission extending to a radius of 2.5 arcsec.

A2390: The U -band image shows a very blue, elongated region in the core, extending SE to NW some 4-5 arcsec in length.

A2597: The CDG possesses knots of star formation (McNamara & O'Connell, 1992; Koekemoer et al., 2002; O'Dea et al., 2004).

Radial Profiles

The master frames, created by stacking the individual frames for each object (see Section 2.3), were first registered to a common coordinate grid using *wregister* in IRAF. Next, the master frames were PSF-matched using the *psfmatch* task to the lowest-resolution frame of the set (typically the U -band frame). This step is

necessary before spatial comparisons between frames taken in different bands can be made. However, since the bands are fairly broad ($FWHM \sim 1500 \text{ \AA}$) and the stars used for the matching may have different colors than the CDG, some effect due to PSF mismatches will remain in the data.

Surface brightness profiles were constructed from the PSF-matched, registered master frames using the *ellipse* task in IRAF. This task works by fitting ellipses to isophotes of the surface brightness distribution of a galaxy and calculating the mean surface brightness along the ellipse (see [Jedrzejewski, 1987](#)). Clipping routines are used to reject stars, superimposed galaxies, or other source of contamination. Additionally, such objects as were visible were masked out by eye before fitting. The ellipticities and position angles were allowed to vary from ellipse to ellipse to reflect changes in the underlying galaxy. Typically, the surface brightness distributions of CDGs become more elliptical at larger radii (e.g., [Patel et al., 2006](#)). The ellipse centroids were not allowed to vary, to make comparisons between profiles in different bands possible. The centroids were determined from the long-wavelength images (R or I), which are generally smooth and relaxed (reflecting the old stellar populations of the galaxy). Centroid positions were calculated using *imexamine* in IRAF, which finds the centroid using Gaussian fits to the radial surface brightness profile.

The ellipse centers, ellipticities, and position angles were fixed to those resulting from a fit to the R - or I -band image, whichever was of higher signal-to-noise, to make it possible to compare profiles in different bands. We note that fixing the U -

band ellipse properties to those of a longer-wavelength band will tend to reduce the U -band surface brightness along the ellipse if the U -band emission has significantly different preferred ellipticities or position angles. An example of such a case is A2390, which has a bar of very blue emission near its center that is clearly different in shape from the I -band emission in the same region (see Appendix A). The net effect of our procedure is to dilute somewhat the signatures of star formation in our profiles; however, we estimate that the effect is generally small.

The resulting color profiles for the optical sample are shown in Figures 4.2 and 4.3.

Errors in Intensities

The total error on each point of the surface brightness profile is the sum of the errors due to the random, statistical fluctuations along each ellipse and the statistical and systematic uncertainties associated with the sky subtraction. The error returned by *ellipse* for the isophotal intensities is the standard deviation of the mean of the intensities along the ellipse ($\sigma_I = \sigma_I/\sqrt{N}$, where N is the number of pixels along the ellipse). The errors in the sky determination may be divided into statistical (i.e. those errors that limit the sky accuracy, even if all sky boxes return the same mode) and the systematic (i.e. those errors that are due to using contaminated regions or are due to gradients in the image):

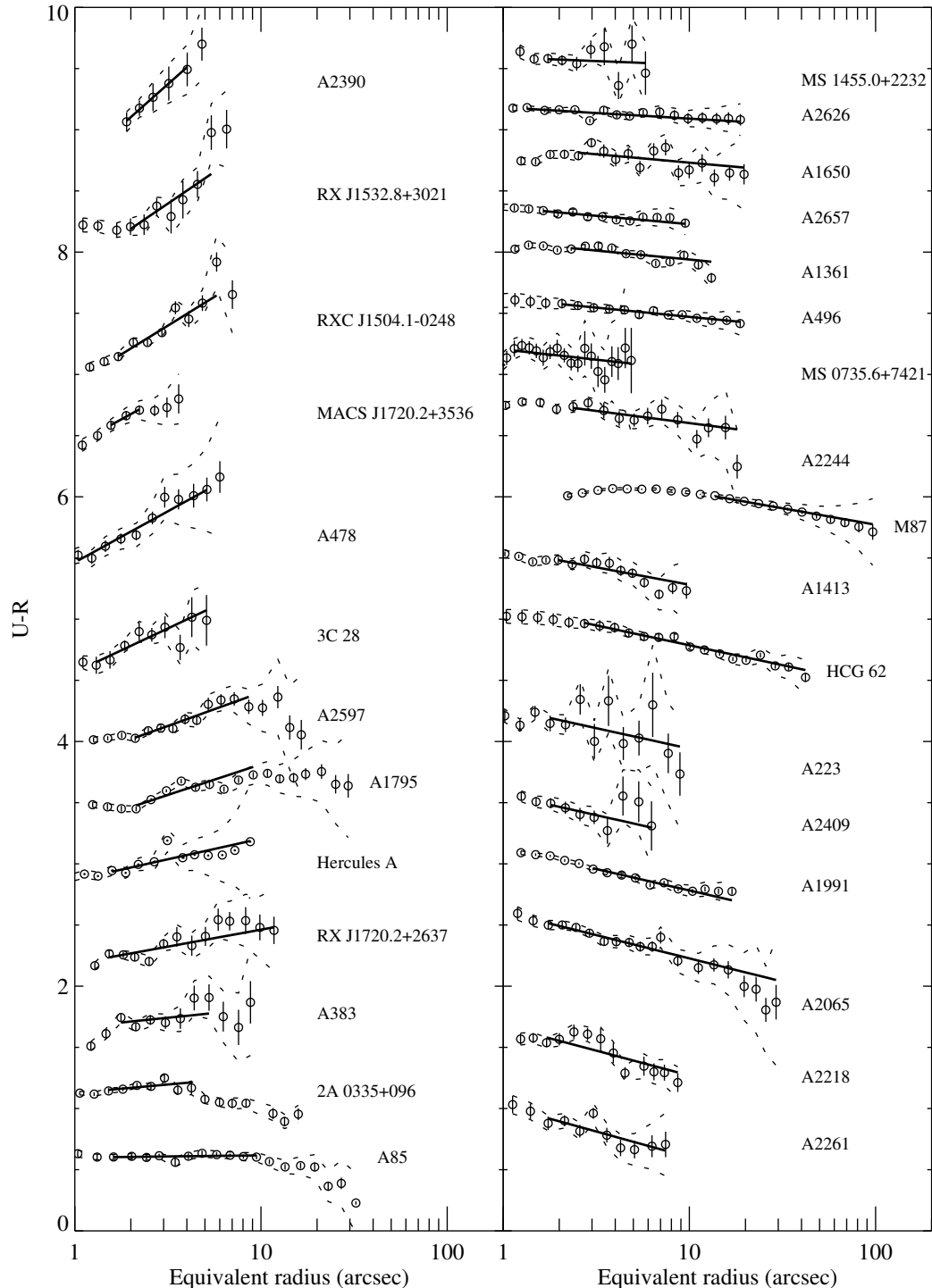


Figure 4.2: $U - R$ color versus the equivalent radius ($r = [ab]^{1/2}$, where a and b are the semiaxes) for the optical sample, ordered by decreasing gradient. The colors for each object have been shifted by arbitrary values. The error bars shown for each point are the statistical errors; the dashed lines show the total (statistical plus systematical) errors. The best-fit gradients (see Section 4.4.2) are overplotted as solid lines between the inner and outer radii used in the fit.

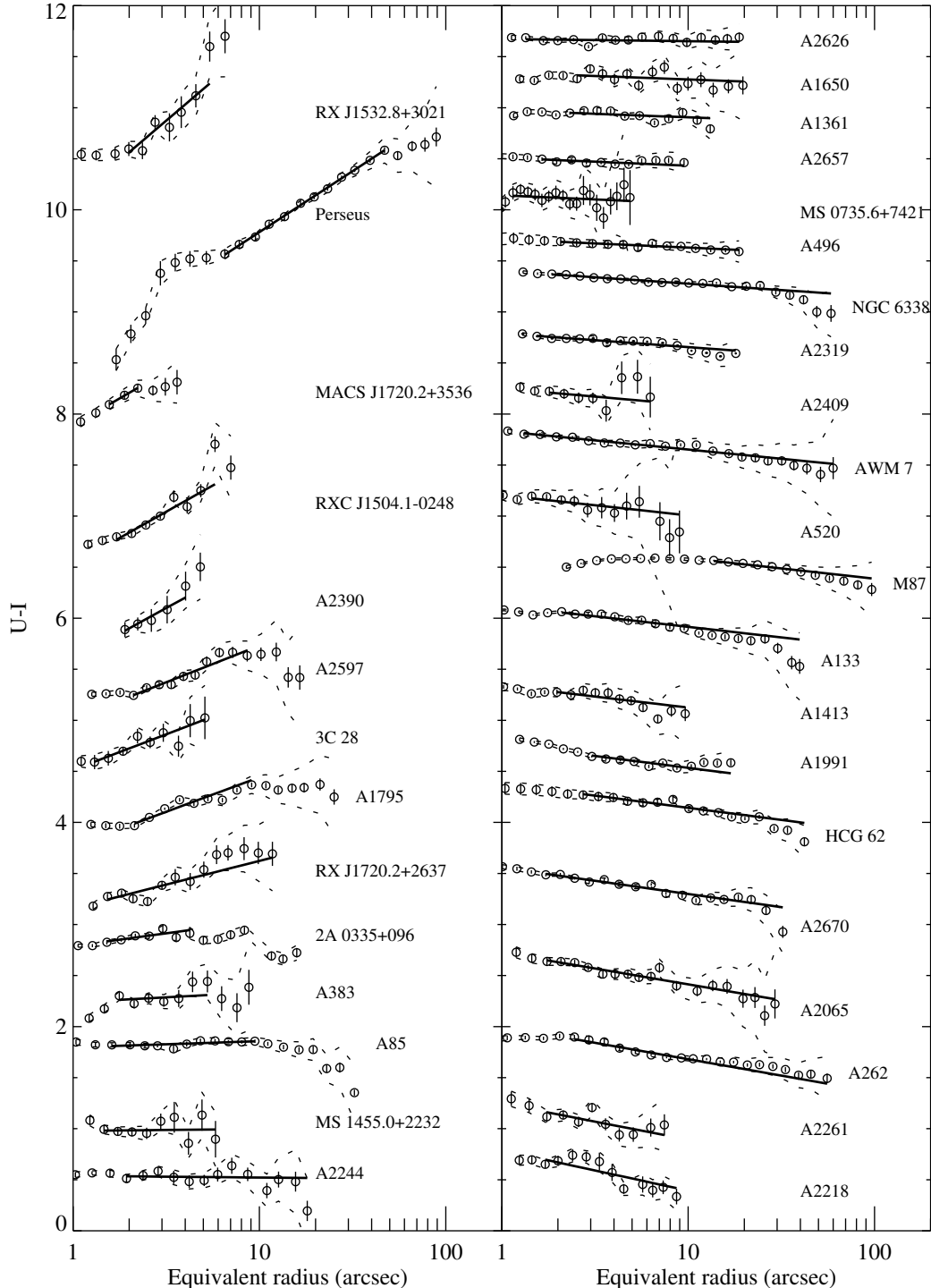


Figure 4.3: $U - I$ color versus the equivalent radius ($r = [ab]^{1/2}$, where a and b are the semiaxes) for the optical sample, ordered by decreasing gradient. The colors for each object have been shifted by arbitrary values. Lines and errors are the same as in Figure 4.2.

Statistical: These errors are estimated by the standard deviation of the mean of the sky values in each sky box (σ_i). The resulting best sky for all the boxes is the weighted mean of the modes ($sky_{\text{best}} = \sum w_i x_i / \sum w_i$, where $w_i = 1/\sigma_i^2$ are the weights), and the error is $\sigma_{sky_{\text{best}}} = (\sum w_i)^{-1/2}$.

Systematic: These errors are estimated from the maximum difference between modes in any two sky boxes (Δsky , see Section 2.3.3).

The resulting total statistical errors in sky-subtracted intensity per pixel are then given by $\delta_I = (\sigma_I^2 + \sigma_{sky}^2)^{1/2}$. These errors are generally dominated by variations in intensity along the isophote, not by the sky errors. The resulting total (statistical plus systematic) errors are then $\sigma_{\text{tot+sys}} = [\delta_I^2 + (\Delta sky/2)^2]^{1/2}$.

Color Gradients and Δ Colors

Color gradients were derived for the $U - I$ and $U - R$ color profiles using a least-squares fitting routine in the MPFIT package written by Craig Markwardt.² The color gradient is defined as the change color (in magnitudes) over the corresponding change in $\log(r)$ (in dex); e.g., for $U - I$:

$$G(U - I) = \frac{d(U - I)}{d \log(r)}. \quad (4.2)$$

The following function was fit to the data in color- $\log(r)$ space:

$$U - I = G(U - I) \log(r) + b, \quad (4.3)$$

²See <http://cow.physics.wisc.edu/~craigm/idl/fitting.html>.

where $G(U - I)$ is the color gradient and b is the intercept. The data were weighted by their total (systematic plus statistical) error, and errors on the gradient were returned by the covariance matrix of the best fit. To eliminate possible effects from the PSF on the fitted gradient, the fits were restricted to radii greater than twice the radius of the FWHM of the PSF. The outer radius used in the fit was set differently for objects with blue cores and for those without. For blue objects, the outer radius was set to the radius at which the profile turns over (where the gradient becomes negative, the approximate point at which star formation ends), so that the resulting gradient would trace the star-forming region only. The edge of the blue emission was determined by examining the $U - I$ or $U - R$ colormaps of the galaxy, made by dividing the U -band image by either the R - or I -band image. For red objects, the outer radius was set to the radius at which the total errors reach 0.5 mag to avoid regions where sky-subtraction errors significantly affect the profile (however, since the data were weighted by their errors, this choice has little effect on the measured gradients). See Figures 4.2 and 4.3 for plots of the color profiles with the best-fit gradients overlaid. Table 4.2 lists the color gradients and radial range over which they were derived.

The $U - R$ and $U - I$ color gradients are very similar, with the $U - I$ color gradients being on average slightly more positive (due to a lower contribution from the star formation to the flux in the I -band). To illustrate this, we plot in Figure 4.4

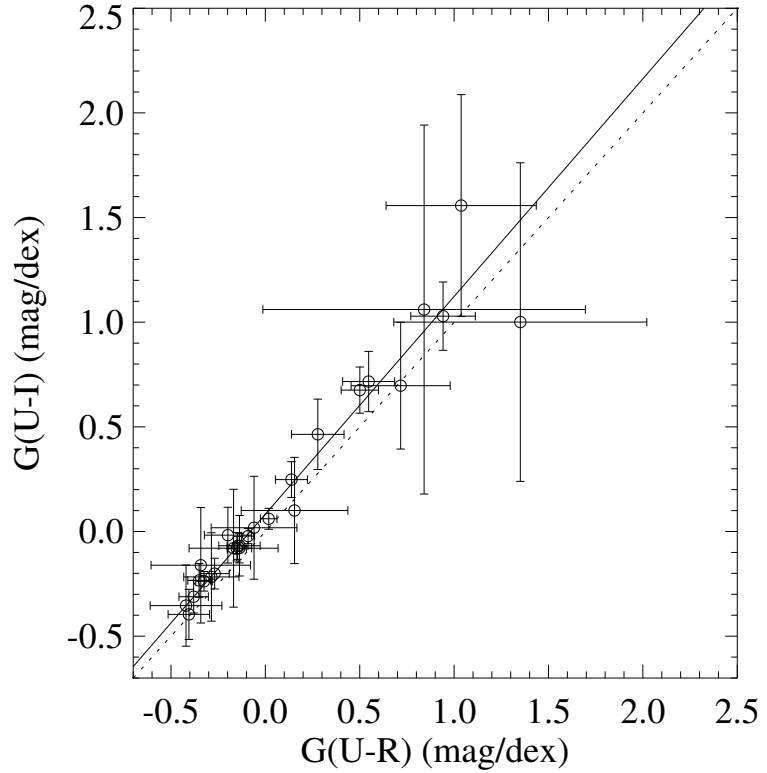


Figure 4.4: The $U - I$ color gradient versus the $U - R$ color gradient. The dashed line shows equality between the two gradients, while the solid line shows the best-fit straight line.

the two gradients against one another. The best-fit straight line gives:

$$G(U - I) = (0.09 \pm 0.03) + (1.05 \pm 0.10)G(U - R). \quad (4.4)$$

The $U - I$ color gradients are therefore consistent with a simple offset from the $U - R$ color gradients.

The gradients discussed above do not by themselves give an indication of the radial extent of the star formation. For two objects with the same gradient, one may have star formation over a much larger physical radius. Therefore, it is useful to derive the change in color between two physical radii. Objects with star-forming regions that

are physically smaller will tend to have smaller color changes than those objects with more extended star formation. To derive the color changes, denoted $\Delta(U - R)$ and $\Delta(U - I)$, we use simple linear interpolation to estimate the colors at 5, 10, and 20 kpc. The $\Delta(U - R)$ color changes are then:

$$\Delta(U - R) = (U - R)_{\text{outer}} - (U - R)_{\text{inner}} \quad (4.5)$$

Table 4.2 lists the Δ colors for the optical sample.

Table 4.2. CDG Color Gradients and Δ Colors.

System	Color Gradients			Δ Colors		
	$\frac{d(U-R)}{d\log(r)}$ (mag dex $^{-1}$)	$\frac{d(U-I)}{d\log(r)}$ (mag dex $^{-1}$)	Range (arcsec)	$\Delta(U-R)$ (mag)	$\Delta(U-I)$ (mag)	Range (kpc)
A85	0.02 ± 0.04	0.06 ± 0.05	1.6-9.5	-0.03 ± 0.05	0.00 ± 0.05	5-10
3C 28	0.72 ± 0.26	0.70 ± 0.30	1.3-5.1	-0.10 ± 0.10	-0.08 ± 0.10	5-20
A133	...	-0.21 ± 0.04	1.8-39.6	0.26 ± 0.14	0.24 ± 0.15	5-10
A223	-0.34 ± 0.31	...	1.5-8.9	...	-0.09 ± 0.05	5-10
A262	...	-0.32 ± 0.03	2.0-176.4	-0.14 ± 0.18	-0.19 ± 0.10	5-20
A383	0.15 ± 0.28	0.10 ± 0.25	1.8-5.3	-0.06 ± 0.39	-0.06 ± 0.10	5-10
AWM 7	...	-0.18 ± 0.03	1.1-84.8	...	-0.19 ± 0.25	5-20
Perseus	...	1.19 ± 0.07	6.5-47.0
2A 0335+096	0.14 ± 0.08	0.25 ± 0.09	1.5-4.2	-0.12 ± 0.08	-0.09 ± 0.18	5-10
A478	0.84 ± 0.25	...	1.0-5.1	0.16 ± 0.53	-0.17 ± 0.45	5-20
A496	-0.15 ± 0.05	-0.08 ± 0.06	1.7-18.7	-0.05 ± 0.08	-0.04 ± 0.09	5-10
A520	...	-0.20 ± 0.28	1.2-9.0	-0.08 ± 0.22	-0.11 ± 0.24	5-20
MS 0735.6+7421	-0.17 ± 0.24	-0.08 ± 0.28	1.0-4.9	-0.03 ± 0.24	-0.13 ± 0.16	5-10
PKS 0745-191 ^a	...	1.496 ± 0.13	2.0-6.0	...	-0.13 ± 0.48	5-20
A1361	-0.15 ± 0.06	-0.07 ± 0.06	2.0-13.1	-0.04 ± 0.03	-0.03 ± 0.03	5-10
A1413	-0.29 ± 0.15	-0.22 ± 0.21	1.7-9.6	-0.06 ± 0.06	-0.00 ± 0.07	5-20
M87	-0.27 ± 0.08	-0.20 ± 0.07	11.5-96.6	-0.05 ± 0.09	-0.03 ± 0.10	5-10

Table 4.2 (continued)

System	Color Gradients			Δ Colors		
	$\frac{d(U-R)}{d\log(r)}$ (mag dex ⁻¹)	$\frac{d(U-I)}{d\log(r)}$ (mag dex ⁻¹)	Range (arcsec)	$\Delta(U-R)$ (mag)	$\Delta(U-I)$ (mag)	Range (kpc)
HCG 62	-0.33 ± 0.04	-0.24 ± 0.05	2.3-42.1	-0.07 ± 0.11	-0.14 ± 0.13	5-10
A1650	-0.14 ± 0.11	-0.07 ± 0.14	2.1-19.7	-0.05 ± 0.11	-0.02 ± 0.11	5-10
Coma	-0.14 ± 0.02	...	1.7-94.4	-0.04 ± 0.08	...	5-10
A1795	0.50 ± 0.10	0.68 ± 0.11	2.1-9.1	0.05 ± 0.08	0.14 ± 0.08	5-10
A1991	-0.35 ± 0.06	-0.23 ± 0.08	2.6-16.9	-0.11 ± 0.05	-0.08 ± 0.06	5-10
MS 1455.0+2232	-0.06 ± 0.23	0.02 ± 0.25	1.5-5.8	5-20
RXC J1504.1-0248	0.94 ± 0.17	1.03 ± 0.16	1.7-5.8	5-10
A2029 ^a	...	-0.269 ± 0.014	3.0-10.0
A2052 ^a	...	-0.069 ± 0.021	5.0-35.0
A2065	-0.38 ± 0.08	-0.31 ± 0.08	1.4-29.2	0.01 ± 0.10	0.04 ± 0.10	5-10
RX J1532.8+3021	1.04 ± 0.40	1.56 ± 0.53	2.0-5.4	-0.20 ± 0.18	-0.11 ± 0.18	5-20
A2218	-0.41 ± 0.11	-0.40 ± 0.12	1.4-8.7	0.02 ± 0.10	0.02 ± 0.10	5-10
Hercules A	0.34 ± 0.25	...	1.6-8.8	0.13 ± 0.11	...	5-10
A2244	-0.20 ± 0.12	-0.02 ± 0.13	1.9-18.1	-0.12 ± 0.09	-0.05 ± 0.10	5-10
NGC 6338	...	-0.12 ± 0.01	1.6-102.2	-0.28 ± 0.17	-0.17 ± 0.17	5-20
RX J1720.2+2637	0.28 ± 0.14	0.46 ± 0.17	1.5-11.7	0.14 ± 0.10	0.16 ± 0.11	5-10
MACS J1720.2+3536	0.84 ± 0.85	1.06 ± 0.88	1.6-2.2	0.27 ± 0.18	0.41 ± 0.19	5-20
			

Table 4.2 (continued)

System	Color Gradients			Δ Colors		
	$\frac{d(U-R)}{d\log(r)}$ (mag dex $^{-1}$)	$\frac{d(U-I)}{d\log(r)}$ (mag dex $^{-1}$)	Range (arcsec)	$\Delta(U-R)$ (mag)	$\Delta(U-I)$ (mag)	Range (kpc)
A2261	-0.42 ± 0.19	-0.35 ± 0.19	1.4-7.4	-0.10 ± 0.10	-0.10 ± 0.10	5-10
A2319	...	-0.13 ± 0.05	1.3-18.0	...	-0.26 ± 0.17	5-20
A2390	1.35 ± 0.67	1.00 ± 0.76	1.9-4.0	0.77 ± 0.17	-0.06 ± 0.07	5-10
A2409	-0.34 ± 0.26	-0.16 ± 0.28	1.5-6.3	1.41 ± 0.54	-0.14 ± 0.13	5-20
A2597	0.55 ± 0.14	0.72 ± 0.14	2.1-8.6	-0.12 ± 0.17	0.23 ± 0.10	5-10
A2626	-0.09 ± 0.03	-0.02 ± 0.04	1.1-18.8	0.23 ± 0.32	0.31 ± 0.10	5-10
A2657	-0.14 ± 0.06	-0.08 ± 0.07	1.4-9.5	-0.01 ± 0.07	-0.01 ± 0.07	5-10
A2670	...	-0.26 ± 0.03	1.4-32.2	...	-0.08 ± 0.03	5-10
			-0.18 ± 0.06	5-20

^aGradient taken from McNamara & O'Connell (1992)

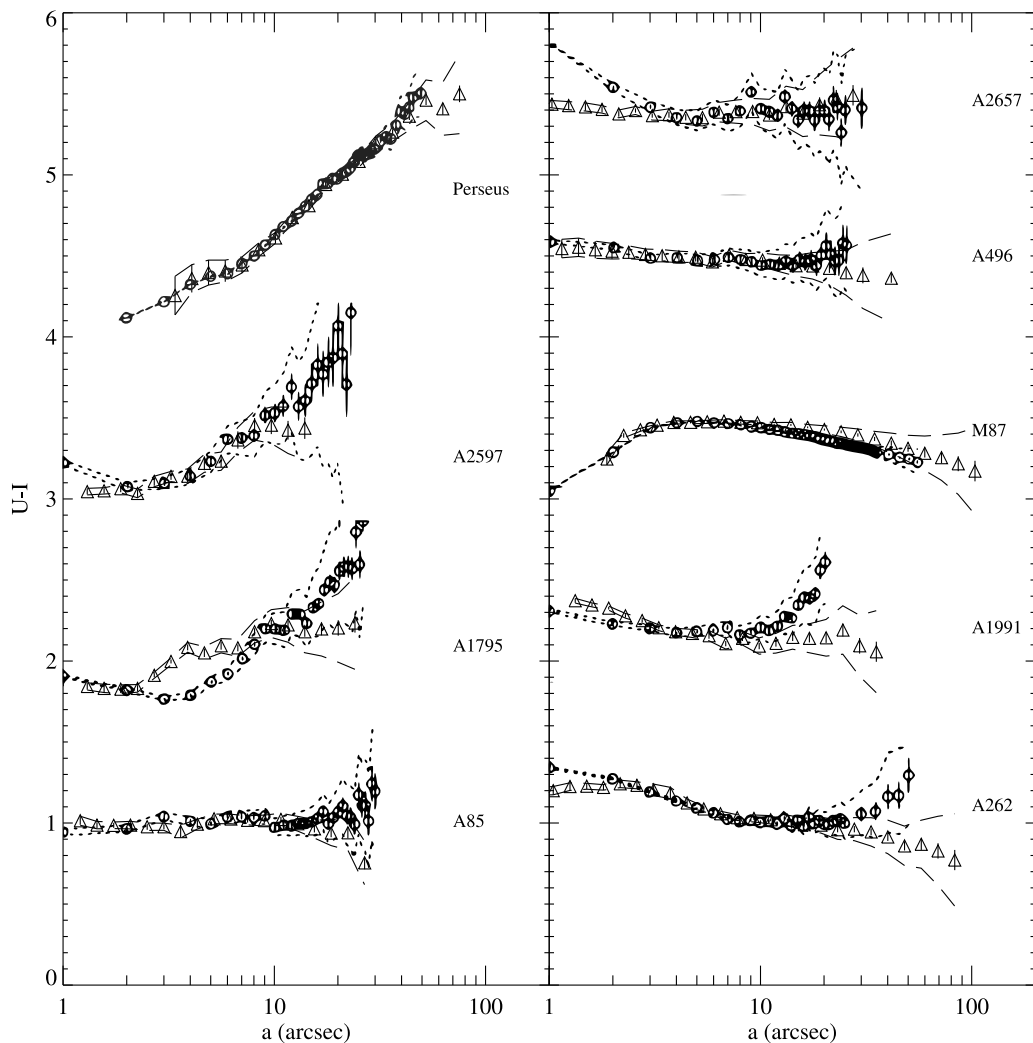


Figure 4.5: Comparison of our $U - I$ color profiles (triangles) to those of McNamara & O'Connell (1992) (circles) for the objects common to both samples.

Comparison with Other Studies and between Observing Runs

As a check for systematic errors in our reduction and analysis, we can compare our color profiles both to profiles from the literature and between different observing runs. In Figure 4.5, we compare our $U - I$ profiles with those from Figure 5 of McNamara & O'Connell (1992). In general, the profiles agree well within the errors over the inner

10-20 arcsec. At the extreme inner radii there is often some discrepancy, probably due to seeing effects at $a \lesssim 2$ arcsec, as the images of McNamara & O'Connell (1992) were not matched between bands for different seeing. At the extreme outer radii ($a \gtrsim 10 - 20$ arcsec) our profiles do not match well, as those of McNamara & O'Connell (1992) often show a steep positive gradient that ours do not (particularly apparent in the profiles of A1991 and A262). This effect may be due to misestimation of the sky by McNamara & O'Connell (1992), as they used a much smaller CCD (FOV $\sim 2.5 \times 2.5$ arcmin compared to our smallest FOV of 9.4×9.4 arcmin) which may have resulted in sky boxes with some contamination from the central galaxy's halo. Otherwise, the only significant discrepancy is in the $3 < a < 6$ arcsec region of the profile of A1795. We believe the bluer colors that McNamara & O'Connell (1992) find in this region are due to differences in the annuli used to measure the surface brightness, as the U -band image shows a linear blue feature in this region, the color of which would be diluted if fairly circular annuli are used (as we have done).

As a further check of consistency, we also compare profiles taken from observations made during different runs and at different telescopes. In Figure 4.6 we show profiles for three objects that we observed twice. A2390 was observed with the MDM 2.4-m telescope and the KPNO 4-m telescope; A2261 and A2244 were observed twice with MDM. The profiles agree well, with the exception of the inner 2 arcsec of the A2390 profiles, which is probably due to seeing differences between the two observations.

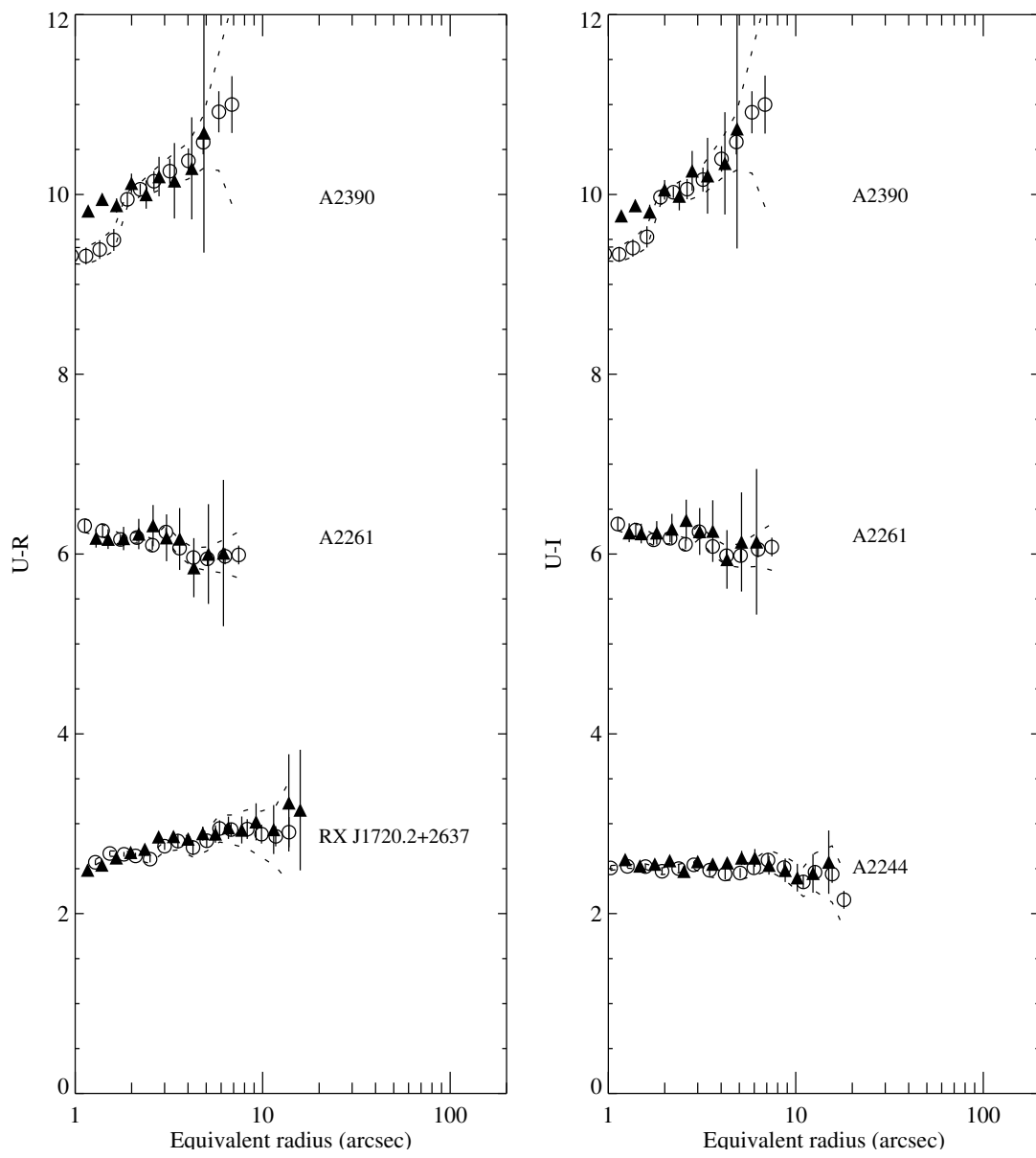


Figure 4.6: Comparison of $U - R$ color profiles (left) and $U - I$ color profiles (right) from different observing runs: A2390 and RX J1720.2+2637 – MDM (triangles) and KPNO (circles), A2261 and A2244 – MDM September 2005 (triangles) and MDM May 2006 (circles).

4.4.3 Analysis of X-ray Data

Chandra's high spatial resolution makes it possible for the first time to derive the properties of the ICM on scales comparable to those of optical observations ($r \sim 1\text{-}2$ arcsec). Therefore, it is now possible to compare the ICM properties (such as cooling time) with the optical properties in the same region. We derived the following ICM properties: temperature, density, pressure, entropy, and cooling time. The temperature and density were recovered directly from the models fit to the spectra during deprojections, and the pressure was calculated from these quantities as $P = 2n_e kT$ (see 2.2.3). The entropy is defined as in Lloyd-Davies et al. (2000):

$$S = kTn_e^{-2/3}, \quad (4.6)$$

and has units of keV cm².

A primary objective of this study is to determine how the ICM cooling times relate to the optical colors. In particular, we are interested in the core of the cluster, where the cooling times are the shortest. We can use the fact that the emissivity and hence surface brightness, again for a fully ionized plasma, is a strong function of the density ($\epsilon \sim n_e^2 [kT]^{-3/2}$) to extrapolate the density in close to the core using the surface brightness profile of the ICM. We used the deprojection method described in Section 2.2.3 and the assumption that the ICM is isothermal to transform from surface brightness to density. We extracted the surface brightness profile in circular annuli with 200–500 counts each, after background subtraction, and normalized the

resulting density profile using the coarser density profile derived using the PROJCT model. We then used the normalized density profile to find the density typically to within an outer radius of 4–5 arcsec. When calculating the cooling time using this density, we assumed that the temperature and abundance of the gas are constant in the inner region and equal to the derived emission-weighted values. Table 4.3 lists the central properties of the ICM in each system, derived as close as possible to the core (after the exclusion of any non-thermal point sources).

Additionally, to make comparisons between objects at a single physical radius, we derived the cooling time at 12 kpc using simple linear interpolation in $\log(t_{\text{cool}}) - \log(r)$ space. The 12 kpc radius was the smallest physical radius that could be achieved across most of our sample (excluding only A520). Table 4.4 lists the derived ICM properties at 12 kpc for the remaining systems. Lastly, we interpolated the cooling time profiles to find the cooling time at the radius of the CDG’s core (also listed in Table 4.4).

Table 4.3. Central ICM Properties.

System	r (arcsec)	r (kpc)	n_e (cm $^{-3}$)	kT (keV)	Entropy (keV cm 2)	t_{cool} (10 8 yr)
A85	2.4	2.6	0.107 $^{+0.009}_{-0.008}$	2.06 $^{+0.15}_{-0.12}$	9.1 $^{+0.8}_{-0.9}$	2.0 $^{+0.5}_{-0.5}$
3C 28	2.2	7.2	0.053 $^{+0.015}_{-0.009}$	1.29 $^{+0.12}_{-0.19}$	9.1 $^{+2.0}_{-1.7}$	3.5 $^{+1.6}_{-1.4}$
A133	3.0	3.3	0.048 $^{+0.004}_{-0.005}$	1.77 $^{+0.08}_{-0.06}$	13.5 $^{+1.1}_{-1.1}$	3.0 $^{+1.0}_{-0.7}$
A223	2.0	6.7	0.019 $^{+0.003}_{-0.003}$	5.50 $^{+0.80}_{-0.61}$	76.3 $^{+11.2}_{-8.7}$	23.9 $^{+5.5}_{-5.2}$
A262	2.0	0.7	0.067 $^{+0.019}_{-0.019}$	0.86 $^{+0.01}_{-0.01}$	5.2 $^{+0.3}_{-0.4}$	1.5 $^{+0.5}_{-0.5}$
A383	1.5	4.6	0.116 $^{+0.010}_{-0.012}$	2.03 $^{+0.25}_{-0.26}$	8.5 $^{+1.2}_{-1.2}$	2.0 $^{+0.6}_{-0.6}$
AWM 7	2.2	0.8	0.140 $^{+0.015}_{-0.013}$	1.18 $^{+0.07}_{-0.07}$	4.4 $^{+0.4}_{-0.4}$	1.2 $^{+0.3}_{-0.3}$
Perseus	11.8	4.2	0.150 $^{+0.005}_{-0.005}$	4.39 $^{+0.46}_{-0.39}$	15.5 $^{+1.7}_{-1.4}$	2.6 $^{+0.4}_{-0.3}$
2A 0335+096	3.4	2.4	0.100 $^{+0.011}_{-0.011}$	1.32 $^{+0.07}_{-0.09}$	6.1 $^{+0.6}_{-0.6}$	1.8 $^{+0.5}_{-0.5}$
A478	1.5	2.6	0.197 $^{+0.014}_{-0.015}$	2.68 $^{+0.28}_{-0.28}$	7.9 $^{+0.9}_{-0.9}$	1.4 $^{+0.3}_{-0.3}$
A496	1.0	0.6	0.198 $^{+0.031}_{-0.025}$	1.20 $^{+0.13}_{-0.15}$	3.5 $^{+0.5}_{-0.5}$	0.9 $^{+0.3}_{-0.2}$
A520	7.7	25.2	0.005 $^{+0.001}_{-0.001}$	7.07 $^{+3.24}_{-0.90}$	253.8 $^{+120.4}_{-43.2}$	117.0 $^{+65.4}_{-43.4}$
MS 0735.6+7421	2.9	10.1	0.067 $^{+0.002}_{-0.002}$	3.18 $^{+0.22}_{-0.24}$	19.2 $^{+1.4}_{-1.5}$	4.8 $^{+0.6}_{-0.6}$
PKS 0745-191	2.5	4.8	0.143 $^{+0.010}_{-0.010}$	2.62 $^{+0.37}_{-0.36}$	9.5 $^{+1.4}_{-1.4}$	2.2 $^{+0.5}_{-0.5}$
A1361	2.0	4.2	0.044 $^{+0.010}_{-0.010}$	2.59 $^{+0.16}_{-0.22}$	20.7 $^{+1.4}_{-1.9}$	6.2 $^{+1.7}_{-1.7}$
A1413	3.8	9.5	0.039 $^{+0.002}_{-0.001}$	6.14 $^{+1.35}_{-1.00}$	53.4 $^{+11.8}_{-8.8}$	12.9 $^{+2.8}_{-2.4}$
M87	5.9	0.5	0.191 $^{+0.009}_{-0.009}$	0.94 $^{+0.02}_{-0.02}$	2.8 $^{+0.1}_{-0.1}$	0.7 $^{+0.1}_{-0.1}$
HCG 62	2.0	0.6	0.072 $^{+0.014}_{-0.014}$	0.67 $^{+0.01}_{-0.01}$	3.9 $^{+0.3}_{-0.2}$	1.4 $^{+0.4}_{-0.4}$
A1650	3.0	4.7	0.043 $^{+0.002}_{-0.002}$	4.26 $^{+1.59}_{-0.90}$	34.4 $^{+12.9}_{-7.4}$	8.4 $^{+2.6}_{-1.7}$
Coma	9.8	4.6	0.008 $^{+0.003}_{-0.003}$	2.75 $^{+3.45}_{-1.61}$	66.9 $^{+85.4}_{-42.6}$	34.3 $^{+68.4}_{-32.7}$
A1795	2.0	2.4	0.069 $^{+0.016}_{-0.016}$	2.74 $^{+0.57}_{-0.37}$	16.3 $^{+3.5}_{-2.4}$	4.0 $^{+1.6}_{-1.4}$
A1991	2.2	2.5	0.077 $^{+0.011}_{-0.011}$	0.77 $^{+0.02}_{-0.02}$	4.2 $^{+0.4}_{-0.4}$	1.3 $^{+0.3}_{-0.3}$
MS 1455.0+2232	1.3	5.3	0.095 $^{+0.020}_{-0.020}$	4.40 $^{+1.36}_{-0.90}$	21.1 $^{+5.2}_{-5.2}$	3.1 $^{+2.5}_{-1.3}$
RXC J1504.1-0248	1.1	3.8	0.180 $^{+0.011}_{-0.012}$	6.87 $^{+3.82}_{-2.53}$	21.5 $^{+12.0}_{-8.0}$	3.1 $^{+1.1}_{-1.1}$
A2029	0.6	0.9	0.373 $^{+0.036}_{-0.031}$	2.88 $^{+0.33}_{-0.22}$	5.6 $^{+0.7}_{-0.5}$	0.6 $^{+0.2}_{-0.1}$
A2052	3.9	2.7	0.017 $^{+0.002}_{-0.002}$	0.71 $^{+0.04}_{-0.08}$	10.5 $^{+1.0}_{-1.4}$	6.4 $^{+4.7}_{-2.4}$
A2065	2.0	2.7	0.037 $^{+0.011}_{-0.011}$	1.97 $^{+0.35}_{-0.21}$	17.8 $^{+3.3}_{-2.3}$	7.0 $^{+3.1}_{-2.7}$
RX J1532.8+3021	2.0	9.6	0.107 $^{+0.009}_{-0.009}$	3.32 $^{+0.29}_{-0.28}$	14.8 $^{+1.3}_{-1.3}$	3.3 $^{+0.5}_{-0.5}$
A2218	3.9	11.7	0.008 $^{+0.003}_{-0.003}$	3.44 $^{+0.96}_{-0.56}$	83.3 $^{+24.0}_{-14.7}$	36.9 $^{+21.3}_{-18.0}$
Hercules A	2.0	5.3	0.078 $^{+0.010}_{-0.010}$	2.04 $^{+0.19}_{-0.21}$	11.2 $^{+1.2}_{-1.2}$	3.2 $^{+0.7}_{-0.8}$
A2244	2.0	3.5	0.046 $^{+0.008}_{-0.008}$	4.58 $^{+0.92}_{-0.60}$	35.6 $^{+7.3}_{-5.1}$	7.1 $^{+2.9}_{-2.1}$
NGC 6338	1.5	0.8	0.236 $^{+0.022}_{-0.018}$	0.99 $^{+0.05}_{-0.06}$	2.6 $^{+0.2}_{-0.2}$	0.7 $^{+0.1}_{-0.1}$
RX J1720.2+2637	1.7	4.8	0.099 $^{+0.017}_{-0.019}$	2.97 $^{+0.83}_{-0.61}$	13.8 $^{+4.2}_{-3.3}$	2.9 $^{+1.9}_{-1.4}$
MACS J1720.2+3536	2.2	11.7	0.076 $^{+0.005}_{-0.006}$	3.66 $^{+0.34}_{-0.25}$	20.4 $^{+2.1}_{-1.8}$	3.8 $^{+1.0}_{-0.8}$
A2261	2.0	7.1	0.043 $^{+0.010}_{-0.010}$	5.76 $^{+1.35}_{-0.92}$	46.6 $^{+11.3}_{-8.2}$	7.9 $^{+4.2}_{-3.1}$
A2319	4.4	4.8	0.028 $^{+0.014}_{-0.014}$	11.32 $^{+7.47}_{-3.41}$	122.2 $^{+80.8}_{-37.1}$	26.2 $^{+16.0}_{-15.7}$
A2390	0.6	2.3	0.199 $^{+0.010}_{-0.015}$	3.39 $^{+1.35}_{-0.86}$	10.0 $^{+4.0}_{-2.6}$	1.9 $^{+0.6}_{-0.5}$
A2409	3.0	7.6	0.013 $^{+0.008}_{-0.008}$	4.82 $^{+0.98}_{-0.68}$	88.5 $^{+19.5}_{-14.5}$	23.6 $^{+19.3}_{-17.2}$
A2597	3.4	5.5	0.075 $^{+0.005}_{-0.005}$	1.66 $^{+0.12}_{-0.14}$	9.3 $^{+0.8}_{-0.9}$	3.0 $^{+0.5}_{-0.5}$
A2626	2.0	2.1	0.063 $^{+0.014}_{-0.014}$	2.54 $^{+0.75}_{-0.64}$	16.0 $^{+4.9}_{-4.2}$	4.4 $^{+2.2}_{-2.0}$
A2657	3.0	2.3	0.017 $^{+0.009}_{-0.009}$	3.84 $^{+1.39}_{-0.87}$	58.2 $^{+22.2}_{-14.8}$	19.5 $^{+17.3}_{-14.3}$
A2670	3.0	4.3	0.026 $^{+0.012}_{-0.012}$	3.38 $^{+0.90}_{-0.65}$	38.3 $^{+12.4}_{-10.7}$	7.9 $^{+9.0}_{-6.8}$

Table 4.4. Interpolated ICM Cooling Times.

System	t_{cool} at 12 kpc (10^8 yr)	t_{cool} at r_{gal} (10^8 yr)	$r_{\text{gal}}^{\text{a}}$ (kpc)
A85	$7.0^{+0.8}_{-0.8}$	$3.5^{+0.5}_{-0.5}$	5.2
3C 28	$5.6^{+1.6}_{-1.5}$	$6.0^{+1.6}_{-1.5}$	12.9
A133	$8.0^{+1.1}_{-0.8}$	$5.0^{+1.0}_{-0.7}$	6.5
A223	$41.7^{+14.8}_{-14.5}$	$35.7^{+9.7}_{-9.4}$	< 6.8
A262	$12.2^{+0.6}_{-0.6}$	$2.2^{+0.7}_{-0.7}$	1.7
A383	$4.8^{+0.8}_{-0.7}$	$2.0^{+0.6}_{-0.6}$	< 6.3
AWM 7	$18.1^{+2.2}_{-1.9}$	$1.2^{+0.3}_{-0.3}$	< 0.7
Perseus	$5.6^{+0.4}_{-0.4}$	$2.6^{+0.4}_{-0.3}$	< 0.7
2A 0335+096	$3.7^{+0.6}_{-0.6}$	$3.5^{+0.6}_{-0.5}$	10.6
A478	$4.8^{+0.4}_{-0.3}$	$1.4^{+0.3}_{-0.3}$	< 3.3
A496	$7.9^{+0.2}_{-0.2}$	$0.9^{+0.3}_{-0.2}$	< 1.3
A520	...	$225.4^{+32.7}_{-22.9}$	494.4
MS 0735.6+7421	$5.8^{+0.6}_{-0.6}$	$4.8^{+0.6}_{-0.6}$	< 7.0
PKS 0745-191	$3.6^{+0.5}_{-0.5}$
A1361	$7.9^{+2.5}_{-2.5}$	$6.3^{+1.7}_{-1.7}$	4.6
A1413	$14.8^{+2.8}_{-2.4}$	$12.9^{+2.8}_{-2.4}$	< 5.0
M87	$10.4^{+0.5}_{-0.5}$	$0.7^{+0.1}_{-0.1}$	< 0.2
HCG 62	$13.3^{+3.1}_{-2.6}$	$1.6^{+0.5}_{-0.5}$	< 0.6
A1650	$15.9^{+2.9}_{-2.0}$	$8.4^{+2.6}_{-1.7}$	< 3.2
Coma	$74.0^{+72.0}_{-36.4}$...	b
A1795	$7.6^{+1.4}_{-1.2}$	$5.9^{+2.2}_{-1.9}$	7.5
A1991	$5.6^{+0.4}_{-0.4}$	$4.0^{+0.6}_{-0.5}$	8.8
MS 1455.0+2232	$4.1^{+2.8}_{-1.4}$	$3.3^{+2.5}_{-1.3}$	< 8.0
RXC J1504.1-0248	$2.9^{+1.3}_{-1.3}$	$3.0^{+1.1}_{-1.1}$	< 7.0
A2029	$6.4^{+0.3}_{-0.2}$
A2052	$7.8^{+5.9}_{-2.9}$
A2065	$15.6^{+3.1}_{-2.4}$	$16.0^{+6.9}_{-6.1}$	13.2
RX J1532.8+3021	$3.8^{+0.6}_{-0.6}$	$4.3^{+0.7}_{-0.7}$	< 9.8
A2218	$37.0^{+22.3}_{-19.2}$	$40.9^{+21.3}_{-17.1}$	30.1
Hercules A	$6.9^{+1.3}_{-1.4}$	$4.7^{+1.2}_{-1.2}$	< 5.3
A2244	$18.0^{+4.1}_{-2.7}$	$9.5^{+4.0}_{-3.0}$	< 3.6
NGC 6338	$11.6^{+1.9}_{-1.8}$	$0.7^{+0.1}_{-0.1}$	< 1.1
RX J1720.2+2637	$5.5^{+2.0}_{-1.5}$	$4.3^{+1.9}_{-1.4}$	8.5
MACS J1720.2+3536	$3.9^{+1.0}_{-0.8}$	$3.8^{+1.0}_{-0.8}$	< 10.6
A2261	$9.9^{+5.6}_{-4.2}$	$9.4^{+5.1}_{-3.8}$	< 7.2
A2319	$27.5^{+17.8}_{-17.6}$	$49.0^{+22.7}_{-22.1}$	50.1
A2390	$6.4^{+0.7}_{-0.6}$	$2.8^{+0.6}_{-0.5}$	< 7.3
A2409	$29.2^{+27.9}_{-25.8}$	$31.2^{+18.8}_{-14.9}$	46.6
A2597	$5.3^{+0.7}_{-0.7}$	$3.0^{+0.5}_{-0.5}$	< 3.2
A2626	$13.9^{+3.4}_{-3.1}$	$5.2^{+2.6}_{-2.4}$	2.6
A2657	$45.9^{+24.4}_{-17.8}$	$22.9^{+20.7}_{-17.3}$	3.5
A2670	$27.2^{+24.1}_{-17.0}$	$8.0^{+9.2}_{-7.0}$	< 2.9

^aRadius from the X-ray core to the CDG's core. Separations of less than 2 arcsec are treated as upper limits.

^bThe Coma data lacked sufficient counts to derive a cooling time at the CDG's radius.

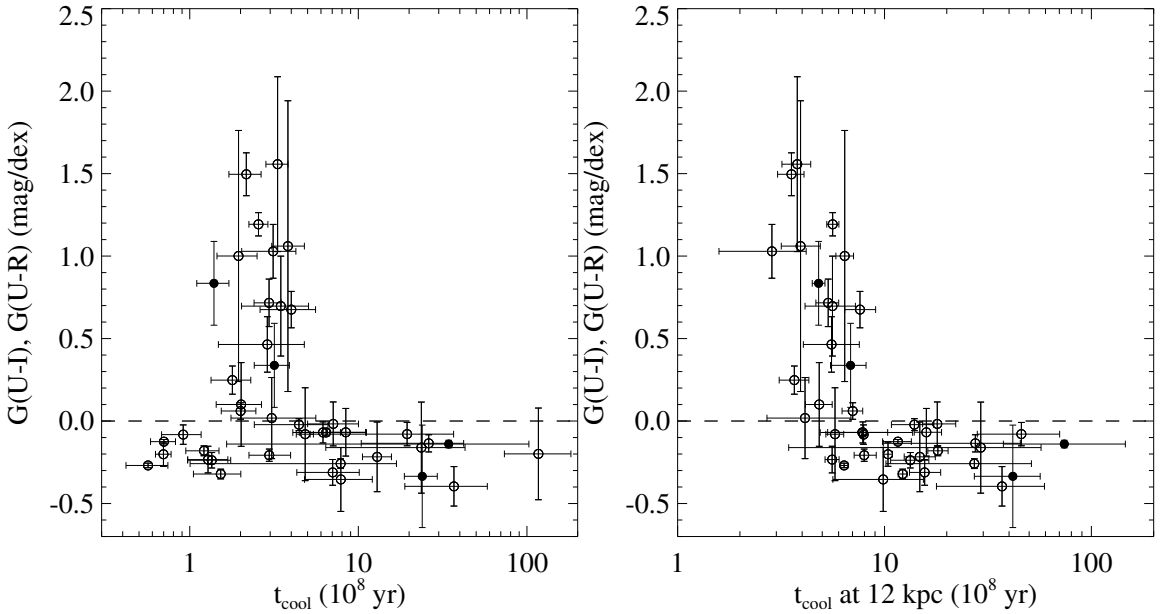


Figure 4.7: *Left:* Color gradient versus the central cooling time. *Right:* Color gradient versus the cooling time at a radius of 12 kpc. $U - I$ gradients (plotted as empty symbols) are used when available; $U - R$ gradients (filled symbols) are used when $U - I$ gradients are unavailable.

4.4.4 Comparing Colors and Cooling Times

The cooling time of the ICM is a critical measure of its thermal state. If the cooling time is sufficiently short (on the order of the age of the system or less), significant condensation of gas should occur unless heating balances the cooling entirely. In this section, we investigate whether the cooling times we derived from *Chandra* data are related to the presence of excess blue emission in the CDG, on the same spatial scales.

To this end, in Figure 4.7, we plot the optical color gradients of the CDG against the central cooling times of the cluster’s ICM. We plot the $U - I$ color gradient when available; otherwise, we plot the $U - R$ gradient, as they are almost equivalent (see Section 4.4.2). The left panel shows the emission-weighted central cooling time

derived as close to the core as our data allow us to achieve (see Table 4.3). Since the systems in our sample vary greatly in redshift, we plot in the right panel the cooling time at 12 kpc (see Table 4.4). At 12 kpc, the very short cooling times (those below $\sim 2 \times 10^8$ yr) measured at the center disappear, demonstrating that their short cooling times relative to the rest of the sample are due to resolution effects.

It is apparent from these figures that positive gradients, which are indicative of active star formation, occur only in objects with central ($r \lesssim 12$ kpc) cooling times below $\sim 7 - 8 \times 10^8$ yr. This finding strongly supports the scenario described in Section 4.3, wherein the cooling ICM is either directly fueling the star formation or is fueling the central AGN that is triggering the star formation. However, it is also apparent that the presence of a short central cooling time does not guarantee the presence of a positive color gradient, as several of the objects with cooling times below $\sim 7 \times 10^8$ yr do not have blue cores (although the majority do).

To emphasize that the systems with blue central colors are different on average from those with red colors, we show in Figure 4.8 histograms of the cooling times at 12 kpc for the objects in our optical sample. We have divided the sample into those systems with positive color gradients (blue systems) and those with negative gradients (red systems). Compared with the red systems, the blue systems clearly prefer shorter cooling times. A Kolmogorov-Smirnov (K-S) test gives a probability of just 2×10^{-6} that the red and blue samples are drawn randomly from the same

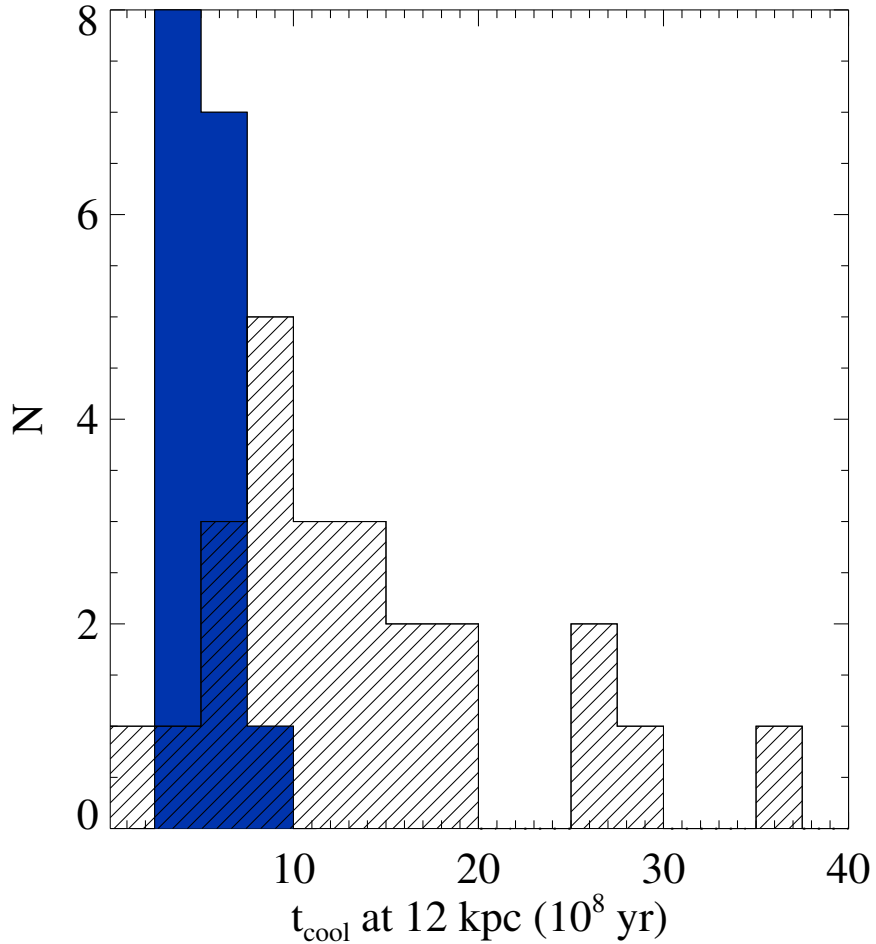


Figure 4.8: Histogram of the cooling times at 12 kpc for objects with positive color gradients (blue) and negative gradients (hatched). The two samples are clearly different.

parent distribution of cooling times. This result is a strong indicator that the cooling flow and star formation in the CDG are connected.

For comparison with the color gradients, we also plot the Δ colors against the cooling times in Figure 4.9. In this figure, the overall relationship between cooling time and the presence of star formation is unchanged from Figure 4.7. However, we

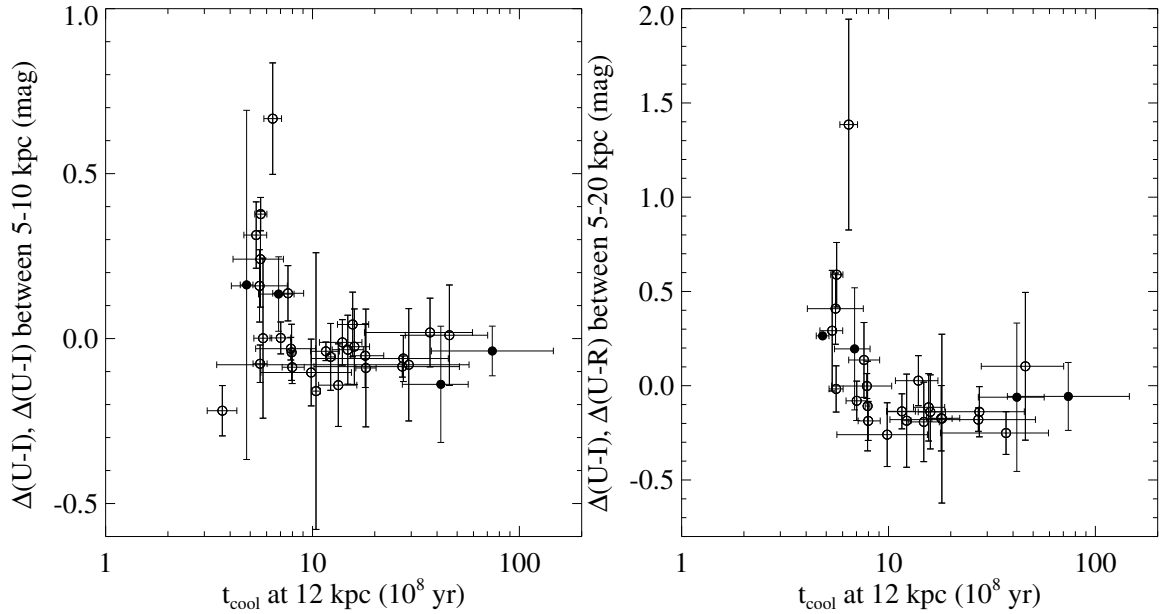


Figure 4.9: *Left:* $\Delta(U - R)$ and $\Delta(U - I)$ between 5-10 kpc versus the cooling time at 12 kpc. *Right:* $\Delta(U - R)$ and $\Delta(U - I)$ between 5-20 kpc versus the cooling time at 12 kpc. Symbols are the same as those in Figure 4.7.

do not see clear evidence that star formation becomes more extended in a smooth fashion as the cooling time decreases, as might be expected if cooling is distributed.

The lack of excess blue emission in some objects with short cooling times may be due to several factors. One possibility is obscuration by dust, which is common in the cores of many CDGs. Dust will preferentially scatter and absorb short-wavelength emission, resulting in observed colors that are redder than the intrinsic ones. However, dust in CDGs is generally observed to be patchy or filamentary (e.g., Laine et al., 2003), not spread smoothly across the galaxy in significant quantities (see however Silva & Wise, 1996). Therefore, it is unlikely that dust would obscure the entire star forming region if star formation in all of the objects with short cooling times is

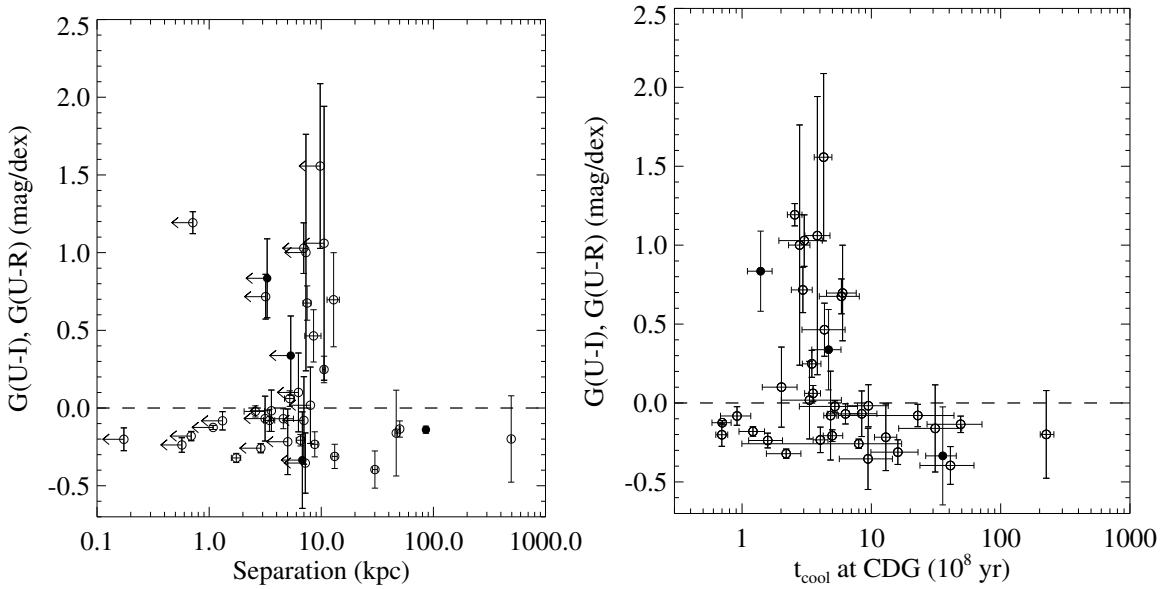


Figure 4.10: *Left:* Color gradient versus the separation between the CDG's core and the cluster's core. Due to uncertainties in the core positions of ~ 1 arcsec (due to pointing errors only, possible systematic errors in core locations are not included but are likely small), separations of less than 2 arcsec are shown as upper limits. *Right:* Color gradient versus the cooling time at the radius of the CDG's core. Symbols are the same as those in Figure 4.7.

similar. However, it would be useful to obtain far-IR ($60 \mu\text{m}$) observations of these systems to measure the amount of reprocessed UV light.

Another possibility is that the red systems do not lie at the core of the cooling flow where cooling times are short, but instead reside at larger radii where the cooling times are relatively long. It is quite common to find the CDG offset 100 kpc or more from the X-ray core (e.g., Patel et al., 2006; Edwards et al., 2007). To investigate this possibility, we plot in the left panel of Figure 4.10 the color gradient against the physical separation between the CDG's core and the cluster's core. In the right panel we plot the color gradient against the cooling time of the ICM at the location of the

CDG's core. In neither plot do the red objects segregate to large separations or long cooling times (though those objects with large separations have long cooling times). However, the blue objects all have small ($\lesssim 20$ kpc) separations. Therefore, although a small separation between the X-ray core and the galaxy does not guarantee a blue core, it appears to be a necessary condition. This result agrees with the findings of [Edwards et al. \(2007\)](#), who find that all the CDGs in their sample with strong optical line emission (indicative of an ionizing source, such as young stars or AGN emission, near cool gas) lie within 50 kpc of the cluster's X-ray core (see also [Crawford et al., 1999](#)). Therefore, the CDG's location relative to the cluster's core is critical to the presence of star formation, a finding which supports the hypothesis that the cooling ICM, which preferentially cools in the core, fuels the star formation.

Another possible reason for the lack of star formation in some objects with short cooling times is that the blue systems occupy different temporal locations on the cycle of cooling and heating discussed in Section [3.4.1](#) than the red systems. The blue systems could reside in clusters in which the central AGN is not currently supplying sufficient heat to offset cooling, whereas in the red systems, the AGN prevents large amounts of cooling from occurring, despite the sometimes short cooling times. In this scenario, one might expect that those objects with large amounts of heating relative to cooling would be redder than those with insufficient heating.

To test this prediction, we plot in Figure [4.11](#) the color gradient versus the ratio of cavity power to ICM luminosity, $P_{\text{cav}}/L_{\text{ICM}}$ (see Section [3.4.1](#) for definitions). While

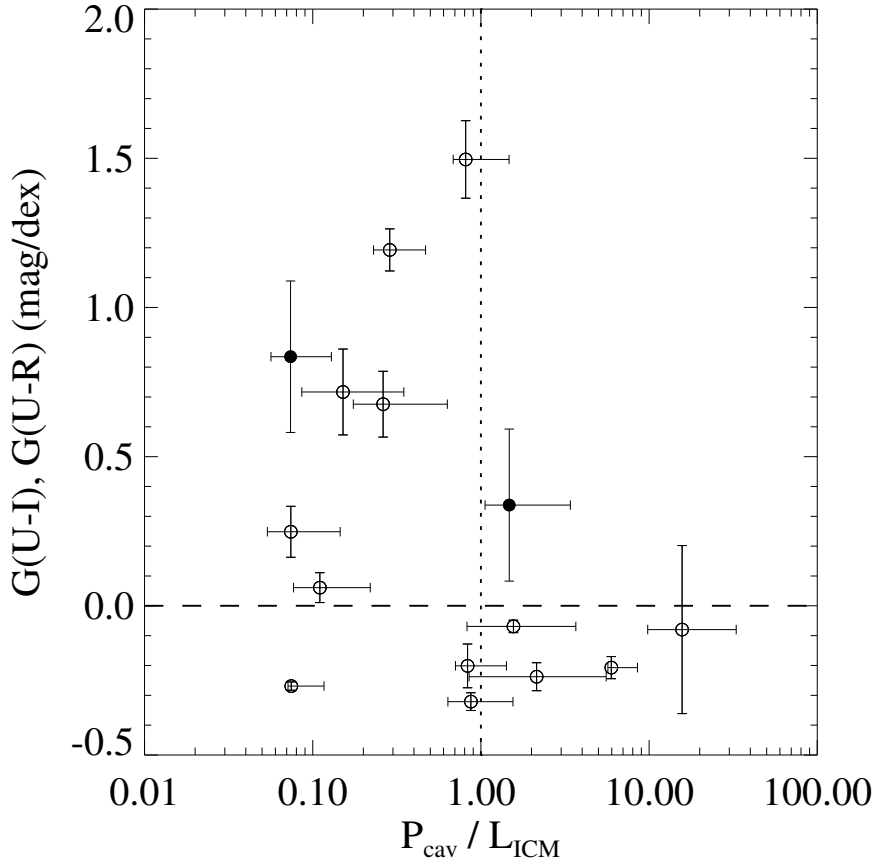


Figure 4.11: Color gradient versus the ratio of cavity power to ICM luminosity. Symbols are the same as those in Figure 4.7.

our sample lacks a large number of systems with a high ratio of cavity power to cooling luminosity, it appears that systems with excess blue emission are more likely to have a low ratio of $P_{\text{cav}}/L_{\text{ICM}}$ (i.e. insufficient heating to balance cooling). The average (median) ratio of $P_{\text{cav}}/L_{\text{ICM}}$ for objects with positive gradients is 0.4 (0.3); for objects with negative gradients, it is 3.9 (1.6). The K-S test gives a probability of 0.02 that the positive- and negative-gradient samples share the same distribution of the ratio of cavity power to ICM luminosity. This finding lends support to the feedback scenario outlined above, and can explain 3 of the 5 red systems in Figure 4.7 with a cooling

time at 12 kpc less than $\sim 8 \times 10^8$ yr. The two remaining systems are A2029 and A1991, which do not appear to have enough AGN heating to balance cooling and yet have short cooling times and are red. However, [McNamara & O'Connell \(1992\)](#) find a positive $U - I$ gradient in A1991 [$G(U - I) = 0.036 \pm 0.022$]; therefore, we have probably missed the blue emission in this system. As for A2029, it is possible that we have underestimated the cavity power or have caught the system just before star formation will occur.

4.4.5 Comparing Colors and Other ICM Properties

We also investigate the dependence of the presence of blue emission on the central temperature, pressure, density, and entropy of the ICM. We plot each of these against the $U - I$ gradients in Figures 4.12 and 4.13. The central temperature (Figure 4.12, *left*) and pressure (Figure 4.12, *right*) show no clear correlations with the $U - I$ gradient; however, it appears that high central densities (Figure 4.13, *left*) are required for blue colors, in agreement with the cooling time findings discussed above (since $t_{\text{cool}} \propto n_e$ for free-free emission). Lastly, we also find that blue gradients occur only in objects in our sample whose central entropies are below ~ 30 kev cm $^{-2}$ (Figure 4.13, *right*). Interestingly, [Voit & Donahue \(2005\)](#) postulate that an entropy floor of ~ 10 kev cm 2 is most likely an indicator of recent AGN feedback, providing an indirect connection between star formation and feedback.

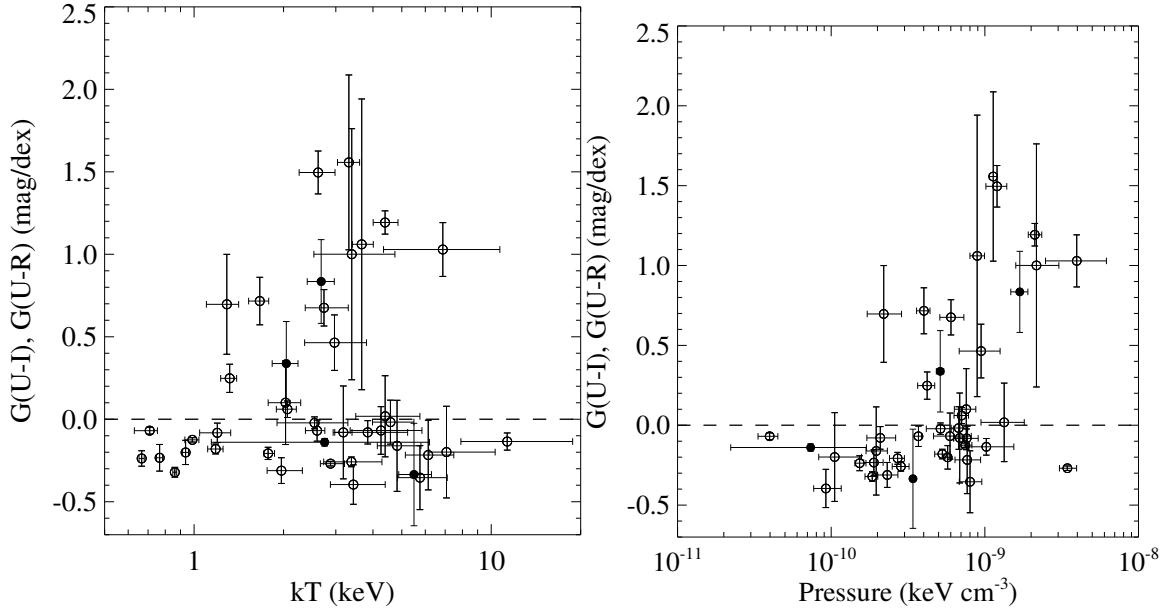


Figure 4.12: *Left:* Color gradient versus the central temperature. *Right:* Color gradient versus the central pressure. Symbols are the same as those in Figure 4.7.

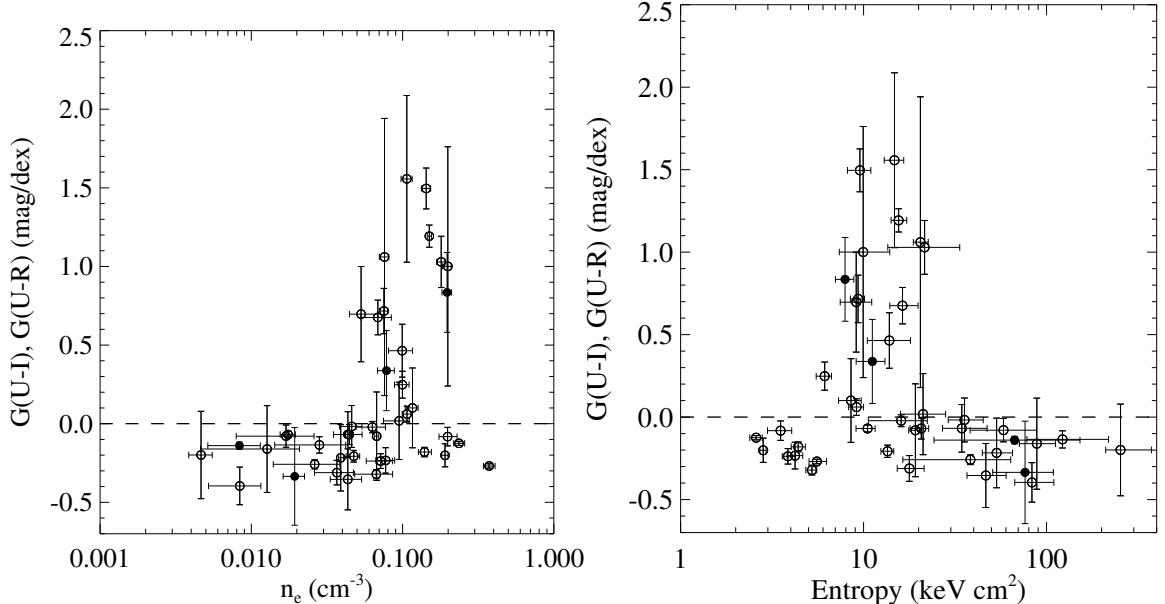


Figure 4.13: *Left:* Color gradient versus the central density. *Right:* Color gradient versus the central entropy. Symbols are the same as those in Figure 4.7.

4.5 Summary

We have used published star formation rates and derived broadband optical colors for a sample of CDGs to investigate possible connections between star formation and the cooling flow. We find that upper limits on net cooling rates of gas out of the ICM are approaching the star formation rates of the central galaxy (to an average ratio of cooling to total star formation rate of four to one), and in some cases are consistent with one another. Inhomogeneities in star formation rates and the lack of firm detections of cooling in X-ray data are the main factors that limit our conclusions. Nevertheless, this rough agreement is far different from the situation a decade ago, when the best X-ray cooling rates were tens to hundreds of times the star formation rates.

While it has been known for some time that the signatures of star formation in CDGs are related to the bulk ICM properties of the cluster such as the classical cooling rate ([McNamara & O'Connell, 1992](#)), we show that, on similar spatial scales, the presence of central blue colors, indicative of active star formation, depends upon the properties of the cooling flow. Blue cores are found to occur only in the clusters in our sample whose central ICM cooling time is less than $\sim 7 \times 10^8$ yr, whose central entropy is less than ~ 30 kev cm $^{-2}$, and where the separation between the X-ray core and the CDG is less than ~ 20 kpc. Finally, we find that the lack of the signatures of star formation in some systems with short cooling times could be due to excess heating by the central AGN that prevents any cooling from occurring.

These results strongly demonstrate a connection between star formation and the cooling flow, and support the feedback scenario in which the cooling ICM, the central AGN, and star formation are all interrelated.

CHAPTER 5

Bulge and Black Hole Growth

5.1 Introduction: the Magorrian Relation

Current theory posits that AGN are powered by the accretion of material onto a central black hole. Gravitational binding energy of the accreting material powers radiation and outflows from AGN as the black hole grows. The relativistic jets that are revealed by their synchrotron emission are a product of this process. The remaining accreting material goes to increasing the mass of the black hole. In a sense, AGN are the “smoking guns” of black hole growth. The fraction of accreted power that re-emerges from an AGN and its partitioning between radiation and outflows are not well understood, but probably depend on accretion rate (e.g., [Rees et al., 1982](#); [Narayan & Yi, 1994](#); [Abramowicz et al., 1995](#); [Churazov et al., 2005](#)). We can place lower limits on the AGN’s power using estimates of the power required to create the cavities associated with the radio lobes. This power may then be used to infer the minimum growth rate of the black hole.

As presented by [Ferrarese & Merritt \(2000\)](#) and [Gebhardt et al. \(2000\)](#), a correlation exists between the mass of the central black hole (M_{BH}) and the velocity dispersion (σ) of the galaxy’s bulge. This correlation suggests that the large-scale properties of the galaxy and the small-scale properties of the black hole are related

(the “Magorrian relation”, [Magorrian et al., 1998](#)). Estimates of the current growth rates of the black hole may be compared to the large-scale properties of the galaxy (such as the star formation rate) to trace the present day impact of bulge and black hole growth on this connection.

5.2 Quantifying Black Hole Growth

5.2.1 Black Hole Growth Rates

The energies and ages described in Section 3.2.4 may be used to infer the minimum growth rate of the black hole assuming the cavities were created by AGN jets fueled by accretion onto the central black hole. Although the luminous energy radiated by the AGN is not included in the cavity energies and must also be fueled by accretion, these systems are radiatively inefficient (e.g., [Bîrzan et al., 2004](#)), and the contribution of radiation to the current total power is negligible. The outbursts might pass through a radiatively efficient phase during their initial stages, but this phase could not have been long-lived, since cluster AGN do not now show the quasar-like activity, and should not therefore affect our results significantly. We stress that our black hole growth rates are lower limits; any energy in excess of the jet energy would result in underestimates of the average accretion rates, but we expect this effect to be small.

The jets are produced through the partial conversion (with efficiency ϵ) of the gravitational binding energy of the accreting material into outburst energy. The

energy required to create the cavities requires an accretion mass, M_{acc} , of

$$M_{\text{acc}} = \frac{E_{\text{cav}}}{\epsilon c^2}. \quad (5.1)$$

The value of ϵ depends on poorly understood details of the jet production process and, probably, on black hole spin. Under the usual assumption, that the maximum energy that can be extracted is determined by the binding energy of the last stable orbit, the upper limit on the efficiency ranges from $\epsilon \lesssim 0.06$ for a nonrotating black hole to $\epsilon \lesssim 0.4$ for an extreme Kerr black hole (Frank et al., 2002). We assume when calculating the energy of the outburst that each cavity represents $4pV$ of energy (i.e. that they are filled with a relativistic plasma).

Since some of the accreting material's mass goes to power the jets, the black hole's mass grows by

$$\Delta M_{\text{BH}} = (1 - \epsilon)M_{\text{acc}}. \quad (5.2)$$

Therefore, increased efficiency results in smaller black hole growth for a given outburst energy. The time-averaged accretion and black hole growth rates were found by dividing Equations 5.1 and 5.2 by the characteristic time scale discussed in Section 3.2.4. Table 5.1 lists the inferred mass by which the black hole grew and the average rate of growth during the outburst. The implied black hole growth rates vary across our sample by approximately four orders of magnitude, from $1.6 \times 10^{-4} M_{\odot} \text{ yr}^{-1}$ (M87) to $1.1 M_{\odot} \text{ yr}^{-1}$ (MS 0735.6+7421), with an average value of $\sim 0.1 M_{\odot} \text{ yr}^{-1}$ and a median value of $0.035 M_{\odot} \text{ yr}^{-1}$.

Table 5.1. Black Hole Masses and Growth Rates.

System	$M_{\text{BH,meas}}^{\text{a}}$ ($10^9 M_{\odot}$)	$M_{\text{BH},\sigma}$ ($10^9 M_{\odot}$)	$M_{\text{BH},L_K}^{\text{b}}$ ($10^9 M_{\odot}$)	$\Delta M_{\text{BH}}^{\text{c}}$ (M_{\odot})	M_{BH}^{c} ($M_{\odot} \text{ yr}^{-1}$)	Bondi ratio ^d ($\dot{M}_{\text{acc}}/\dot{M}_{\text{Bondi}}$)	Eddington ratio ^d ($\dot{M}_{\text{acc}}/\dot{M}_{\text{Edd}}$)
A85	...	1.1 $^{+0.6}_{-0.4}$	1.0 $^{+0.6}_{-0.4}$	2.5 $^{+2.5}_{-0.7} \times 10^5$	5.9 $^{+5.9}_{-1.7} \times 10^{-3}$	1.2 $^{+52}_{-1.7}$	2.6 $^{+5.2}_{-1.4} \times 10^{-4}$
A133	0.7 $^{+0.4}_{-0.3}$	5.0 $^{+2.0}_{-0.2} \times 10^6$	9.8 $^{+4.2}_{-0.4} \times 10^{-2}$	1.00 $^{+3300}_{-670}$	7.3 $^{+9.2}_{-2.9} \times 10^{-3}$
A262	...	0.4 $^{+0.2}_{-0.1}$	0.3 ± 0.1	2.5 $^{+2.0}_{-0.7} \times 10^4$	1.5 $^{+1.2}_{-0.4} \times 10^{-3}$	1.4 $^{+41}_{-9}$	2.1 $^{+3.2}_{-1.0} \times 10^{-4}$
Persens	...	0.3 ± 0.1	0.6 $^{+0.3}_{-0.2}$	3.8 $^{+3.9}_{-2.0} \times 10^6$	2.4 $^{+1.5}_{-0.5} \times 10^{-2}$	1.400 $^{+4200}_{-900}$	3.9 $^{+5.2}_{-1.7} \times 10^{-3}$
2A 0335+096	0.5 $^{+0.3}_{-0.2}$	2.2 $^{+2.0}_{-0.6} \times 10^5$	3.8 $^{+3.7}_{-1.2} \times 10^{-3}$	3.6 $^{+137}_{-26}$	3.6 $^{+7.1}_{-1.9} \times 10^{-4}$
A478	0.9 $^{+0.6}_{-0.5}$	3.0 $^{+2.3}_{-0.7} \times 10^5$	1.6 $^{+1.2}_{-0.4} \times 10^{-2}$	41 $^{+206}_{-32}$	9.0 $^{+17}_{-4.8} \times 10^{-4}$
MS 0735.6+7421	0.7 $^{+0.5}_{-0.3}$	3.2 $^{+3.5}_{-1.2} \times 10^8$	1.1 $^{+1.1}_{-0.4}$	18000 $^{+103000}_{-15000}$	7.9 $^{+20}_{-5.9} \times 10^{-2}$
PKS 0745-191	1.1 $^{+0.7}_{-0.3}$	1.4 $^{+1.1}_{-0.5} \times 10^7$	2.7 $^{+2.2}_{-0.4} \times 10^{-1}$	630 $^{+3570}_{-490}$	1.2 $^{+2.5}_{-0.6} \times 10^{-2}$
4C 55.16	0.5 $^{+0.3}_{-0.2}$	2.4 $^{+2.5}_{-0.9} \times 10^6$	6.7 $^{+7.0}_{-2.5} \times 10^{-2}$	1200 $^{+5600}_{-900}$	6.5 $^{+4.5}_{-1.6} \times 10^{-3}$
Hydra A	...	0.9 $^{+0.7}_{-0.4}$	0.4 $^{+0.2}_{-0.1}$	1.3 $^{+1.0}_{-0.2} \times 10^7$	6.8 $^{+3.1}_{-0.9} \times 10^{-2}$	210 $^{+1300}_{-170}$	3.7 $^{+5.6}_{-1.8} \times 10^{-3}$
RBS 797	7.5 $^{+2.7}_{-3.0} \times 10^6$	1.9 $^{+2.7}_{-0.9} \times 10^{-1}$
Zw 2701	0.6 $^{+0.4}_{-0.2}$	7.2 $^{+11}_{-4.1} \times 10^7$	1.0 $^{+1.4}_{-0.4}$	62000 $^{+453000}_{-54000}$	8.2 $^{+25}_{-6.0} \times 10^{-2}$
Zw 3146	2.6 $^{+2.4}_{-1.3}$	7.7 $^{+9.2}_{-2.3} \times 10^7$	0.9 $^{+0.1}_{-0.2}$	370 $^{+3060}_{-300}$	1.7 $^{+5.4}_{-1.0} \times 10^{-2}$
A1068	1.0 $^{+0.6}_{-0.4}$...	3.1 $\times 10^{-3}$	6.4 $^{+18}_{-18}$	1.6 $^{+1.0}_{-0.6} \times 10^{-4}$
M84	0.36	0.7 ± 0.2	0.12 ± 0.03	6.1 $^{+8.4}_{-3.3} \times 10^2$	1.6 $^{+2.3}_{-0.9} \times 10^{-4}$	0.44 $^{+1.4}_{-4.3}$	2.1 $^{+4.5}_{-1.4} \times 10^{-5}$
M87	3.3 ± 0.7	1.2 $^{+0.5}_{-0.3}$	0.3 ± 0.1	4.1 $^{+2.9}_{-0.6} \times 10^3$	1.0 $^{+0.9}_{-0.2} \times 10^{-3}$	0.04 $^{+0.33}_{-0.08}$	1.5 $^{+1.7}_{-0.4} \times 10^{-5}$
Centaurus	...	0.4 ± 0.1	0.3 ± 0.1	1.2 $^{+0.3}_{-0.3} \times 10^4$	1.2 $^{+0.9}_{-0.3} \times 10^{-3}$	2.4 $^{+5.9}_{-1.5}$	1.6 $^{+2.2}_{-0.7} \times 10^{-4}$
HCG 62	0.2 ± 0.1	9.3 $^{+5.5}_{-15} \times 10^3$	6.1 $^{+9.7}_{-3.6} \times 10^{-4}$	12 $^{+54}_{-10}$	1.4 $^{+3.7}_{-1.0} \times 10^{-4}$
A1795	...	0.6 $^{+0.3}_{-0.2}$	0.8 $^{+0.5}_{-0.3}$	9.4 $^{+13}_{-3.1} \times 10^5$	2.6 $^{+3.6}_{-0.9} \times 10^{-2}$	390 $^{+2660}_{-300}$	2.0 $^{+5.2}_{-1.1} \times 10^{-3}$
A1835	1.9 $^{+1.6}_{-0.9}$	9.5 $^{+10}_{-3.0} \times 10^6$	2.8 $^{+3.0}_{-1.0} \times 10^{-1}$	520 $^{+3570}_{-430}$	7.3 $^{+20}_{-4.7} \times 10^{-3}$
PKS 1404-267	...	0.4 ± 0.1	0.2 ± 0.1	2.3 $^{+2.9}_{-1.0} \times 10^4$	3.2 $^{+4.1}_{-1.0} \times 10^{-3}$	72 $^{+266}_{-53}$	4.3 $^{+9.2}_{-2.6} \times 10^{-4}$
MACS J1423.8+2404	5.8 $^{+11}_{-3.8} \times 10^6$	2.2 $^{+4.0}_{-1.4} \times 10^{-1}$
A2029	1.5 $^{+0.8}_{-0.5}$	2.1 $^{+1.6}_{-0.9}$	9.6 $^{+5.4}_{-0.3} \times 10^5$	1.4 $^{+0.8}_{-0.1} \times 10^{-2}$	7.0 $^{+26}_{-4.7}$	4.4 $^{+6.3}_{-1.7} \times 10^{-4}$	
A2052	0.4 $^{+0.2}_{-0.1}$	0.6 $^{+0.3}_{-0.2}$	3.6 $^{+4.5}_{-1.5} \times 10^5$	2.3 $^{+3.1}_{-1.7} \times 10^{-2}$	510 $^{+2710}_{-420}$	3.1 $^{+7.6}_{-1.9} \times 10^{-3}$	
MKW 3S	...	0.3 ± 0.1	7.7 $^{+7.9}_{-0.8} \times 10^6$	6.5 $^{+6.7}_{-0.7} \times 10^{-2}$	12000 $^{+98000}_{-9000}$	1.1 $^{+2.2}_{-0.4} \times 10^{-2}$	
A2199	0.7 $^{+0.3}_{-0.2}$	0.7 $^{+0.4}_{-0.2}$	1.5 $^{+1.3}_{-0.3} \times 10^6$	4.3 $^{+3.9}_{-0.7} \times 10^{-2}$	260 $^{+860}_{-170}$	3.1 $^{+4.9}_{-1.3} \times 10^{-3}$	
Hercules A	...	0.7 $^{+0.5}_{-0.3}$	6.3 $^{+8.1}_{-1.7} \times 10^6$	5.0 $^{+6.4}_{-1.4} \times 10^{-2}$	2100 $^{+13100}_{-1600}$	3.3 $^{+9.2}_{-1.9} \times 10^{-3}$	
3C 388	1.5 $^{+1.2}_{-0.7}$	0.6 $^{+0.3}_{-0.2}$	1.1 $^{+1.5}_{-0.4} \times 10^6$	3.1 $^{+4.4}_{-1.2} \times 10^{-2}$	960 $^{+750}_{-810}$	1.0 $^{+3.4}_{-0.7} \times 10^{-3}$	

Table 5.1 (continued)

System	$M_{\text{BH,meas}}^{\text{a}}$ ($10^9 M_\odot$)	$M_{\text{BH},\sigma}$ ($10^9 M_\odot$)	$M_{\text{BH},L_K}^{\text{b}}$ ($10^9 M_\odot$)	$\Delta M_{\text{BH}}^{\text{c}}$ (M_\odot)	$\dot{M}_{\text{BH}}^{\text{c}}$ ($M_\odot \text{ yr}^{-1}$)	Bondi ratio ^d ($\dot{M}_{\text{acc}}/\dot{M}_{\text{Bondi}}$)	Eddington ratio ^d ($\dot{M}_{\text{acc}}/\dot{M}_{\text{Edd}}$)
3C 401	$2.2^{+3.9}_{-1.4} \times 10^6$	$1.0^{+1.9}_{-0.7} \times 10^{-1}$
Cygnus A	2.7 ± 0.7	...	$1.0^{+0.6}_{-0.4}$	$1.7^{+1.4}_{-1.0} \times 10^7$	$2.1^{+1.8}_{-1.0} \times 10^{-1}$	210^{+630}_{-120}	$3.6^{+5.2}_{-1.2} \times 10^{-3}$
Sersic 159/03	$0.6^{+0.4}_{-0.2}$	$5.0^{+5.3}_{-1.6} \times 10^6$	$1.2^{+1.3}_{-0.4} \times 10^{-1}$	1400^{+8100}_{-1100}	$1.0^{+2.4}_{-0.6} \times 10^{-2}$
A2597	...	0.2 ± 0.1	0.3 ± 0.1	$7.2^{+9.3}_{-3.0} \times 10^5$	$1.1^{+1.4}_{-0.5} \times 10^{-2}$	640^{+4100}_{-540}	$2.6^{+7.1}_{-1.7} \times 10^{-3}$
A4059	...	$0.7^{+1.0}_{-0.4}$	$1.0^{+0.6}_{-0.4}$	$6.1^{+5.2}_{-1.7} \times 10^5$	$1.5^{+1.4}_{-0.6} \times 10^{-2}$	450^{+5830}_{-410}	$1.2^{+4.6}_{-0.9} \times 10^{-3}$

^aBlack hole mass measured using gas kinematics. For Cygnus A, the value of Tadhunter et al. (2003) was adopted, adjusted to our adopted angular diameter distance of 224.2 Mpc. For M87, the average of the values of Harms et al. (1994) and Macchetto et al. (1997) was adopted, adjusted to a distance of 17.9 Mpc. For M84, the value of Maciejewski & Binney (2001) was adopted, adjusted to a distance of 15.2 Mpc.

^bValues have been adjusted by a factor of 0.35 (see text for details).

^cThe change and rate of change in black hole mass were calculated assuming $\epsilon = 0.1$.

^dThe Bondi and Eddington rates were calculated with $M_{\text{BH,meas}}$ when available. If no measured value exists, $M_{\text{BH},\sigma}$ was used, if available, and M_{BH,L_K} if not.

5.2.2 Eddington and Bondi Accretion Rates

It is useful to compare the inferred accretion rates to two theoretical rates, the Eddington and Bondi accretion rates. The Eddington rate is indicative of the maximum likely (steady-state) rate of accretion under the assumption of spherical symmetry, and occurs when the gravitational force acting inward on the accreting material is balanced by the outward pressure of the radiation emitted by the accretion process. For a fully ionized plasma, the Eddington accretion rate is

$$\frac{\dot{M}_{\text{Edd}}}{M_{\odot} \text{ yr}^{-1}} = 2.2\epsilon^{-1} \left(\frac{M_{\text{BH}}}{10^9 M_{\odot}} \right). \quad (5.3)$$

This rate is a function only of the black hole mass (discussed in Section 5.2.3) and the assumed radiative efficiency, ϵ . Table 5.1 lists the Eddington ratios ($\dot{M}_{\text{acc}}/\dot{M}_{\text{Edd}}$) for our sample, calculated assuming $\epsilon = 0.1$.

The Bondi rate (Bondi, 1952) sets the rate of accretion, assuming spherical symmetry, for a black hole with an accreting atmosphere of temperature (T) and density (n_e) as

$$\frac{\dot{M}_{\text{Bondi}}}{M_{\odot} \text{ yr}^{-1}} = 0.012 \times \left(\frac{n_e}{\text{cm}^{-3}} \right) \left(\frac{kT}{\text{keV}} \right)^{-3/2} \left(\frac{M_{\text{BH}}}{10^9 M_{\odot}} \right)^2. \quad (5.4)$$

This accretion occurs within the Bondi radius, inside which the gas comes under the dominating influence of the black hole:

$$\frac{R_{\text{Bondi}}}{\text{kpc}} = 0.031 \times \left(\frac{kT}{\text{keV}} \right)^{-1} \left(\frac{M_{\text{BH}}}{10^9 M_{\odot}} \right). \quad (5.5)$$

The Bondi rate is therefore an estimate of accretion directly from the hot ICM onto the black hole. Table 5.1 lists the Bondi ratios ($\dot{M}_{\text{acc}}/\dot{M}_{\text{Bondi}}$) for our sample, and

Table 5.2 lists the properties used in the calculation of the Bondi rates. In calculating the Bondi rate, we use the modeled temperature and density from *Chandra* spectra, extracted from a central region that contains ~ 3000 counts after the exclusion of any non-thermal point sources. However, the size of the central region is not sufficiently small to resolve the Bondi radius of any system in our sample; therefore, the true temperature and density of the ICM at the Bondi radius could be lower and higher, respectively, than we have measured, resulting in an underestimate of the Bondi rate. We discuss this effect further in Section 5.4.

5.2.3 Black Hole Masses

Calculation of both the Eddington and Bondi rates requires estimates of the black hole mass. Of the systems in our sample, only three (Cygnus A, M84, and M87) have direct mass measurements (see Table 5.1). For the remaining systems, we use the bulge properties of the host galaxy as proxies for the black hole mass. As discussed earlier, the black hole's mass scales with the large-scale properties of the host galaxy such as bulge velocity dispersion and luminosity. The most well-studied relation between the black hole mass and the properties of the host galaxy is the $M_{\text{BH}} - \sigma$ relation, which relates M_{BH} to the stellar velocity dispersion (σ) of the galaxy's bulge as

$$\log \left(\frac{M_{\text{BH},\sigma}}{M_{\odot}} \right) = \alpha + \beta \log \left(\frac{\sigma}{\sigma_0} \right), \quad (5.6)$$

Table 5.2. Central ICM Properties Used in the Bondi Calculations.

System	kT (keV)	n_e (cm $^{-3}$)	a (kpc)	R_{Bondi} (kpc)
A85	$2.1^{+0.1}_{-0.2}$	$0.107^{+0.009}_{-0.008}$	5.8	0.017
A133	$1.8^{+0.1}_{-0.1}$	$0.048^{+0.004}_{-0.005}$	8.0	0.012
A262	$0.86^{+0.01}_{-0.01}$	$0.065^{+0.008}_{-0.007}$	3.4	0.013
Perseus	$4.4^{+0.5}_{-0.4}$	$0.150^{+0.005}_{-0.005}$	8.6	0.004
2A 0335+096	$1.4^{+0.1}_{-0.1}$	$0.056^{+0.003}_{-0.002}$	5.1	0.012
A478	$2.7^{+0.3}_{-0.3}$	$0.20^{+0.01}_{-0.02}$	5.3	0.010
MS 0735.6+7421	$3.2^{+0.2}_{-0.2}$	$0.067^{+0.002}_{-0.003}$	23.8	0.007
PKS 0745-191	$2.6^{+0.4}_{-0.4}$	$0.14^{+0.01}_{-0.01}$	11.2	0.013
Hydra A	$2.6^{+0.8}_{-0.5}$	$0.15^{+0.01}_{-0.02}$	4.7	0.011
Zw 2701	$3.3^{+0.3}_{-0.3}$	$0.024^{+0.002}_{-0.002}$	37.6	0.006
Zw 3146	$3.1^{+0.3}_{-0.2}$	$0.177^{+0.007}_{-0.007}$	15.0	0.027
M84	$0.57^{+0.01}_{-0.01}$	$0.105^{+0.007}_{-0.007}$	0.9	0.020
M87	$0.94^{+0.02}_{-0.02}$	$0.191^{+0.009}_{-0.009}$	1.0	0.110
Centaurus	$0.77^{+0.01}_{-0.01}$	$0.23^{+0.01}_{-0.01}$	1.3	0.015
HCG 62	$0.67^{+0.01}_{-0.01}$	$0.057^{+0.007}_{-0.005}$	2.1	0.010
A1795	$2.7^{+0.6}_{-0.4}$	$0.067^{+0.005}_{-0.005}$	9.5	0.007
A1835	$4.0^{+0.3}_{-0.3}$	$0.110^{+0.003}_{-0.003}$	27.2	0.015
PKS 1404-267	$1.3^{+0.1}_{-0.1}$	$0.046^{+0.002}_{-0.002}$	8.5	0.009
A2029	$2.9^{+0.3}_{-0.2}$	$0.37^{+0.04}_{-0.03}$	2.2	0.022
A2052	$0.71^{+0.04}_{-0.08}$	$0.017^{+0.002}_{-0.002}$	5.5	0.017
MKW 3S	$2.8^{+0.8}_{-0.5}$	$0.028^{+0.006}_{-0.009}$	7.8	0.003
A2199	$2.2^{+0.2}_{-0.1}$	$0.099^{+0.005}_{-0.005}$	4.4	0.010
Hercules A	$2.0^{+0.2}_{-0.2}$	$0.0111^{+0.0006}_{-0.0005}$	67.0	0.012
3C 388	$3.0^{+0.2}_{-0.2}$	$0.0069^{+0.0004}_{-0.0004}$	55.6	0.016
Cygnus A	$5.2^{+0.5}_{-0.6}$	$0.132^{+0.009}_{-0.008}$	5.3	0.017
Sersic 159/03	$1.8^{+0.2}_{-0.1}$	$0.056^{+0.004}_{-0.004}$	12.2	0.010
A2597	$1.6^{+0.2}_{-0.2}$	$0.073^{+0.005}_{-0.005}$	11.0	0.006
A4059	$2.1^{+0.1}_{-0.1}$	$0.022^{+0.001}_{-0.001}$	10.6	0.010

where α , β , and σ_0 are constants. The values of these constants vary somewhat from study to study (for a discussion, see Tremaine et al., 2002). For the purposes of our calculations, we adopt the values of Tremaine et al. (2002), namely $\alpha = 8.13 \pm 0.06$, $\beta = 4.02 \pm 0.32$, and $\sigma_0 = 200 \text{ km s}^{-1}$.

In deriving this relation, Tremaine et al. (2002) use as σ the mean stellar velocity dispersion within a slit aperture of length $2r_e$ and width $1'' - 2''$ (denoted by σ_1). Unfortunately, most of our sample lacks dispersions measured in this aperture. Instead, central velocity dispersions (generally measured within an aperture of $r \sim 2''$) are more common. Central dispersions (denoted by σ_c) were taken from the HyperLeda Database.¹ Measurements of σ_c exist for 15 of the 33 galaxies in our sample (listed in Table 2.1). When more than one measurement exists, we use the weighted average of all available measurements. We have estimated the magnitude of the error resulting from our use of σ_c instead of σ_1 using the relations given in Jorgensen et al. (1995) and Tremaine et al. (2002) and find for the 8 systems in our sample with measurements of both r_e and σ_c that $M_{\text{BH},\sigma}$ increases on average by 10% after the correction, much less than the typical formal uncertainties in $M_{\text{BH},\sigma}$. Since we lack measurements of r_e for some systems and the correction is small, we ignore the aperture correction and use simply σ_c in our calculation of $M_{\text{BH},\sigma}$.

For the 18 systems without a measurement of velocity dispersion, we calculate the black hole mass from the total K -band luminosity of the bulge (L_K) using the relation of Marconi & Hunt (2003) for their group 1 black holes (those with secure mass determinations):

$$\log \left(\frac{M_{\text{BH},L_K}}{M_\odot} \right) = A + B \left[\log \left(\frac{L_K}{L_\odot} \right) - 10.9 \right], \quad (5.7)$$

¹ Available at <http://leda.univ-lyon.fr/>

where $A = 8.21 \pm 0.07$ and $B = 1.13 \pm 0.12$. Apparent K -band magnitudes were taken from the Two Micron All Sky Survey (2MASS) catalog.² The apparent magnitudes were corrected for Galactic extinction with the values of Schlegel et al. (1998) and corrected for redshift (K -corrected) and evolution using the corrections of Poggianti (1997). Lastly, the magnitudes were converted to absolute magnitudes using our assumed cosmology and the redshifts listed in Table 2.1.

We note that there is a systematic offset between the masses calculated by the two methods for the 15 systems that have measurements of both central velocity dispersion and total K -band magnitude. Masses calculated from the total K -band luminosity are on average 2.9 ± 1.6 times greater. We checked this result using total R -band magnitudes from the HyperLeda database (see Section 5.2.3) and the $M_{\text{BH}} - M_R$ relation of McLure & Dunlop (2004) and find a similar systematic offset [$M_{\text{BH},M_R} = (3.3 \pm 2.4) \times M_{\text{BH},\sigma}$]. Bettoni et al. (2003) find a similar but smaller offset in a sample of radio galaxies and attribute it to systematically low values of σ . Since our values of σ are typically weighted averages of several values from a number of different sources, it is unlikely that they would be systematically low across our entire sample.

We do not understand the origin of the offset in our data, but note that the galaxies in our sample are mostly large cDs, with extended stellar envelopes that may bias their total magnitudes with respect to normal ellipticals (e.g., Schombert, 1986);

²See <http://www.ipac.caltech.edu/2mass>.

however, [Fujita & Reiprich \(2004\)](#) do not find evidence of such an offset in a similar sample of CDGs. It is also possible that the $M_{\text{BH}} - \sigma$ relation breaks down at high masses (see e.g., [Shields et al., 2006](#)); however, there is little evidence to support this hypothesis at this time. [Marconi & Hunt \(2003\)](#) find evidence of a significant correlation between M_{BH} and the bulge effective radius, with the result that $M_{\text{BH},\sigma}$ may be too low for large bulges. For typical values of the effective radius for galaxies in our sample ($r_e \sim 10$ kpc), the magnitude of this effect is sufficient to account for the offset we see. However, [Marconi & Hunt \(2003\)](#) note that this correlation is weak, and further investigation is required to confirm its existence. For the purposes of calculating the Eddington and Bondi rates, we adjust the black hole masses inferred from the K -band luminosities by a factor of 0.35. The black hole masses inferred by both methods are listed in Table 5.1.

Bulge Masses

Lastly, to estimate the impact of star formation on the mass of the galaxy's bulge, we have estimated the mass of the bulge as

$$M_{\text{bulge}} = L_{\text{bulge}} \left(\frac{M}{L} \right)_{\text{bulge}}. \quad (5.8)$$

We use the total R -band luminosity of the galaxy for the bulge luminosity, L_{bulge} . Total apparent magnitudes were taken when available from the catalog of [Prugniel & Heraudeau \(1998\)](#) and otherwise from the LEDA database (both databases are available through HyperLeda). In cases in which the R -band magnitudes were un-

available, we used the total B -band magnitudes, if available, and converted these to R -band magnitudes using $\langle (B - R)_0 \rangle = 1.44 \pm 0.17$ (the average corrected color of our sample). The apparent magnitudes were corrected and converted to absolute magnitudes in the same way as the K -band magnitudes (see Section 5.2.2). For the R -band mass-to-light ratio of the bulge, we adopt $(M/L)_{\text{bulge}} = 6.3 (M/L)_{\odot}$, the average found by Fisher et al. (1995), after adjusting to our cosmology. The derived absolute magnitudes and bulge masses are listed in Table 2.1.

5.3 Comparing Black Hole and Bulge Growth

X-ray cavities provide a strong lower limit on the energy of the AGN outburst, independent of accretion disk radiation models and photon conversion efficiencies. Therefore they provide a robust means of estimating the minimum mass accreted onto the black hole. These properties allow us to investigate the relationship between the black hole's growth and the bulge's local (small-scale) growth in the same systems in a unique and detailed fashion that has not been possible before.

Figure 5.1 shows the black hole growth rate versus the bulge growth rate (traced by star formation) for the systems in our sample with reliable star formation rate estimates. We plot as dashed lines the time derivative of the present-day Magorrian relation, as found by Häring & Rix (2004): $\dot{M}_{\text{BH}} = 1.4 \times 10^{-3} \dot{M}_{\text{bulge}}$. In terms of our derived quantities, this relation becomes $(1 - \epsilon)P_{\text{cav}}/(\epsilon c^2) = 1.4 \times 10^{-3} SFR$.

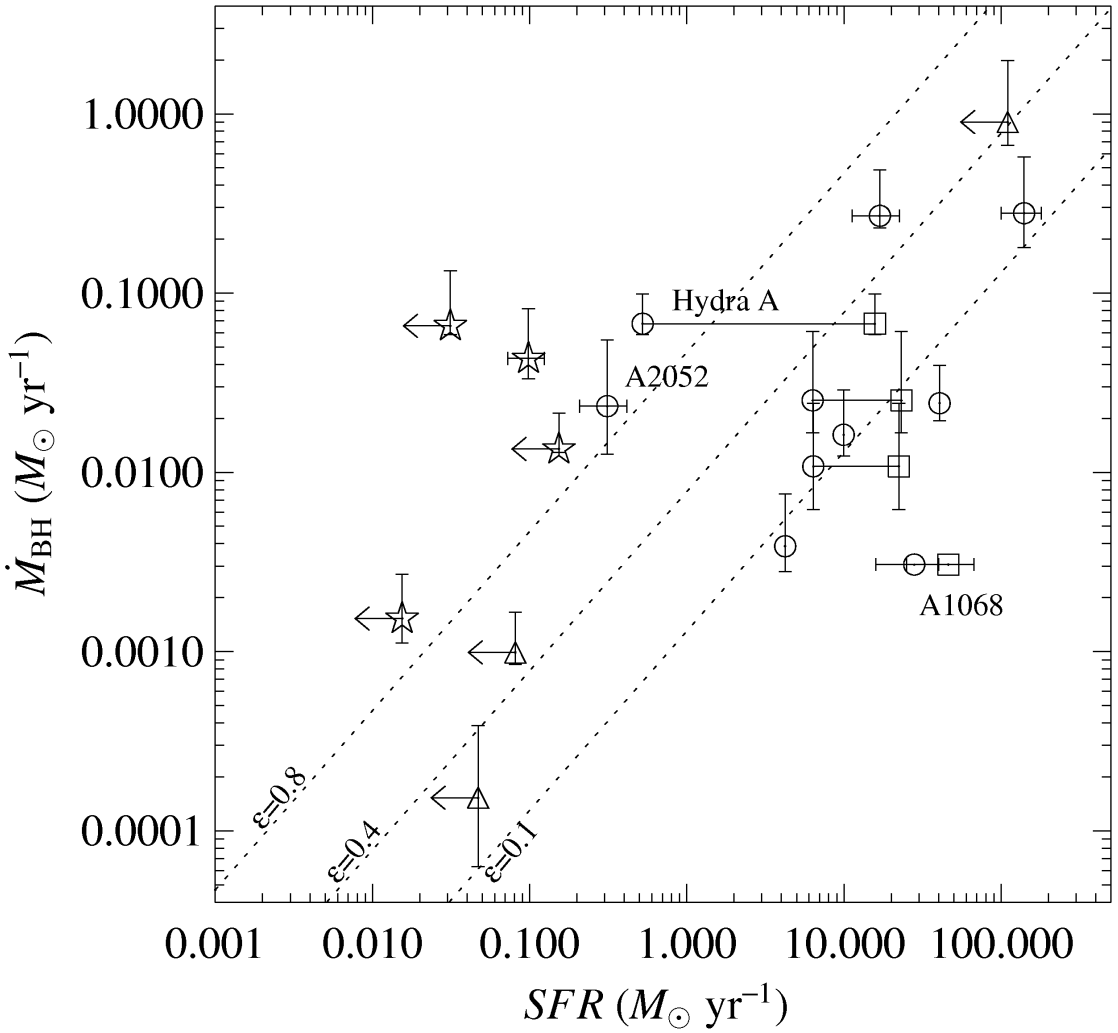


Figure 5.1: Black hole growth rate versus star formation rate. The diagonal lines represent $\dot{M}_{\text{BH}} = 1.4 \times 10^{-3} SFR$ (see text for details) for different values of ϵ . The symbols are the same as those in Figure 4.1.

There is a trend, with large scatter, between the bulge and black hole growth rates, centered approximately on the Magorrian slope (assuming accretion efficiencies of $\epsilon \sim 0.1\text{-}0.4$).

As discussed in Section 5.2.1, the upper limit on the efficiency with which the rest mass energy of the accreting material is converted to outburst energy varies between

0.06 and 0.4. Therefore, under the assumption that star formation traces all of the bulge’s growth, consistency with general relativity and the slope of the Magorrian relation requires that all objects with estimates of the *total* star formation rate fall below the $\epsilon = 0.4$ line in Figure 5.1.

This requirement is clearly violated in a number of objects. For example, the black holes in both Hydra A and A2052 are growing faster than strict adherence to the Magorrian relation would predict, whereas the bulge of A1068 is growing too fast (note, however, that no cavities were detected in A1068’s atmosphere; therefore, there is large uncertainty in the rate of growth of A1068’s black hole). While the discrepancy in A1068’s rates may be explained with an extremely low efficiency for the conversion of gravitational binding energy of the accreting material to outburst energy ($\epsilon \sim 0.005$), it is also possible that present-day growth is occurring in spurts, with periods of cooling and star formation (as in A1068) in which the bulge grows quickly with little commensurate black hole growth, while during periods of heating (as in Hydra A) the black hole grows more quickly than the bulge.

The trend in Figure 5.1 may be interpreted as an indication that, in a time-averaged sense, the growth of the bulges and black holes in our sample proceeds roughly along the Magorrian relation. When compared to the bulge masses calculated in Section 4.2 and the black hole masses calculated in Section 5.2.1, the black holes are growing at rates of $\sim 10^{-9} - 10^{-12}$ yr $^{-1}$ and the bulges at rates of $\sim 10^{-11} - 10^{-13}$ yr $^{-1}$. Present-day growth would not move most of the systems significantly off of

the Magorrian relation, even if growth at such rates was constant for the age of the universe.

However, for a number of systems, current growth could produce their present-day black holes in $\lesssim 10^{10}$ yr. The three most extreme cases (MS 0735.6+7421, Zw 2701, and Zw 3146) have growth rates that, if constant over just $\sim 10^9$ yr, would be sufficient to grow their black holes to their current masses. Periodic and powerful outbursts, without commensurate bulge growth (e.g., MS 0735.6+7421), could cause significant departures from the Magorrian relation.

These three systems represent $\sim 10\%$ of our sample, implying a duty cycle in active systems of one such outburst every $\sim 10^8/0.1 = 10^9$ yr (assuming a typical time between outbursts of 10^8 yr). Large outbursts might shut off cooling (and hence fueling) for long periods, making them a relatively rare event (see [Donahue et al., 2006](#)). If the most powerful outbursts are infrequent in the present-day universe, the Magorrian relation must have been established during earlier periods of extreme black hole and bulge growth, as has been postulated by a number of authors (e.g., [Yu & Tremaine, 2002](#); [Binney, 2005](#); [Di Matteo et al., 2005](#); [Churazov et al., 2005](#)) and supported by high-redshift quasar studies (e.g., [McLure & Dunlop, 2004](#)).

Lastly, it is possible that we are missing some fraction of the bulge growth. The CDG is thought to grow through the addition of material by two main processes: cooling of gas out of the ICM (see Section [3.3.1](#)) and merging (cannibalism) of the CDG with other cluster members. The rate of growth from mergers is difficult to

measure. Lauer (1988), through a study of multiple-nucleus CDGs, estimated a cannibalism rate of $L \approx 2L^*$ per 5×10^9 yr. This estimate implies that such growth is significant over the age of the cluster; however, the time scale for this growth is much longer than the cooling and star formation time scales considered here. Therefore, we have neglected mergers and used the star formation rates described in Section 4.2 to set the instantaneous bulge growth rate.

5.4 Accretion Mechanism

To investigate whether the growth of the black hole, or equivalently the energy of its outburst, depends on its mass (inferred assuming bulges come equipped with mature black holes, see Section 5.2.3), we plot in Figure 5.2 the fractional change in the black hole's mass during the outburst ($\Delta M_{\text{BH}}/M_{\text{BH}}$) against its mass. There is no clear indication in Figure 5.2 that the growth of the black hole depends on the black hole mass, at least to the extent that the bulge velocity dispersion or luminosity is a good black hole mass estimator for these systems. For example, systems that differ by a factor of two in inferred black hole mass, such as M84 ($M_{\text{BH}} \sim 4 \times 10^8 M_{\odot}$) and MS 0735.6+7421 ($M_{\text{BH}} \sim 7 \times 10^8 M_{\odot}$), differ in their fractional growth by a factor of $\sim 10^5$. However, uncertainties in the black hole and accreted masses may obscure any underlying correlation.

For a number of objects in our sample, the implied accretion rates necessary to generate the cavities are well above our Bondi accretion rates (by factors of up to

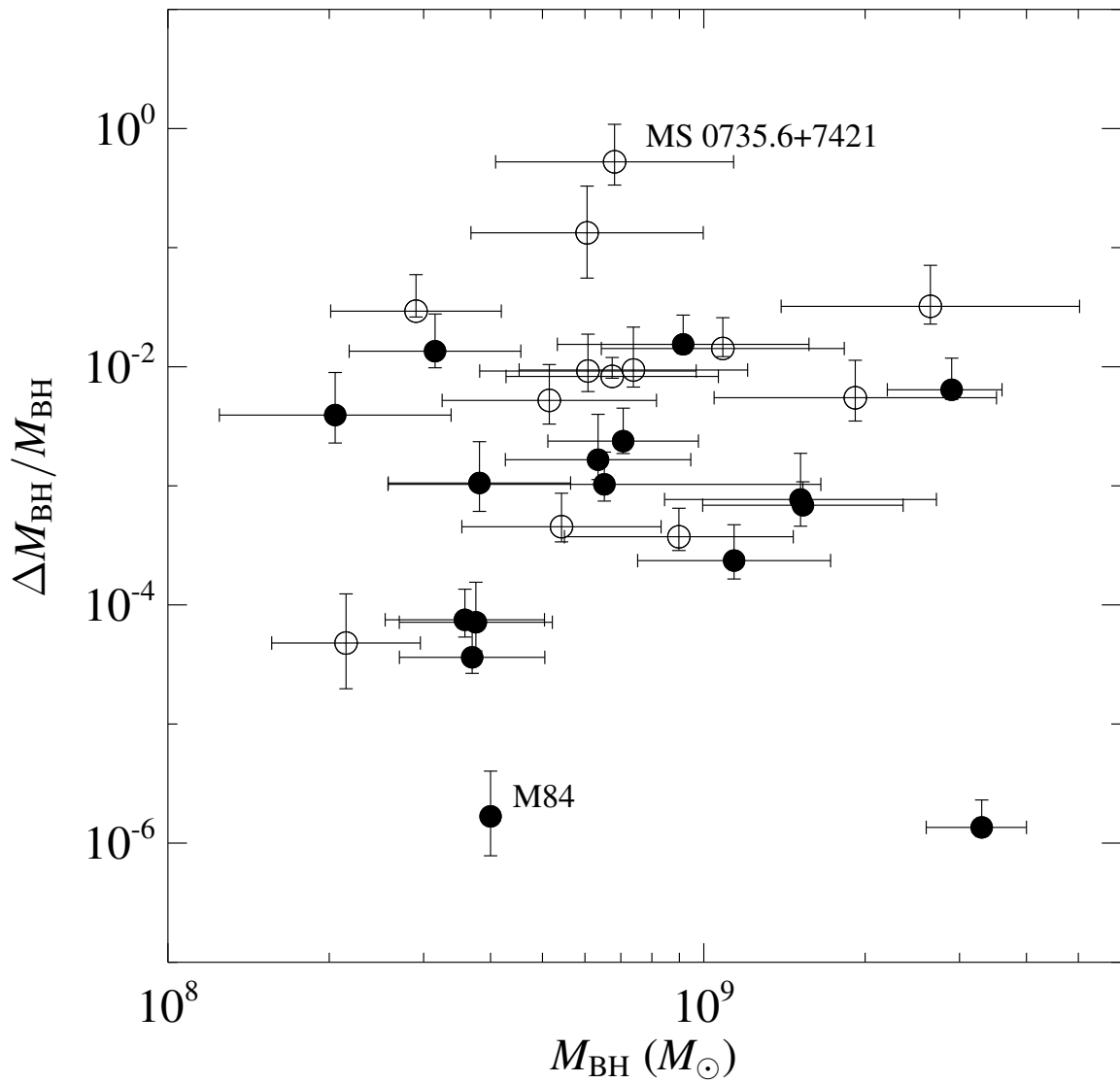


Figure 5.2: The black hole's relative change in mass versus the mass of the black hole, inferred either from gas kinematics or the stellar velocity dispersion (*filled symbols*) or from the K -band luminosity of the host galaxy's bulge (*empty symbols*, corrected by a factor of 0.35).

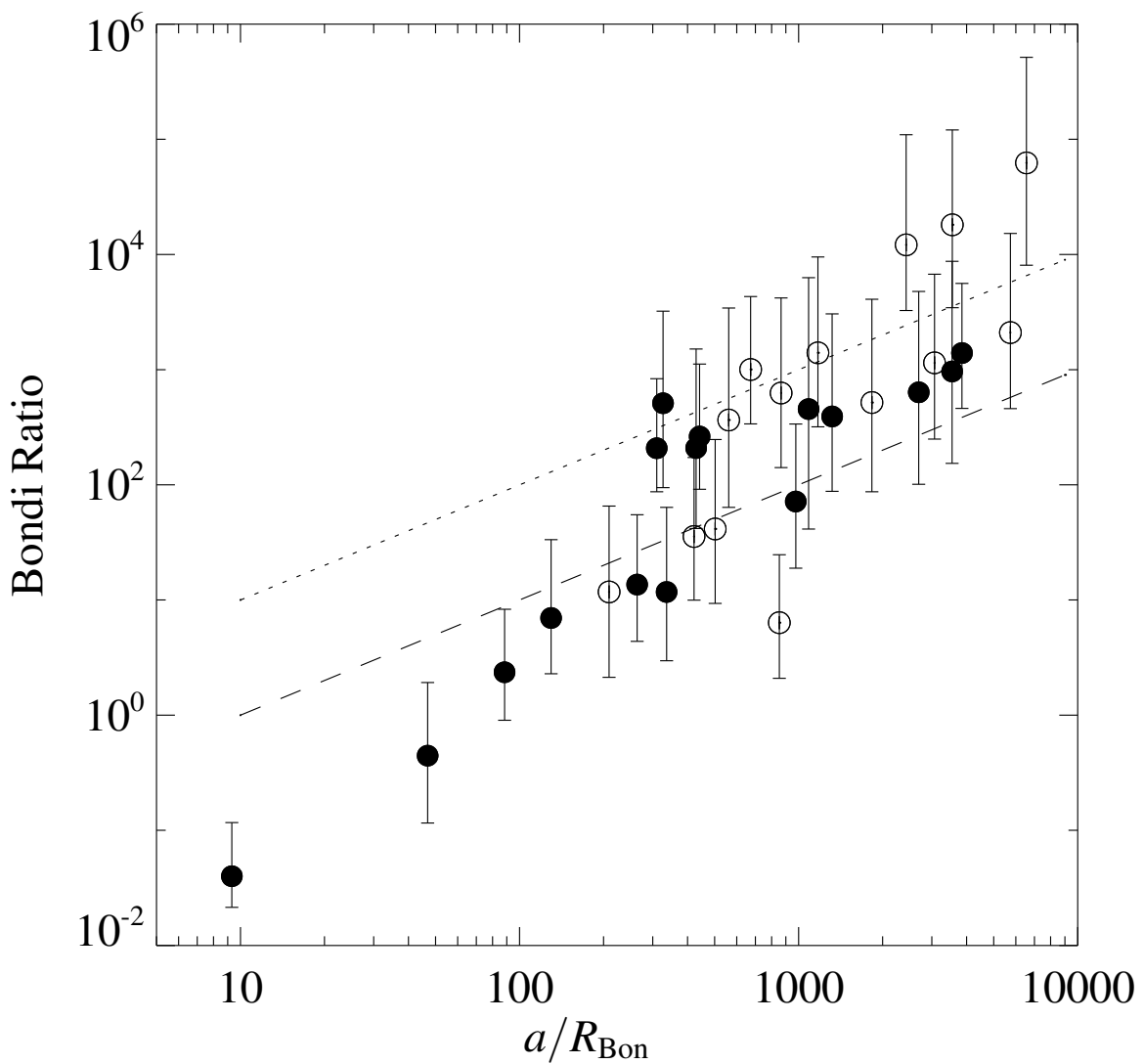


Figure 5.3: Bondi ratio (defined as $\dot{M}_{\text{acc}}/\dot{M}_{\text{Bondi}}$) versus the ratio of the semi-major axis of the central region (within which the Bondi rate was calculated) to the Bondi radius. The symbols are the same as those in Figure 5.2. The lines denote the likely scaling of the measured Bondi ratio with the size of the central region, assuming a true Bondi ratio of 1 at the Bondi radius and a density profile $\rho \propto r^{-1}$, with either a flat core inside $a/R_{\text{Bondi}} = 10$ (*dashed line*) or no core (*dotted line*).

$\sim 5 \times 10^4$, see Table 5.1 and Figure 5.3). Specifically, those systems with the most powerful outbursts appear to have the largest Bondi ratios, as should be expected from the small range in black hole masses. However, as discussed in Section 5.2.2, we do not resolve the Bondi radius. Therefore, our Bondi rates are probably lower than the true values, particularly in higher redshift objects and those observations with a low number of total counts (resulting in a larger central region to obtain ~ 3000 counts).

To illustrate the radial dependence of this correction, we plot in Figure 5.3 the ratio of the accretion to Bondi rate versus the semi-major axis of the central region from which the Bondi rates were calculated, normalized to the Bondi radius. The trend in this figure supports the conclusion that the Bondi radius is not resolved. Overplotted are lines denoting the scaling of the measured Bondi ratio with radius, assuming a true Bondi ratio of unity at the Bondi radius and a density profile that rises as $\rho \propto r^{-1}$ to the Bondi radius (upper line) or flattens inside $a/R_{\text{Bondi}} = 10$ (lower line), as observed in M87 (Di Matteo et al., 2003). Objects near or below these lines could reasonably have ratios of order unity or less and thus be consistent with Bondi accretion. Those significantly above the lines are likely to be accreting in excess of their Bondi rates.

All of the objects in our sample are consistent with Bondi accretion, but only if the density continues to rise as a powerlaw to the Bondi radius. The accretion rates in those objects with the least powerful outbursts (such as M84 and M87) are

generally consistent with Bondi ratios of significantly less than unity. This conclusion is supported by [Allen et al. \(2006\)](#), who find that accretion rates in ellipticals with low-power outbursts are consistent with Bondi accretion.

However, a number of objects (typically those with powerful outbursts, such as MS 0735.6+7421 and Zw 2701) are barely consistent with Bondi accretion and would have difficulty fueling their outbursts through Bondi accretion alone, suggesting some other route for much of the accreting material, such as cold accretion (e.g., the cold feedback mechanism of [Pizzolato & Soker, 2005](#)). Additionally, the Bondi accretion rate assumes spherically symmetric, radial accretion, while real astrophysical flows will have some net angular momentum. An example is M87, which appears to possess a central disk of gas ([Harms et al., 1994](#); [Macchetto et al., 1997](#)); thus, any accreting material would be likely to have significant angular momentum (for a discussion, see [Pizzolato & Soker, 2005](#)). Recent hydrodynamic simulations of accretion flows (e.g., [Proga & Begelman, 2003](#); [Krumholz et al., 2005](#)) find that even small amounts of angular momentum can reduce the accretion rate to well below the Bondi rate.

It is also possible that the Bondi rates (and hence central densities) in these objects were higher at the time of the outburst than they are now. We note however that very high densities imply very short cooling times. At sufficiently high densities, the gas will cool and fall out of the hot phase in which Bondi accretion operates, placing an upper limit on the density appropriate for use in the Bondi calculation (the maximal cooling flow, see [Nulsen & Fabian, 2000](#)). For example, to fuel the outbursts in MS

0735.6+7421 and Zw 2701 by Bondi accretion alone, the accretion rate would need to be very close to the maximal cooling flow value ($\sim 10\%$ of the Eddington rate for these objects, see [Nulsen & Fabian, 2000](#)). However, this constraint is not severe enough to rule out Bondi accretion as a viable accretion mechanism in most of our sample.

5.5 Summary

Using the cavities to infer black hole growth and star formation to infer bulge growth, we find that bulge and black hole growth rates scale roughly with each other in rough accordance with the slope of the Magorrian relation. The large scatter may indicate that growth occurs in spurts, with periods of cooling and star formation interspersed with periods of heating, or that the efficiency of the conversion of the gravitational binding energy of the accreting matter to outburst energy varies across the sample. We find the central supermassive black holes are growing at rates of $\sim 10^{-4} M_{\odot} \text{ yr}^{-1}$ to $\sim 1 M_{\odot} \text{ yr}^{-1}$ (with a median rate of $0.035 M_{\odot} \text{ yr}^{-1}$), which, in most of our sample, are insufficient to account for their present-day masses. However, a number of black holes are growing at rates that are consistent with their formation from scratch in $\sim 10^{10} \text{ yr}$. The extreme cases are those objects experiencing the most powerful outbursts ($P_{\text{cav}} \sim 5 \times 10^{45} \text{ ergs s}^{-1}$, approximately 10% of our sample), which are growing at rates sufficient to assemble their black holes in $\sim 10^9 \text{ yr}$.

Across our sample, the inferred black hole accretion rates are well below their Eddington limits but above their Bondi rates. *Chandra* does not resolve the Bondi radius in these systems, and thus significant Bondi accretion cannot be ruled out. The exceptions are those systems with powerful outbursts, where either direct accretion from the hot ICM is not the principle route of cooling gas or their central properties were very different at the time of the outburst than those of typical nearby CDGs such as M87.

CHAPTER 6

Conclusions

We have presented an analysis of the star formation, ICM, and AGN properties in 61 cooling flows. We demonstrate that AGN outbursts, which are strongly coupled to the ICM through cavities inflated by the AGN’s lobes, can supply enough energy to balance cooling in more than half of our sample and possibly, in a time-averaged sense, in all cooling flows. The black hole growth that must accompany these outbursts is large enough in some cases to make simple Bondi accretion unlikely, though it is still well below Eddington limits. While low-level, net cooling may still proceed, it must do so at much smaller rates than predicted before the advent of high-resolution X-ray data. We show that upper limits on the net cooling rates are consistent with the scenario in which the cooling ICM is the source of material for active star formation, unusual in most ellipticals but present in many CDGs. We demonstrate that excess blue emission in the CDG, indicative of recent star formation, is closely linked to the presence of gas in the ICM with short cooling times ($\lesssim 7 \times 10^8$ yr) or low entropies ($\lesssim 30$ keV cm²) within ~ 20 kpc of the CDG’s core. Lastly, we find that star formation is also more likely to exist in systems whose AGN are currently supplying insufficient energy to balance cooling from the ICM.

In summary, a unified picture of star formation, cooling, and AGN feedback is now emerging, one with applications to the more general problems of galaxy formation and

the truncation of the high end of the luminosity function of galaxies. Both simulations and models of galaxy formation (e.g., Balogh et al., 2001; Sijacki & Springel, 2006; Voit et al., 2005) conclude that AGN heating is required to prevent the overcooling problem in Λ CDM models, in which too many large galaxies are formed. A plausible scenario, supported by our findings, is that AGN regulate the cooling of gas in the cores of cooling flows, preventing most of the ICM from cooling but allowing some net condensation that feeds both star formation and black hole growth, possibly in an intermittent manner, along the Magorrian relation.

Bibliography

Abramowicz, M. A., Chen, X., Kato, S., Lasota, J.-P., & Regev, O. 1995, ApJ, 438, L37

Allen, S. W. 1995, MNRAS, 276, 947

Allen, S. W., Dunn, R. J. H., Fabian, A. C., Taylor, G. B., & Reynolds, C. S. 2006, MNRAS, 372, 21

Allen, S. W., Schmidt, R. W., Ebeling, H., Fabian, A. C., & van Speybroeck, L. 2004, MNRAS, 353, 457

Anders, E., & Grevesse, N. 1989, Geochim. Cosmochim. Acta, 53, 197

Balogh, M. L., Pearce, F. R., Bower, R. G., & Kay, S. T. 2001, MNRAS, 326, 1228

Bauer, F. E., Fabian, A. C., Sanders, J. S., Allen, S. W., & Johnstone, R. M. 2005, MNRAS, 359, 1481

Bettoni, D., Falomo, R., Fasano, G., & Govoni, F. 2003, A&A, 399, 869

Binney, J. 2005, Royal Society of London Philosophical Transactions Series A, 363, 739

Binney, J., & Tabor, G. 1995, MNRAS, 276, 663

Binney, J., & Tremaine, S. 1987, Galactic dynamics (Princeton, NJ, Princeton University Press)

- Bîrzan, L., Rafferty, D. A., McNamara, B. R., Wise, M. W., & Nulsen, P. E. J. 2004, ApJ, 607, 800
- Blanton, E. L., Sarazin, C. L., & McNamara, B. R. 2003, ApJ, 585, 227
- Blanton, E. L., Sarazin, C. L., McNamara, B. R., & Clarke, T. E. 2004, ApJ, 612, 817
- Blanton, E. L., Sarazin, C. L., McNamara, B. R., & Wise, M. W. 2001, ApJ, 558, L15
- Boehringer, H., & Hensler, G. 1989, A&A, 215, 147
- Boehringer, H., Voges, W., Fabian, A. C., Edge, A. C., & Neumann, D. M. 1993, MNRAS, 264, L25
- Bondi, H. 1952, MNRAS, 112, 195
- Bregman, J. N., Fabian, A. C., Miller, E. D., & Irwin, J. A. 2006, ApJ, 642, 746
- Bregman, J. N., Miller, E. D., Athey, A. E., & Irwin, J. A. 2005, ApJ, 635, 1031
- Cardiel, N., Gorgas, J., & Aragon-Salamanca, A. 1995, MNRAS, 277, 502
—. 1998, MNRAS, 298, 977
- Carollo, C. M., Danziger, I. J., & Buson, L. 1993, MNRAS, 265, 553
- Chatzikos, M., Sarazin, C. L., & Kempner, J. C. 2006, ApJ, 643, 751

- Choi, Y.-Y., Reynolds, C. S., Heinz, S., Rosenberg, J. L., Perlman, E. S., & Yang, J. 2004, ApJ, 606, 185
- Churazov, E., Brüggen, M., Kaiser, C. R., Böhringer, H., & Forman, W. 2001, ApJ, 554, 261
- Churazov, E., Sazonov, S., Sunyaev, R., Forman, W., Jones, C., & Böhringer, H. 2005, MNRAS, 363, L91
- Churazov, E., Sunyaev, R., Forman, W., & Böhringer, H. 2002, MNRAS, 332, 729
- Clarke, T. E., Blanton, E. L., & Sarazin, C. L. 2004, ApJ, 616, 178
- Clarke, T. E., Sarazin, C. L., Blanton, E. L., Neumann, D. M., & Kassim, N. E. 2005, ApJ, 625, 748
- Crawford, C. S., Allen, S. W., Ebeling, H., Edge, A. C., & Fabian, A. C. 1999, MNRAS, 306, 857
- Dahle, H., Kaiser, N., Irgens, R. J., Lilje, P. B., & Maddox, S. J. 2002, ApJS, 139, 313
- David, L. P., Nulsen, P. E. J., McNamara, B. R., Forman, W., Jones, C., Ponman, T., Robertson, B., & Wise, M. 2001, ApJ, 557, 546
- Di Matteo, T., Allen, S. W., Fabian, A. C., Wilson, A. S., & Young, A. J. 2003, ApJ, 582, 133

- Di Matteo, T., Springel, V., & Hernquist, L. 2005, *Nature*, 433, 604
- Dickey, J. M., & Lockman, F. J. 1990, *ARA&A*, 28, 215
- Donahue, M., Horner, D. J., Cavagnolo, K. W., & Voit, G. M. 2006, *ApJ*, 643, 730
- Dubinski, J. 1994, *ApJ*, 431, 617
- Dunn, R. J. H., & Fabian, A. C. 2006, *MNRAS*, 373, 959
- Durret, F., Lima Neto, G. B., & Forman, W. 2005, *A&A*, 432, 809
- Edgar, R. J., & Chevalier, R. A. 1986, *ApJ*, 310, L27
- Edge, A. C. 2001, *MNRAS*, 328, 762
- Edge, A. C., Stewart, G. C., Fabian, A. C., & Arnaud, K. A. 1990, *MNRAS*, 245, 559
- Edwards, L. O. V., Hudson, M. J., Balogh, M. L., & Smith, R. J. 2007, *MNRAS*, 502
- Elvis, M., Maccacaro, T., Wilson, A. S., Ward, M. J., Penston, M. V., Fosbury, R. A. E., & Perola, G. C. 1978, *MNRAS*, 183, 129
- Enßlin, T. A., & Heinz, S. 2002, *A&A*, 384, L27
- Ettori, S., Fabian, A. C., Allen, S. W., & Johnstone, R. M. 2002, *MNRAS*, 331, 635
- Fabian, A. C. 1994, *ARA&A*, 32, 277

- Fabian, A. C., Celotti, A., Blundell, K. M., Kassim, N. E., & Perley, R. A. 2002a, MNRAS, 331, 369
- Fabian, A. C., Mushotzky, R. F., Nulsen, P. E. J., & Peterson, J. R. 2001, MNRAS, 321, L20
- Fabian, A. C., Sanders, J. S., Allen, S. W., Crawford, C. S., Iwasawa, K., Johnstone, R. M., Schmidt, R. W., & Taylor, G. B. 2003a, MNRAS, 344, L43
- Fabian, A. C., Sanders, J. S., Crawford, C. S., Conselice, C. J., Gallagher, J. S., & Wyse, R. F. G. 2003b, MNRAS, 344, L48
- Fabian, A. C., Sanders, J. S., Ettori, S., Taylor, G. B., Allen, S. W., Crawford, C. S., Iwasawa, K., Johnstone, R. M., & Ogle, P. M. 2000, MNRAS, 318, L65
- Fabian, A. C., Sanders, J. S., Taylor, G. B., & Allen, S. W. 2005, MNRAS, 360, L20
- Fabian, A. C., Sanders, J. S., Taylor, G. B., Allen, S. W., Crawford, C. S., Johnstone, R. M., & Iwasawa, K. 2006, MNRAS, 366, 417
- Fabian, A. C., Voigt, L. M., & Morris, R. G. 2002b, MNRAS, 335, L71
- Ferrarese, L., & Merritt, D. 2000, ApJ, 539, L9
- Ferreras, I., Lisker, T., Carollo, C. M., Lilly, S. J., & Mobasher, B. 2005, ApJ, 635, 243
- Finoguenov, A., & Jones, C. 2001, ApJ, 547, L107

Fisher, D., Illingworth, G., & Franx, M. 1995, ApJ, 438, 539

Forman, W., Churazov, E., Jones, C., Markevitch, M., Nulsen, P., Vikhlinin, A., Begelman, M., Boehringer, H., Eilek, J., Heinz, S., Kraft, R., Owen, F., & Pahre, M. 2006, astro-ph/0604583

Forman, W., Nulsen, P., Heinz, S., Owen, F., Eilek, J., Vikhlinin, A., Markevitch, M., Kraft, R., Churazov, E., & Jones, C. 2005, ApJ, 635, 894

Frank, J., King, A., & Raine, D. J. 2002, Accretion Power in Astrophysics: Third Edition (Cambridge, UK, Cambridge University Press, 2002)

Franx, M., Illingworth, G., & Heckman, T. 1989, AJ, 98, 538

Fujita, Y., & Reiprich, T. H. 2004, ApJ, 612, 797

Fujita, Y., Sarazin, C. L., Kempner, J. C., Rudnick, L., Slee, O. B., Roy, A. L., Andernach, H., & Ehle, M. 2002, ApJ, 575, 764

Fujita, Y., Sarazin, C. L., Reiprich, T. H., Andernach, H., Ehle, M., Murgia, M., Rudnick, L., & Slee, O. B. 2004, ApJ, 616, 157

Gebhardt, K., Bender, R., Bower, G., Dressler, A., Faber, S. M., Filippenko, A. V., Green, R., Grillmair, C., Ho, L. C., Kormendy, J., Lauer, T. R., Magorrian, J., Pinkney, J., Richstone, D., & Tremaine, S. 2000, ApJ, 539, L13

Gitti, M., McNamara, B. R., Nulsen, P. E. J., & Wise, M. W. 2007, ApJ, 660, 1118

- Goudfrooij, P., Hansen, L., Jorgensen, H. E., Norgaard-Nielsen, H. U., de Jong, T., & van den Hoek, L. B. 1994, A&AS, 104, 179
- Häring, N., & Rix, H.-W. 2004, ApJ, 604, L89
- Harms, R. J., Ford, H. C., Tsvetanov, Z. I., Hartig, G. F., Dressel, L. L., Kriss, G. A., Bohlin, R., Davidsen, A. F., Margon, B., & Kochhar, A. K. 1994, ApJ, 435, L35
- Heckman, T. M. 1981, ApJ, 250, L59
- Heinz, S., Choi, Y.-Y., Reynolds, C. S., & Begelman, M. C. 2002, ApJ, 569, L79
- Hicks, A. K., & Mushotzky, R. 2005, ApJ, 635, L9
- Hicks, A. K., Wise, M. W., Houck, J. C., & Canizares, C. R. 2002, ApJ, 580, 763
- Hu, E. M., Cowie, L. L., & Wang, Z. 1985, ApJS, 59, 447
- Iwasawa, K., Fabian, A. C., Allen, S. W., & Ettori, S. 2001, MNRAS, 328, L5
- Jedrzejewski, R. I. 1987, MNRAS, 226, 747
- Jeltema, T. E., Canizares, C. R., Bautz, M. W., & Buote, D. A. 2005, ApJ, 624, 606
- Johnstone, R. M., Allen, S. W., Fabian, A. C., & Sanders, J. S. 2002, MNRAS, 336, 299
- Johnstone, R. M., Fabian, A. C., Morris, R. G., & Taylor, G. B. 2005, MNRAS, 356, 237

- Johnstone, R. M., Fabian, A. C., & Nulsen, P. E. J. 1987, MNRAS, 224, 75
- Jones, C., Forman, W., Vikhlinin, A., Markevitch, M., David, L., Warmflash, A., Murray, S., & Nulsen, P. E. J. 2002, ApJ, 567, L115
- Jorgensen, I., Franx, M., & Kjaergaard, P. 1995, MNRAS, 276, 1341
- Kaastra, J. S., Tamura, T., Peterson, J. R., Bleeker, J. A. M., Ferrigno, C., Kahn, S. M., Paerels, F. B. S., Piffaretti, R., Branduardi-Raymont, G., & Böhringer, H. 2004, A&A, 413, 415
- Kempner, J. C., Sarazin, C. L., & Ricker, P. M. 2002, ApJ, 579, 236
- Kennicutt, Jr., R. C. 1998, ARA&A, 36, 189
- Kino, M., & Kawakatu, N. 2005, MNRAS, 364, 659
- Kobayashi, C., & Arimoto, N. 1999, ApJ, 527, 573
- Koekemoer, A. M., O'Dea, C. P., Sarazin, C. L., McNamara, B. R., Donahue, M., Voit, G. M., Baum, S. A., & Gallimore, J. F. 1999, ApJ, 525, 621
- Koekemoer, A. M., O'Dea, C. P., Sarazin, C. L., McNamara, B. R., Donahue, M., Voit, M., Baum, S. A., & Gallimore, J. F. 2002, New Astronomy Review, 46, 149
- Kraft, R. P., Azcona, J., Forman, W. R., Hardcastle, M. J., Jones, C., & Murray, S. S. 2006, ApJ, 639, 753
- Krumholz, M. R., McKee, C. F., & Klein, R. I. 2005, ApJ, 618, 757

- Laine, S., van der Marel, R. P., Lauer, T. R., Postman, M., O'Dea, C. P., & Owen, F. N. 2003, AJ, 125, 478
- Landolt, A. U. 1992, AJ, 104, 340
- Lauer, T. R. 1988, ApJ, 325, 49
- Leahy, J. P., & Gizani, N. A. B. 2001, ApJ, 555, 709
- Lecavelier des Etangs, A., Gopal-Krishna, & Durret, F. 2004, A&A, 421, 503
- Levan, A. J., Tanvir, N. R., Fruchter, A. S., Rol, E., Fynbo, J. P. U., Hjorth, J., Williams, G., Bergeron, E., Bersier, D., Bremer, M., Grav, T., Jakobsson, P., Nilsson, K., Olszewski, E., Priddey, R. S., Rafferty, D., & Rhoads, J. 2006, ApJ, 648, L9
- Liedahl, D. A., Osterheld, A. L., & Goldstein, W. H. 1995, ApJ, 438, L115
- Lloyd-Davies, E. J., Ponman, T. J., & Cannon, D. B. 2000, MNRAS, 315, 689
- Macchetto, F., Marconi, A., Axon, D. J., Capetti, A., Sparks, W., & Crane, P. 1997, ApJ, 489, 579
- Maciejewski, W., & Binney, J. 2001, MNRAS, 323, 831
- Magorrian, J., Tremaine, S., Richstone, D., Bender, R., Bower, G., Dressler, A., Faber, S. M., Gebhardt, K., Green, R., Grillmair, C., Kormendy, J., & Lauer, T. 1998, AJ, 115, 2285

- Marconi, A., & Hunt, L. K. 2003, ApJ, 589, L21
- Martinez, J., & Iglewicz, I. 1981, Biometrika, 68, 331
- Mazzotta, P., Brunetti, G., Giacintucci, S., Venturi, T., & Bardelli, S. 2004, Journal of Korean Astronomical Society, 37, 381
- Mazzotta, P., Edge, A. C., & Markevitch, M. 2003, ApJ, 596, 190
- Mazzotta, P., Kaastra, J. S., Paerels, F. B., Ferrigno, C., Colafrancesco, S., Mewe, R., & Forman, W. R. 2002, ApJ, 567, L37
- McLure, R. J., & Dunlop, J. S. 2004, MNRAS, 352, 1390
- McNamara, B. R. 1995, ApJ, 443, 77
- McNamara, B. R. 1997, in Astronomical Society of the Pacific Conference Series, Vol. 115, Galactic Cluster Cooling Flows, ed. N. Soker, 109
- McNamara, B. R. 2004, in The Riddle of Cooling Flows in Galaxies and Clusters of galaxies, ed. T. Reiprich, J. Kempner, & N. Soker, 177
- McNamara, B. R., Jannuzi, B. T., Elston, R., Sarazin, C. L., & Wise, M. 1996a, ApJ, 469, 66
- McNamara, B. R., Jannuzi, B. T., Sarazin, C. L., Elston, R., & Wise, M. 1999, ApJ, 518, 167
- McNamara, B. R., & Nulsen, P. E. J. 2007, ARA&A, 45, 117

- McNamara, B. R., Nulsen, P. E. J., Wise, M. W., Rafferty, D. A., Carilli, C., Sarazin, C. L., & Blanton, E. L. 2005, *Nature*, 433, 45
- McNamara, B. R., & O'Connell, R. W. 1989, *AJ*, 98, 2018
- . 1992, *ApJ*, 393, 579
- . 1993, *AJ*, 105, 417
- McNamara, B. R., Rafferty, D. A., Bîrzan, L., Steiner, J., Wise, M. W., Nulsen, P. E. J., Carilli, C. L., Ryan, R., & Sharma, M. 2006, *ApJ*, 648, 164
- McNamara, B. R., Wise, M., Nulsen, P. E. J., David, L. P., Sarazin, C. L., Bautz, M., Markevitch, M., Vikhlinin, A., Forman, W. R., Jones, C., & Harris, D. E. 2000, *ApJ*, 534, L135
- McNamara, B. R., Wise, M., Sarazin, C. L., Jannuzzi, B. T., & Elston, R. 1996b, *ApJ*, 466, L9
- McNamara, B. R., Wise, M. W., & Murray, S. S. 2004, *ApJ*, 601, 173
- McNamara, B. R., Wise, M. W., Nulsen, P. E. J., David, L. P., Carilli, C. L., Sarazin, C. L., O'Dea, C. P., Houck, J., Donahue, M., Baum, S., Voit, M., O'Connell, R. W., & Koekemoer, A. 2001, *ApJ*, 562, L149
- Morris, R. G., & Fabian, A. C. 2005, *MNRAS*, 358, 585
- Narayan, R., & Yi, I. 1994, *ApJ*, 428, L13

- Nulsen, P. E. J., David, L. P., McNamara, B. R., Jones, C., Forman, W. R., & Wise, M. 2002, ApJ, 568, 163
- Nulsen, P. E. J., & Fabian, A. C. 2000, MNRAS, 311, 346
- Nulsen, P. E. J., Hambrick, D. C., McNamara, B. R., Rafferty, D., Birzan, L., Wise, M. W., & David, L. P. 2005a, ApJ, 625, L9
- Nulsen, P. E. J., McNamara, B. R., Wise, M. W., & David, L. P. 2005b, ApJ, 628, 629
- O'Dea, C. P., Baum, S. A., Mack, J., Koekemoer, A. M., & Laor, A. 2004, ApJ, 612, 131
- Oegerle, W. R., Cowie, L., Davidsen, A., Hu, E., Hutchings, J., Murphy, E., Sembach, K., & Woodgate, B. 2001, ApJ, 560, 187
- Patel, P., Maddox, S., Pearce, F. R., Aragón-Salamanca, A., & Conway, E. 2006, MNRAS, 370, 851
- Pedlar, A., Ghataure, H. S., Davies, R. D., Harrison, B. A., Perley, R., Crane, P. C., & Unger, S. W. 1990, MNRAS, 246, 477
- Peletier, R. F., Davies, R. L., Illingworth, G. D., Davis, L. E., & Cawson, M. 1990, AJ, 100, 1091
- Peres, C. B., Fabian, A. C., Edge, A. C., Allen, S. W., Johnstone, R. M., & White, D. A. 1998, MNRAS, 298, 416

- Peterson, J. R., Kahn, S. M., Paerels, F. B. S., Kaastra, J. S., Tamura, T., Bleeker, J. A. M., Ferrigno, C., & Jernigan, J. G. 2003, ApJ, 590, 207
- Pinkney, J., Holtzman, J., Garasi, C., Watson, A. M., Gallagher, III, J. S., Ballester, G. E., Burrows, C. J., Casertano, S., Clarke, J. T., Crisp, D., Evans, R. W., Griffiths, R. E., Hester, J. J., Hoessel, J. G., Mould, J. R., Scowen, P. A., Stapelfeldt, K. R., Trauger, J. T., & Westphal, J. A. 1996, ApJ, 468, L13
- Pizzolato, F., & Soker, N. 2005, ApJ, 632, 821
- Poggianti, B. M. 1997, A&AS, 122, 399
- Proga, D., & Begelman, M. C. 2003, ApJ, 592, 767
- Prugniel, P., & Heraudeau, P. 1998, A&AS, 128, 299
- Quilis, V., Bower, R. G., & Balogh, M. L. 2001, MNRAS, 328, 1091
- Rafferty, D. A., McNamara, B. R., Nulsen, P. E. J., & Wise, M. W. 2006, ApJ, 652, 216
- Rees, M. J., Phinney, E. S., Begelman, M. C., & Blandford, R. D. 1982, Nature, 295, 17
- Reynolds, C. S., Brenneman, L. W., & Stocke, J. T. 2005, MNRAS, 357, 381
- Reynolds, C. S., Heinz, S., & Begelman, M. C. 2002, MNRAS, 332, 271
- Romanishin, W. 1987, ApJ, 323, L113

Romanishin, W., & Hintzen, P. 1988, ApJ, 324, L17

Rosner, R., & Tucker, W. H. 1989, ApJ, 338, 761

Rowan-Robinson, M., Mann, R. G., Oliver, S. J., Efstathiou, A., Eaton, N., Goldschmidt, P., Mobasher, B., Serjeant, S. B. G., Sumner, T. J., Danese, L., Elbaz, D., Franceschini, A., Egami, E., Kontizas, M., Lawrence, A., McMahon, R., Norgaard-Nielsen, H. U., Perez-Fournon, I., & Gonzalez-Serrano, J. I. 1997, MNRAS, 289, 490

Sanders, J. S., & Fabian, A. C. 2002, MNRAS, 331, 273

Sanders, J. S., Fabian, A. C., & Dunn, R. J. H. 2005, MNRAS, 360, 133

Sanderson, A. J. R., Finoguenov, A., & Mohr, J. J. 2005, ApJ, 630, 191

Schindler, S., Castillo-Morales, A., De Filippis, E., Schwope, A., & Wambsganss, J. 2001, A&A, 376, L27

Schlegel, D. J., Finkbeiner, D. P., & Davis, M. 1998, ApJ, 500, 525

Schmidt, R. W., Allen, S. W., & Fabian, A. C. 2001, MNRAS, 327, 1057

Schmidt, R. W., Fabian, A. C., & Sanders, J. S. 2002, MNRAS, 337, 71

Schombert, J. M. 1986, ApJS, 60, 603

Shields, G. A., Menezes, K. L., Massart, C. A., & Vanden Bout, P. 2006, ApJ, 641,

- Sijacki, D., & Springel, V. 2006, MNRAS, 366, 397
- Silva, D. R., & Wise, M. W. 1996, ApJ, 457, L15
- Smith, D. A., Wilson, A. S., Arnaud, K. A., Terashima, Y., & Young, A. J. 2002, ApJ, 565, 195
- Smith, E. P., Bohlin, R. C., Bothun, G. D., O'Connell, R. W., Roberts, M. S., Neff, S. G., Smith, A. M., & Stecher, T. P. 1997, ApJ, 478, 516
- Smith, E. P., O'Connell, R. W., Bohlin, R. C., Cheng, K.-P., Cornett, R. H., Hill, J. K., Hill, R. S., Hintzen, P., Landsman, W. B., Neff, S. G., Roberts, M. S., Smith, A. M., & Stecher, T. P. 1992, ApJ, 395, L49
- Soker, N. 2003, MNRAS, 342, 463
- . 2006, New Astronomy, 12, 38
- Soker, N., Blanton, E. L., & Sarazin, C. L. 2004, A&A, 422, 445
- Soker, N., White, III, R. E., David, L. P., & McNamara, B. R. 2001, ApJ, 549, 832
- Sun, M., Jones, C., Murray, S. S., Allen, S. W., Fabian, A. C., & Edge, A. C. 2003, ApJ, 587, 619
- Tadhunter, C., Marconi, A., Axon, D., Wills, K., Robinson, T. G., & Jackson, N. 2003, MNRAS, 342, 861

- Tadhunter, C. N., Morganti, R., di Serego-Alighieri, S., Fosbury, R. A. E., & Danziger, I. J. 1993, MNRAS, 263, 999
- Tamura, N., & Ohta, K. 2000, AJ, 120, 533
- Tremaine, S., Gebhardt, K., Bender, R., Bower, G., Dressler, A., Faber, S. M., Filippenko, A. V., Green, R., Grillmair, C., Ho, L. C., Kormendy, J., Lauer, T. R., Magorrian, J., Pinkney, J., & Richstone, D. 2002, ApJ, 574, 740
- Vader, J. P., Vigroux, L., Lachieze-Rey, M., & Souviron, J. 1988, A&A, 203, 217
- Voigt, L. M., & Fabian, A. C. 2004, MNRAS, 347, 1130
- Voigt, L. M., Schmidt, R. W., Fabian, A. C., Allen, S. W., & Johnstone, R. M. 2002, MNRAS, 335, L7
- Voit, G. M., Balogh, M. L., Bower, R. G., Lacey, C. G., & Bryan, G. L. 2003, ApJ, 593, 272
- Voit, G. M., & Donahue, M. 2005, ApJ, 634, 955
- Voit, G. M., Kay, S. T., & Bryan, G. L. 2005, MNRAS, 364, 909
- Vrtilek, J. M., Grego, L., David, L. P., Ponman, T. J., Forman, W., Jones, C., & Harris, D. E. 2002, APS Meeting Abstracts, 17107
- Wills, K. A., Tadhunter, C. N., Robinson, T. G., & Morganti, R. 2002, MNRAS, 333,

Wilson, A. S., Smith, D. A., & Young, A. J. 2006, ApJ, 644, L9

Wilson, A. S., Young, A. J., & Smith, D. A. 2003, in Astronomical Society of the Pacific Conference Series, Vol. 290, Active Galactic Nuclei: From Central Engine to Host Galaxy, ed. S. Collin, F. Combes, & I. Shlosman, 141

Wise, M. W., McNamara, B. R., & Murray, S. S. 2004, ApJ, 601, 184

Wise, M. W., McNamara, B. R., Nulsen, P. E. J., Houck, J. C., & David, L. P. 2007, ApJ, 659, 1153

Young, A. J., Wilson, A. S., & Mundell, C. G. 2002, ApJ, 579, 560

Yu, Q., & Tremaine, S. 2002, MNRAS, 335, 965

Zakamska, N. L., & Narayan, R. 2003, ApJ, 582, 162

APPENDIX A

Images

In the following figures, we show false-color optical images of each CDG in the sample for which optical data were taken. The I -band image is shown in red, R -band in green, and U -band in blue (when either the R - or I -band image only was available, it was used for both red and green colors). The bands have been matched for seeing. A logarithmic scaling has been used, with a single bias and contrast across all three bands. North is up and East to the left in all images, and the bar in each image shows the scale.

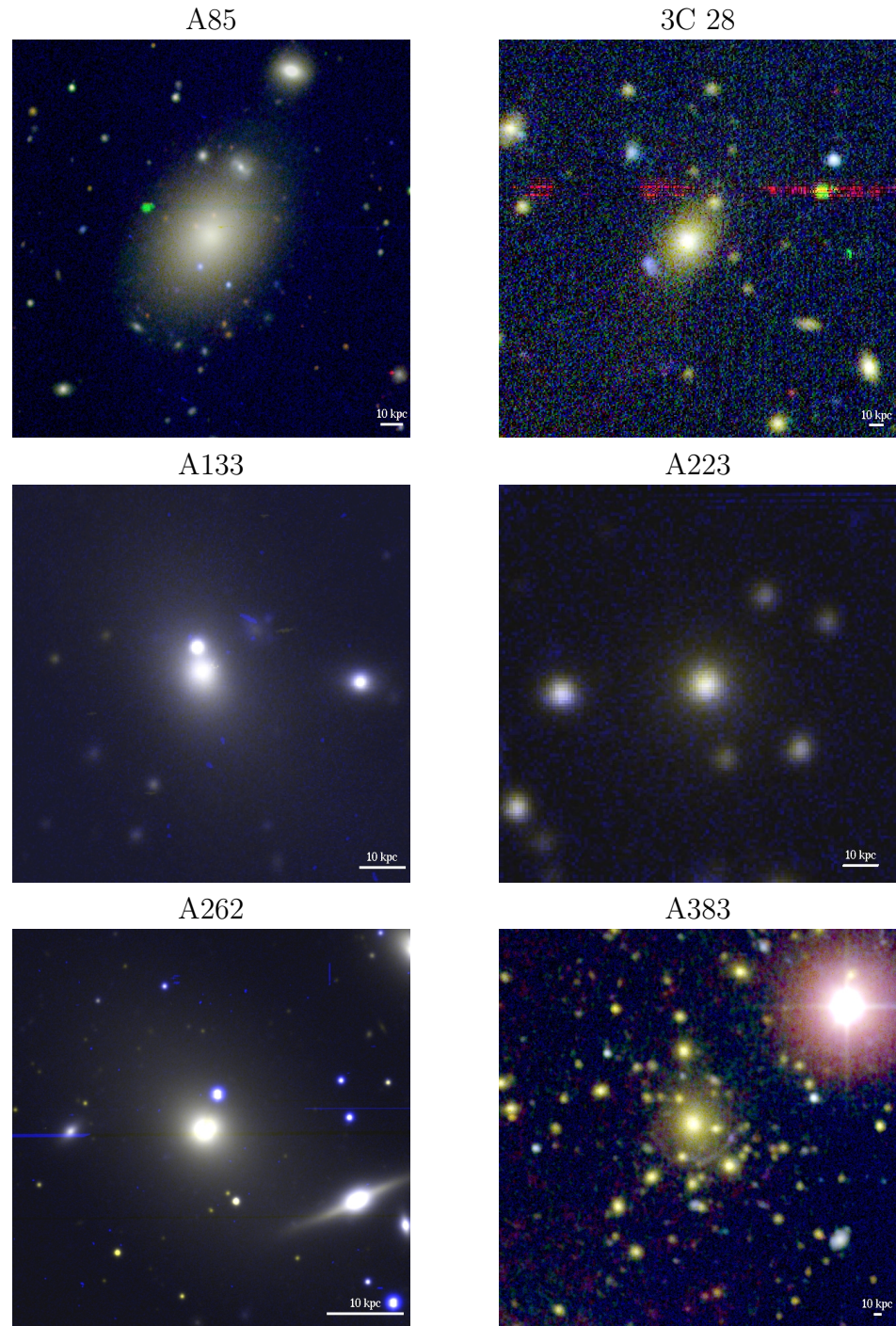


Figure A.1: Optical images of the CDGs in the sample.

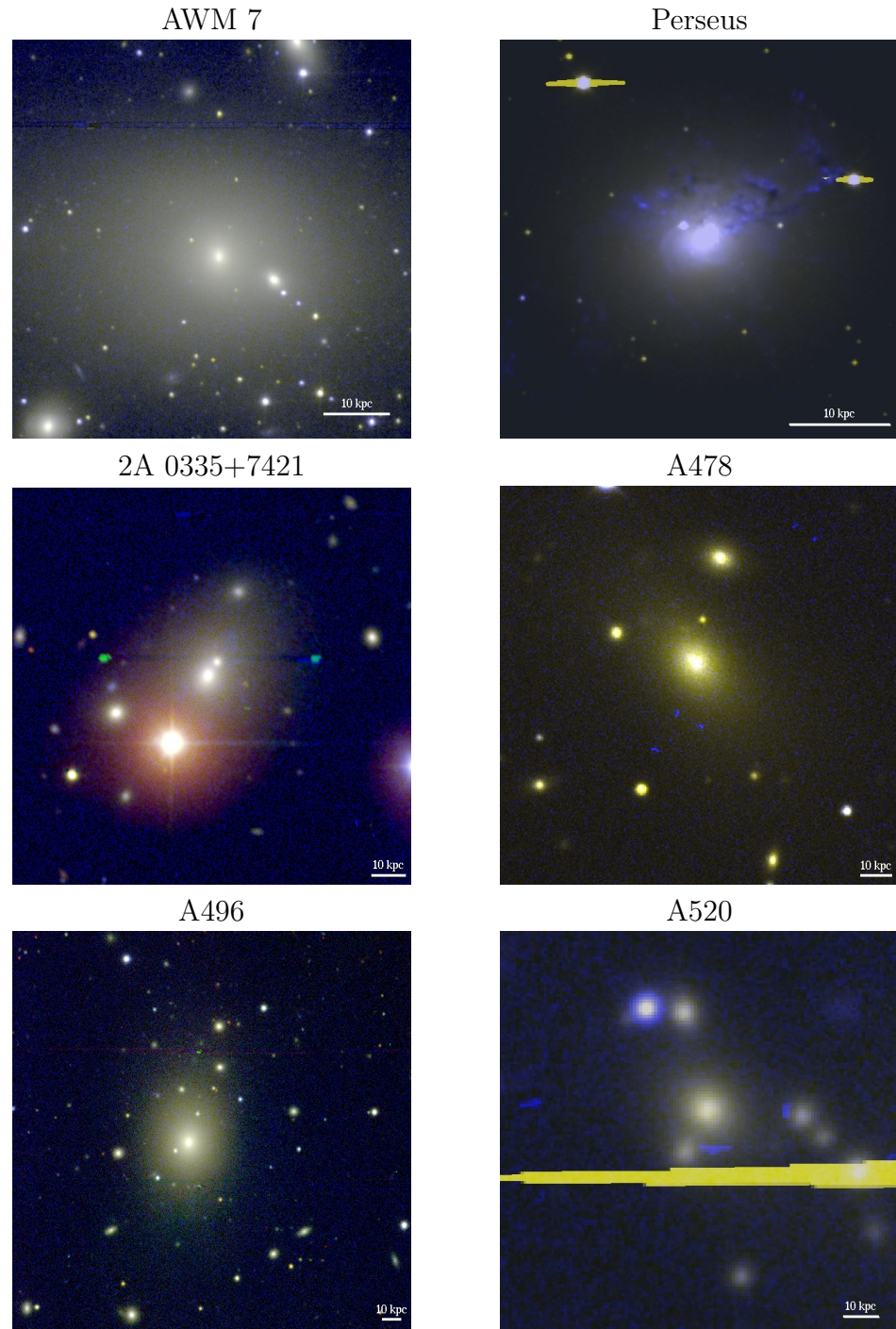


Figure A.2: Optical images of the CDGs in the sample — continued.

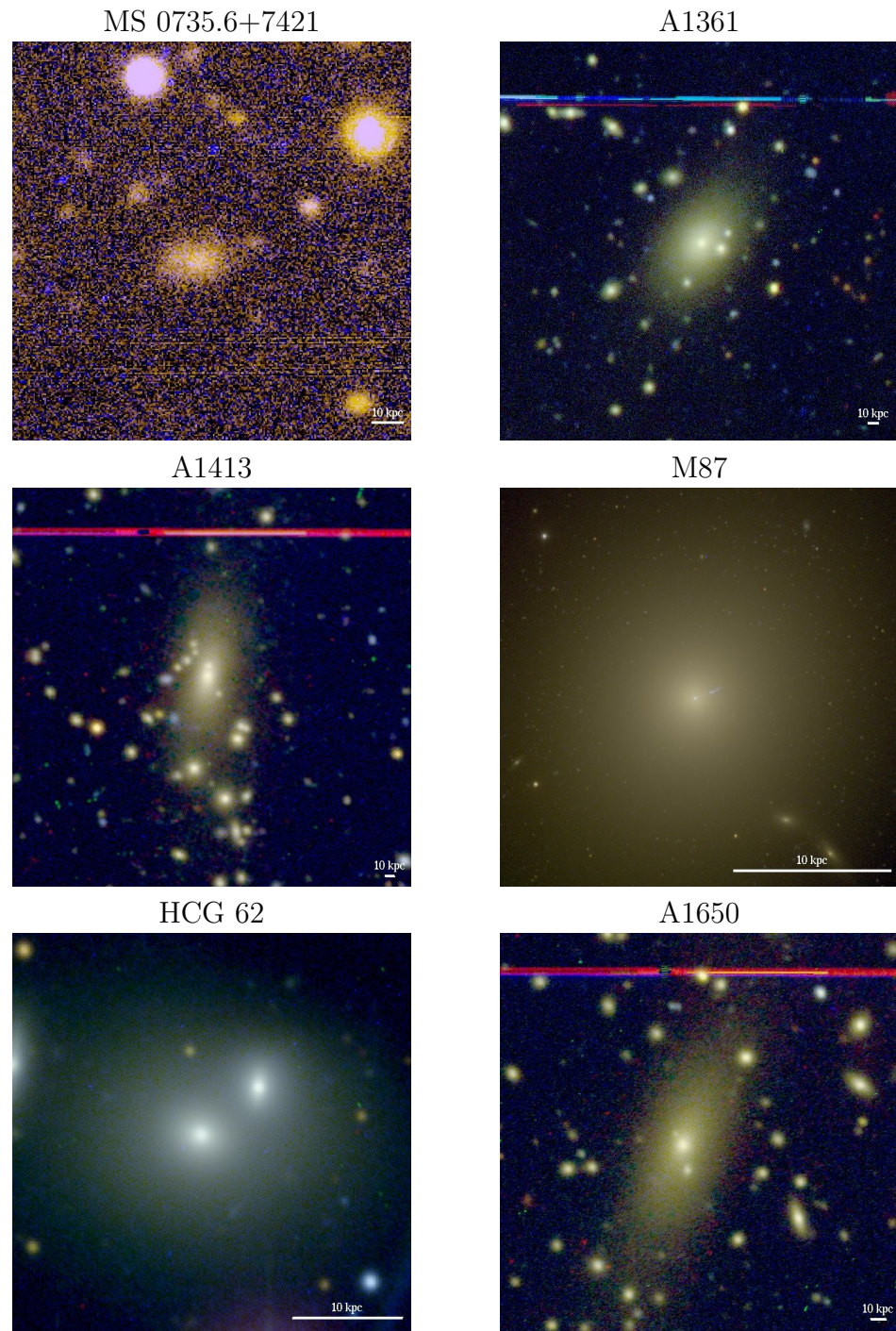


Figure A.3: Optical images of the CDGs in the sample — continued.

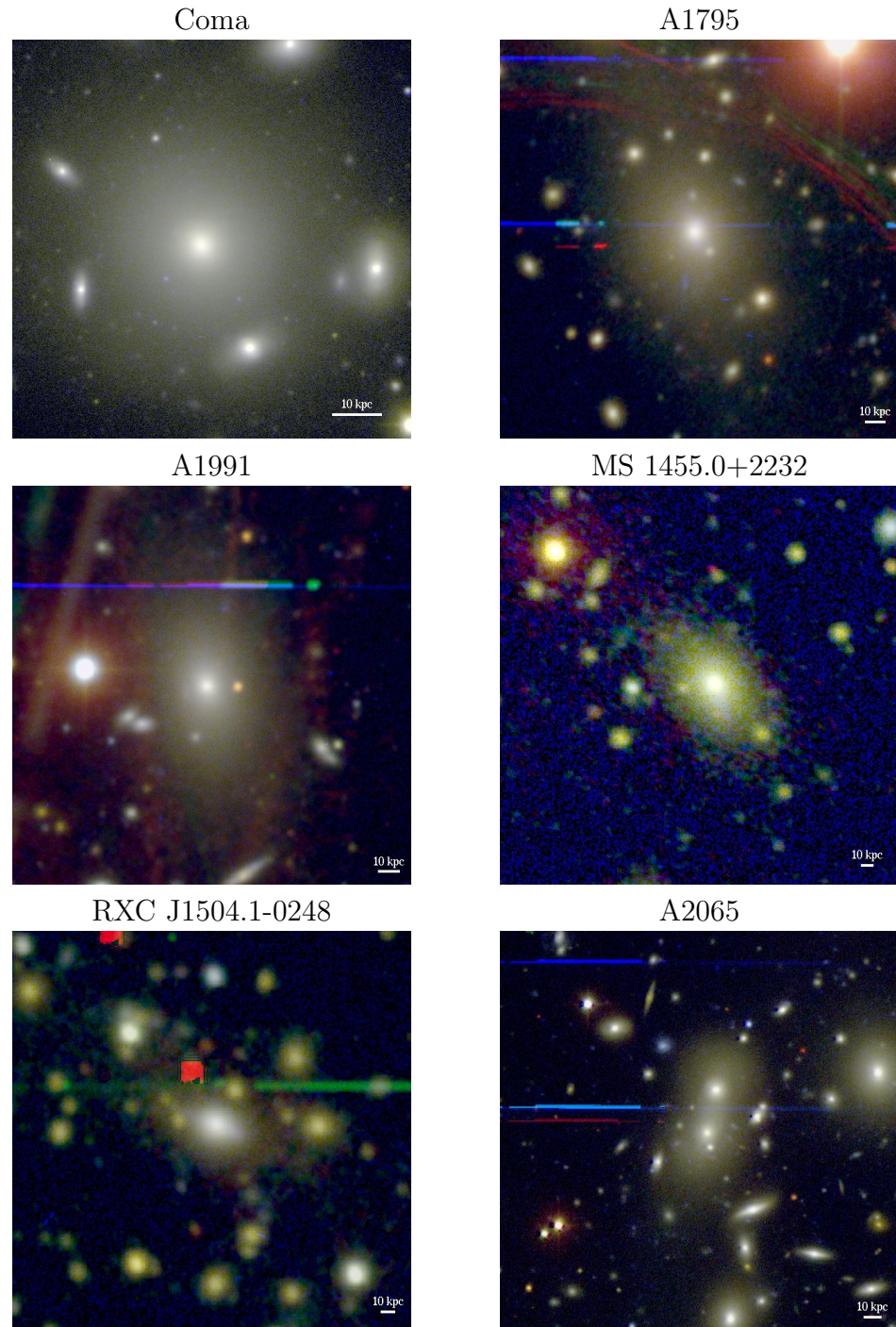


Figure A.4: Optical images of the CDGs in the sample — continued.

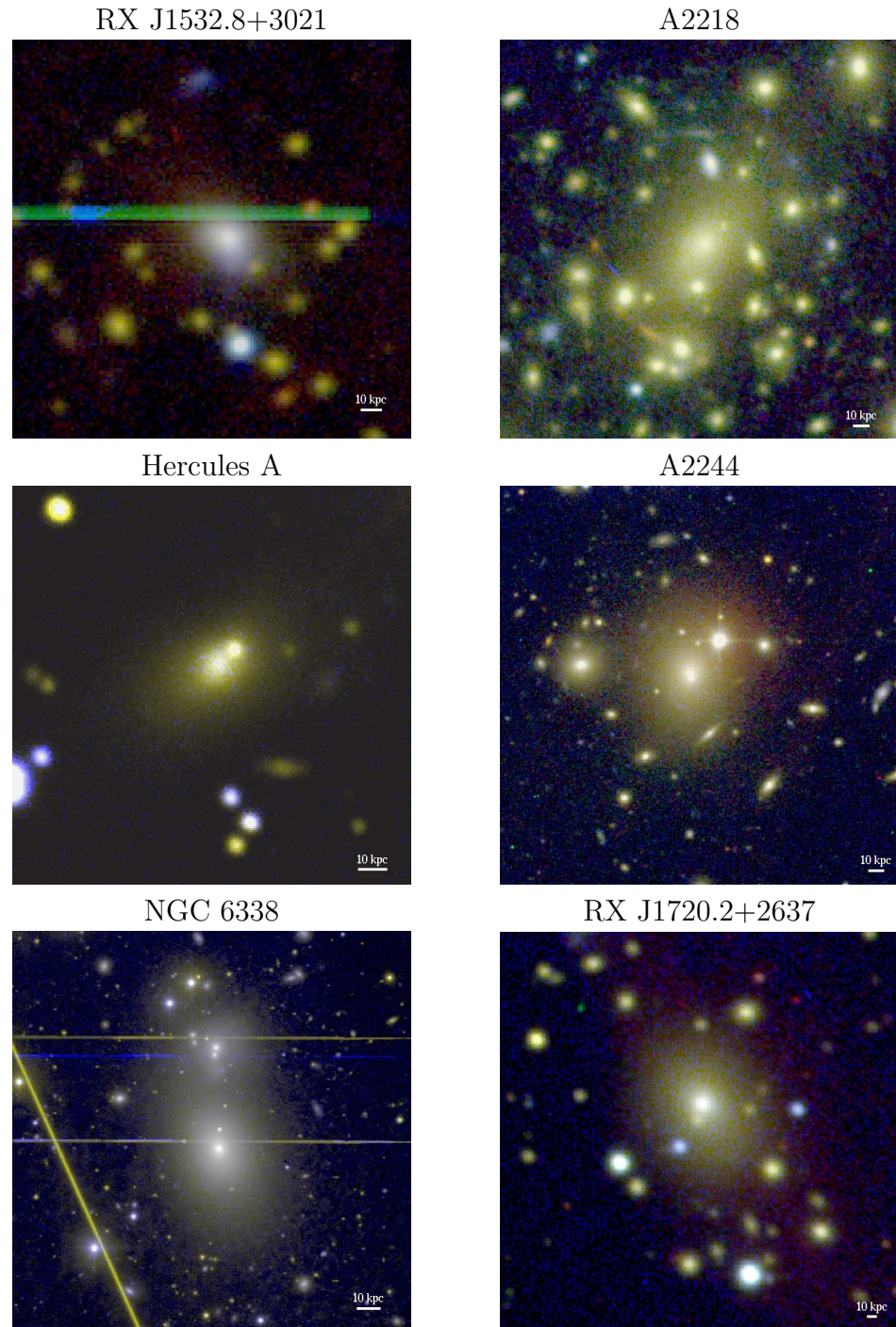


Figure A.5: Optical images of the CDGs in the sample — continued.

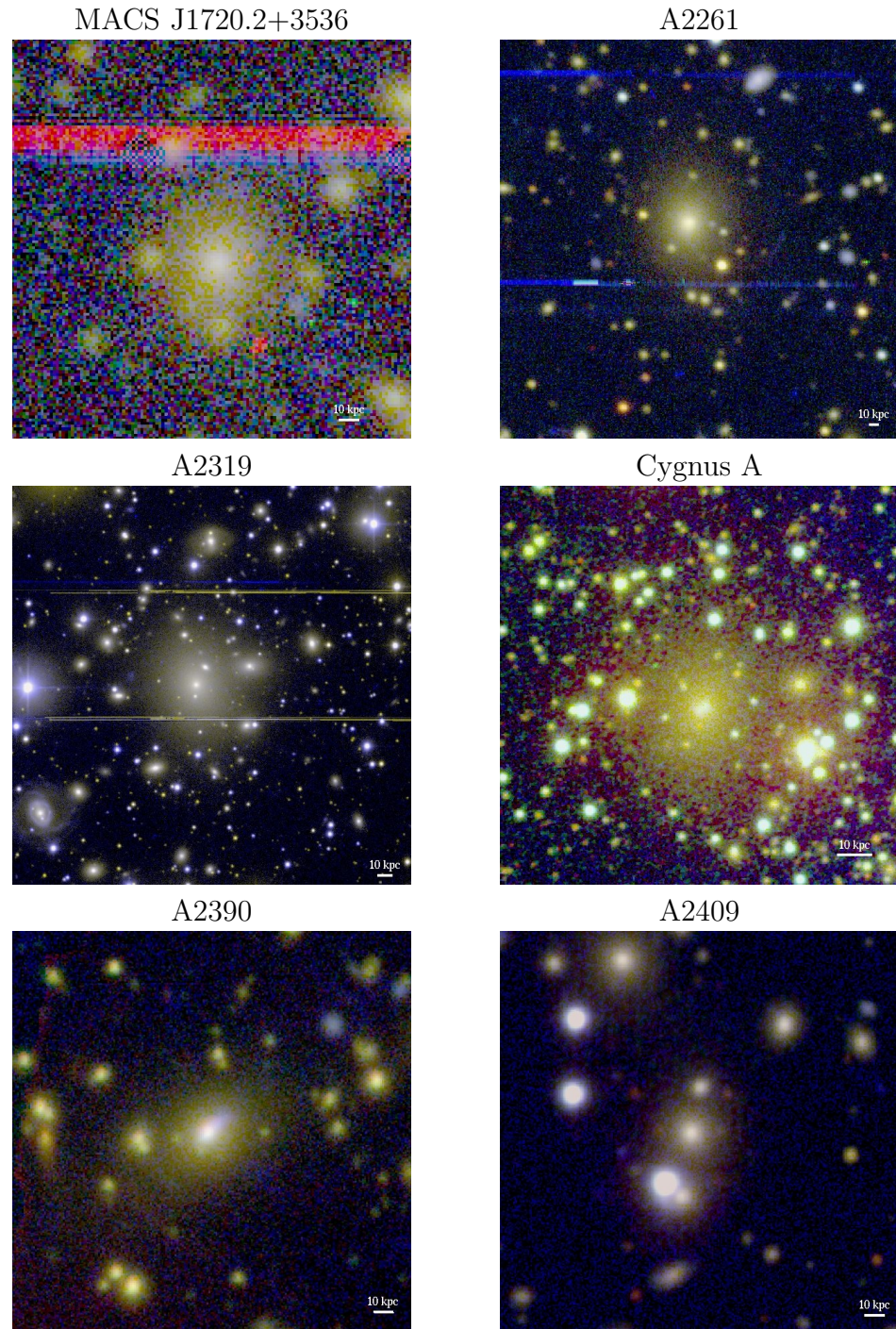


Figure A.6: Optical images of the CDGs in the sample — continued.

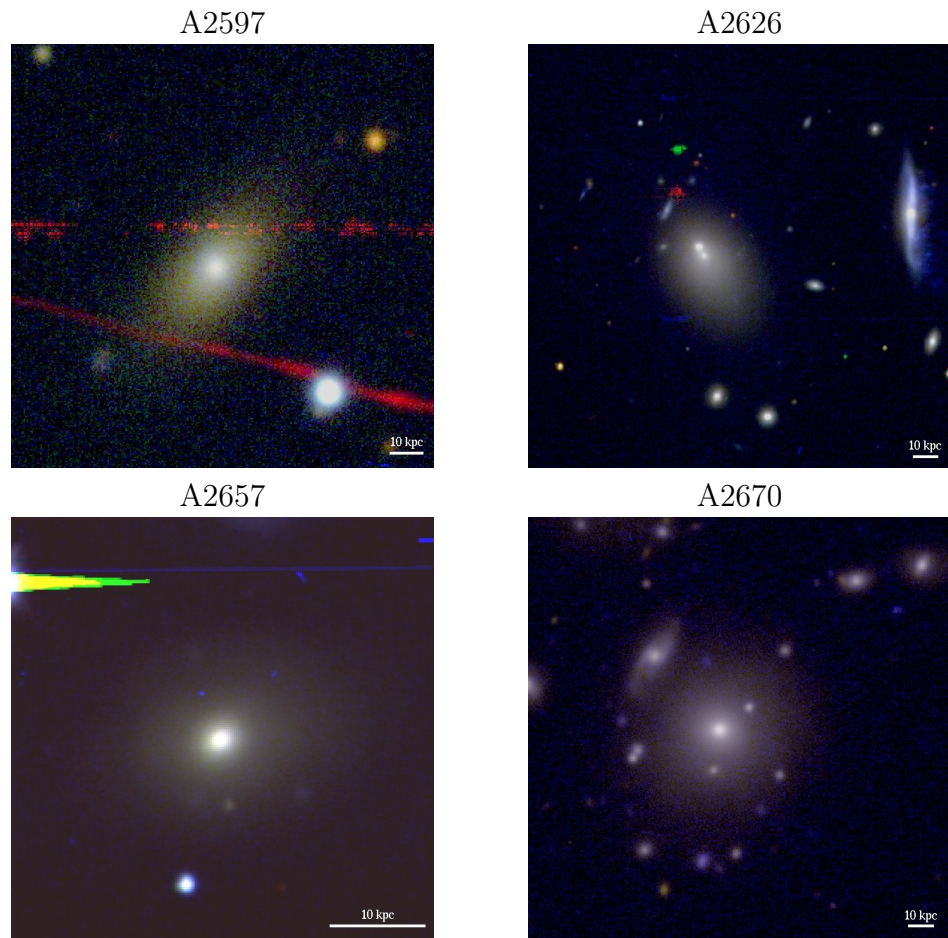


Figure A.7: Optical images of the CDGs in the sample — continued.

APPENDIX B

Pipeline Software

To automate much of the reduction of the *Chandra* X-ray data, pipeline software was written. The following are the instructions for its use.

PIPELINE SOFTWARE FOR ACIS CHIPS

The following IDL procedures may be used to reprocess and analyze nongrating Chandra data. Each should be run from the parent directory of the observation (i.e. from the directory that contains the primary and secondary directories). These instructions assume the pipeline procedure files are in your IDL path and the NEWCOOL executable is in your regular path.

General instructions:

-
- 0) Download the following files from the Chandra Data Archive [you must use Chaser or WebChaser (<http://cda.harvard.edu/chaser>) to download the files if you wish to make a new bad pixel file]:
 *_evt1.fits
 *_evt2.fits
 *_asol1.fits (may be more than one)
 *_aoff1.fits
 *_bpix1.fits
 *_flt1.fits
 *_msk1.fits
 *_bias0.fits (optional: for new bpix file)
 *_pbk0.fits (optional: for new bpix file)
 - 1) Edit `ciao_info.txt`. Enter the path to `ciao.csh` (this should be the same as the path in your `.cshrc` file) and the path to `lhea-init.csh` (for XPSEC and FTOOLS).
 - 2) Copy the following files to the observation directory:
`ciao_info.txt`
`weights.txt`
`newcool` (for use on turvy)

- 4) Change to the observation directory if you're not already there.

To reprocess and make blank-sky background file:

-
- 5) Run ACIS_REPROCESS in IDL for the chip of interest (see diagram below). The default chipid is 7 (the ACIS-S3 chip). If desired, use /newbpix to make a new bad pixel file:

```
IDL> acis_reprocess [, chipid=chipid, /newbpix]
```

To extract spectra in annuli:

-
- 6) Determine the center for the concentric annuli in physical coordinates (ie xc,yc; a good image to look at is images/ccd_img_clean.fits), as well as the ellipticity (1-b/a) and the position angle (degrees ccw from +x-axis to semi-major axis) if you want to use ellipses.
 - 7) Run EXTRACT_ANNULI in IDL:

```
IDL> extract_annuli, xc, yc, mincnts, /mkacisrmf [, chipid=chipid,
          ellip=ellip, pa=pa, cencnts=cencnts]
```

To fit the spectra with a single temperature model:

-
- 8) Run FIT_SPECTRA in IDL:

```
IDL> fit_spectra, /DEPROJECTED [, /FLUX]
```

The FLUX keyword will calculate fluxes for the best-fit model. Values are required for Galactic nH (use the weighted average value from <http://heasarc.gsfc.nasa.gov/cgi-bin/Tools/w3nh/w3nh.pl>), kT (typically kT=3.0 works well), abundance (0.3 works well), redshift (from NED: <http://nedwww.ipac.caltech.edu/>), low and high energy cutoffs (typically low=0.5 and high=7.0, the range for which Chandra is well calibrated), the number of regions to fit (typically the number of regions that you extracted in EXTRACT_ANNULI), and the counts per bin (typically 30).

To plot the results:

-
- 9) Run PLOT_ANNULI in IDL:

```
IDL> plot_annuli, /DEPROJECTED
```

The following 3 steps are only necessary if you want to fit models to the cooling region; otherwise, skip to step 13.

To extract cooling regions:

-
- 10) To make a region whose outer boundary lies exactly on the cooling radius (defined to be the radius at which the cooling time is 7.7 Gyr), run EXTRACT_COOLING in IDL:

```
IDL> extract_cooling [, chipid=chipid, /MKACISRMF]
```

The annuli properties used in EXTRACT_ANNULI are used again here. The radii of the two regions nearest the cooling radius will be adjusted. The number of the cooling region (the region whose outer boundary lies exactly on the cooling radius) will be displayed on the screen and is required for the next step.

To fit a cooling model:

-
- 11) Run FIT_SPECTRA in IDL:
- ```
IDL> fit_spectra, /COOLING [, /FLUX]
```

To find the total X-ray or cooling flux inside the cooling radius:

- 
- 12) Run FIT\_SPECTRA in IDL:
- ```
IDL> fit_spectra, /COOL_FLUXES
```

To get a summary of the cluster properties:

-
- 13) Run CLUSTER_PROPERTIES in IDL:
- ```
IDL> cluster_properties, /DEPROJECTED [, /COOLING, /FLUX]
```

To clean up all unnecessary files:

- 
- 14) Once you've finished the analysis, run CLEAN\_UP.SH to delete unneeded files:
- ```
% clean_up.sh
```

ACIS_REPROCESS:

Purpose: Reprocesses the event files and the background file (calls process_events.pro and acis_bg.pro), starting from the data archive products.

Required files: secondary/flt1 file
secondary/evt1 file
secondary/aoft1 file
primary/evt2 file
primary/asol1 file(s)
ciao_info.txt

Optional files: secondary/bias0 file (for new bad pixel file)
secondary/pbk0 file ("")

Key files created: obs_info_###.txt (information about the data)
reprocessed/evt2_c7_clean.fits (cleaned event file)
reprocessed/evt2_c7_clean_no_ptsrc.fits (no point sources)
background/bg.fits (background file)
primary/new_bpix.fits (optional: new bad pixel file)

EXTRACT_ANNULI:

Purpose: Extracts spectra in circular or elliptical annuli for spectral fitting and makes the appropriate weighted RMFs and ARFs. Will also extract a central spectrum with a different number of counts (cencnts) from the other spectra (mincnts).

Required files: primary/bpix1 file
primary/asol1 file(s)
outputs of ACIS_REPROCESS

Key files created: obs_info_###.txt (updated)
spectra/ccd_asphist.fits
spectra/reg*_sou.pi (spectra)
spectra/reg*_bgd.pi (background spectra)
regions/annuli_mincounts.reg (ds9 region file)
spectra/annuli.txt (summary of region properties)

```
spectra/sb.dat (surface brightness data file)
```

```
-----  
FIT_SPECTRA:  
-----
```

Purpose: Fits the resultant spectra extracted by "extract_annuli.pro" with a single temperature wabs*mekal model in XSPEC. Prompts for initial model parameters. Fits either a projected model (wabs*mekal) or a deprojected model (projct*wabs*mekal). The abundance (Z) is allowed to vary; nH and redshift are fixed.

Required files: output of EXTRACT_ANNULI

Key files created: obs_info_###.txt (updated)
spectra/plot_mekal.ps (plot of fitted spectra)
spectra/source_mekal.spectra (best fit model)
spectra/xspec_mekal.log (fit summary)

PLOT_ANNULI makes: radial_plots_deproj_1.ps (radial plots of kT, ne, P, and S)
radial_plots_deproj_2.ps (radial plots of Z, SB, and t_cool)

APPENDIX C

Co-authored Publications

The following are publications on which I contributed work that is not included in this dissertation. My contributions are as follows:

McNamara et al. (2005) I did the X-ray analysis of MS 0735.6+7421.

Nulsen et al. (2005a) I did some early X-ray analysis.

Levan et al. (2006) I made some of the observations used in the paper.

McNamara et al. (2006) I did the X-ray analysis of A1835.